

## Cell-internalized MRI contrast agents

**Citation for published version (APA):**

Kok, M. B. (2010). *Cell-internalized MRI contrast agents*. [Phd Thesis 1 (Research TU/e / Graduation TU/e), Biomedical Engineering]. Technische Universiteit Eindhoven. <https://doi.org/10.6100/IR672781>

**DOI:**

[10.6100/IR672781](https://doi.org/10.6100/IR672781)

**Document status and date:**

Published: 01/01/2010

**Document Version:**

Publisher's PDF, also known as Version of Record (includes final page, issue and volume numbers)

**Please check the document version of this publication:**

- A submitted manuscript is the version of the article upon submission and before peer-review. There can be important differences between the submitted version and the official published version of record. People interested in the research are advised to contact the author for the final version of the publication, or visit the DOI to the publisher's website.
- The final author version and the galley proof are versions of the publication after peer review.
- The final published version features the final layout of the paper including the volume, issue and page numbers.

[Link to publication](#)

**General rights**

Copyright and moral rights for the publications made accessible in the public portal are retained by the authors and/or other copyright owners and it is a condition of accessing publications that users recognise and abide by the legal requirements associated with these rights.

- Users may download and print one copy of any publication from the public portal for the purpose of private study or research.
- You may not further distribute the material or use it for any profit-making activity or commercial gain
- You may freely distribute the URL identifying the publication in the public portal.

If the publication is distributed under the terms of Article 25fa of the Dutch Copyright Act, indicated by the "Taverne" license above, please follow below link for the End User Agreement:

[www.tue.nl/taverne](http://www.tue.nl/taverne)

**Take down policy**

If you believe that this document breaches copyright please contact us at:

[openaccess@tue.nl](mailto:openaccess@tue.nl)

providing details and we will investigate your claim.

# **Cell-internalized MRI contrast agents**

This study was funded in part by the BSIK program entitled Molecular Imaging of Ischemic Heart Disease (project number BSIK03033) and by the EC-FP6-project DiMI, LSHB-CT-2005-512146. This study was performed in the framework of the European Cooperation in the field of Scientific and Technical Research (COST) D38 Action Metal-Based Systems for Molecular Imaging Applications.

A catalogue record is available from the Library Eindhoven University of Technology

ISBN: 978-90-386-2216-3

Printed by: Ipskamp, Enschede, The Netherlands

Cover Design: Jeanne Collignon

# Cell-internalized MRI contrast agents

Proefschrift

ter verkrijging van de graad van doctor aan de Technische Universiteit Eindhoven, op gezag van de rector magnificus, prof.dr.ir. C.J. van Duijn, voor een commissie aangewezen door het College voor Promoties in het openbaar te verdedigen op maandag 26 april 2010 om 16.00 uur

door

Maarten Boudewijn Kok

geboren te Enschede

Dit proefschrift is goedgekeurd door de promotor:

prof.dr. K. Nicolay

Copromotor:

dr.ir. G.J. Strijkers



## Contents

<b>Chapter 1:</b>	Introduction	1
<b>Chapter 2</b>	The cellular compartmentalization of internalized paramagnetic liposomes strongly influences both $T_1$ and $T_2$ relaxivity	17
<b>Chapter 3:</b>	A three-compartment $T_1$ -relaxation model for intracellular paramagnetic contrast agents	41
<b>Chapter 4:</b>	Dynamic changes in $^1\text{H}$ -MR relaxometric properties of cell-internalized paramagnetic liposomes, as studied over a 5-day period	69
<b>Chapter 5</b>	Influence of cell-internalization on relaxometric, optical and compositional properties of targeted paramagnetic quantum dot micelles	87
<b>Chapter 6:</b>	Quantitative $^1\text{H}$ MRI, $^{19}\text{F}$ MRI, and $^{19}\text{F}$ MRS of cell-internalized perfluorocarbon paramagnetic nanoparticles	111
<b>Chapter 7:</b>	A multimodal liposome for combined SPECT, MR and fluorescence imaging	131
<b>Chapter 8:</b>	General discussion	147
<b>Summary</b>		157
<b>Dankwoord</b>		163
<b>List of publications</b>		167
<b>Curriculum Vitae</b>		169

# Chapter **1**

## **Introduction**



# 1 Introduction

The use of contrast agents is essential for molecular MRI, a new and rapidly developing field that focuses on *in vivo* imaging of biological markers and processes. This chapter starts with an introduction on molecular imaging and is followed by an overview of research conducted in the four major application areas of molecular imaging: cancer, atherosclerosis, myocardial infarction and neurological disorders. Subsequently the use of contrast agents will be addressed. The rationale, aim and approach of the thesis conclude this chapter.

## 1.1 Molecular Imaging

Conventional imaging techniques such as positron emission tomography (PET), single photon-emission CT (SPECT), computed tomography (CT), ultrasound (US) and magnetic resonance imaging (MRI) are routinely used to differentiate between healthy and diseased tissue on the anatomical or physiological level. However, detection of diseases in earlier stages of development is very beneficial for treatment outcome. During the development of a disease several stages can be identified. These stages concur with the differential up- or down-regulation of specific proteins or other molecules that are either excreted or exposed by cells. The field that focuses on the imaging and measuring of these biologic processes at the cellular and molecular level is called molecular imaging [1]. New approaches for imaging molecules are being developed to better understand the biology of disease processes and to identify options for disease diagnostics and therapy. The field of molecular imaging mainly focuses on diseases that can be targeted via the blood stream, using an intravenous injection of contrast agent. Cancer [2], atherosclerosis [3], myocardial infarction [4], and neurological disorders [5, 6] are key areas for molecular imaging research which will be elaborated on in the next four paragraphs.

### Cancer

Cancer is the main cause of death in the western world. Molecular imaging of cancer will allow clinicians not only to see if and where a tumor is located in the body, but also to visualize biological processes and the expression and activity of specific molecules, that are altered during tumor formation. A commonly used approach is the administration of the PET agent [<sup>18</sup>F]fluorodeoxyglucose (FDG). FDG is a glucose analog that is rapidly taken up by cells with a high rate of glucose metabolism, a key feature of malignant cells [7]. FDG-PET has also been used for predicting tumor response to treatment and patient survival [8]. During tumor growth angiogenesis is required to provide oxygen and nutrition to

the growing tumor. The  $\alpha_v\beta_3$ -integrin, a key marker for angiogenic blood vessels, has served as an excellent target for molecular imaging of tumor vascular endothelium [9, 10]. Extracellular matrix remodeling, required for angiogenesis, has been visualized by imaging MMP activity [11]. Many tumors also develop a necrotic core. Strategies to image cell death include the use of ligands, such as Annexin V, that target apoptotic cells [12-14]. Besides imaging of molecular processes induced by tumor formation, molecular markers have been imaged that are uniquely expressed by specific tumor types [15-20]. For example, the human epidermal growth factor receptor 2 (HER-2) has been targeted using a monoclonal antibody. This receptor is highly upregulated in several types of cancer, including breast, lung and bladder carcinomas. Positive  $T_1$  contrast in MR images was generated by the specific binding of avidin-gadolinium complexes to tumor cells prelabeled with a biotinylated anti-HER-2/neu antibody [20].

### **Atherosclerosis**

Atherosclerosis lies at the basis of myocardial infarction and stroke and is a major cause of death and illness in developed countries. Atherosclerosis is characterized by the accumulation of lipids and fibrous elements in the walls of large arteries. Several stages can be identified and markers expressed during these stages can serve as targets for molecular imaging [21]. Initial plaque formation was detected by visualizing adhesion molecules such as the cell-adhesion molecules VCAM-1 and ICAM-1 as well as P- and E-selectin [22-24], which play an essential role in the recruitment of inflammatory cells during the initial stages of atherosclerosis. Furthermore, several groups have imaged the presence of inflammatory cells such as macrophages and T-cells using MRI and PET [25-29]. Besides direct imaging of macrophages, several molecules excreted by these cells, including the matrix metallo proteinases MMP-2 and MMP-9 also are excellent targets for molecular imaging and were visualized using SPECT/CT and MRI [30, 31]. Rupture-prone plaques can be distinguished based on the presence of a necrotic core by imaging of the apoptotic cells [32, 33]. Fibrin can be targeted to reveal the presence of a thrombus that is formed after rupturing of a vulnerable plaque [34-37]. The formation of angiogenic vessels in advanced atherosclerotic plaques, which could destabilize the plaques, has been imaged by targeting the  $\alpha_v\beta_3$ -integrin [38, 39].

### **Myocardial Infarction**

Closely related to atherosclerosis is myocardial infarction. Myocardial infarction is caused by an obstruction within the coronary arteries, most commonly due to acute thrombus formation following plaque rupture or entrapment of emboli. Generally, four phases can be distinguished after occlusion of the coronary

artery. Phase 1 is characterized by death of cardiomyocytes through apoptosis or necrosis. After the initial cell death secondary necrosis occurs initiated by the inability of cells to phagocytose the apoptotic cells. Phase 1 and 2 have been imaged using markers such as VCAM-1 [40] and markers for apoptosis [40]. This type of cardiomyocyte death evokes an early inflammatory response (phase 2). During this phase several inflammatory cells, such as lymphocytes, plasma cells and macrophages, infiltrate the infarction. Extensive remodeling of the extracellular matrix starts during phase 2, which was imaged by targeting matrix metallo proteinases (MMPs) [41, 42]. Phase 3 is the formation of highly vascularized granulation tissue which increases the tensile strength of the infarct and prevents rupture. The newly formed vessels in phase 3 were detected by Meoli *et al.* using SPECT [43]. During this phase several extracellular matrix proteins are deposited, such as fibronectin and collagen. Phase 4 is characterized by the disappearance of all cells except for myofibroblasts resulting in scar tissue formation. The formation of collagen during phase 3 and 4 was assessed using a collagen targeted MR contrast agent by Caravan *et al.* [44, 45].

### **Neurological disorders**

Several imaging modalities have been used for molecular imaging of diseases of the central nervous system such as stroke, Alzheimer's disease, Parkinson's disease and multiple sclerosis. Main features of most of these diseases include the initiation of an inflammatory response inducing the upregulation of adhesion molecules, disruption of the blood brain barrier and the infiltration of monocytes [5, 6]. Vascular inflammation after stroke was visualized by MRI using VCAM-1 targeted superparamagnetic iron oxide particles [46]. A key inflammatory enzyme, myeloperoxidase (MPO) that is secreted by activated neutrophils and macrophages, was imaged using an MR probe that, when activated, could bind to proteins or form a polymer, causing a longer retention time and an increase in  $T_1$ -weighted MRI signal intensity [47]. Neuroinflammation has also been detected using a radiolabeled probe that binds to the peripheral benzodiazepine receptor, a marker that is highly expressed by microglial cells and monocytes infiltrating the brain parenchyma [48]. CD40, a marker that is upregulated during neuroinflammation was imaged using a near infrared probe conjugated to a monoclonal antibody [49]. Besides imaging neuro-inflammation, also disease specific approaches are actively explored. Molecular imaging of Alzheimer's disease has mainly focused on specialized probes targeted to the amyloid  $\beta$  plaques [50, 51].

## 1.2 Contrast agents

The development of suitable contrast agents is of critical importance to molecular imaging. The applications described in the previous paragraphs employed targeted contrast agents to detect specific processes during disease development. A targeted contrast agent generally consists of two components: (i) a ligand with high affinity for a biological marker such as peptides, proteins, small molecules, carbohydrates, antibodies and antibody fragments; and (ii) a component that can be detected by the imaging modality-of-choice as for instance radio-isotopes (SPECT/PET), fluorochromes (NIRF), magnetic moieties (MRI) or sonic enhancers (US) [4]. The choice of contrast agent depends not only on the imaging modality used, but also on the location and abundance of the molecular target. For detection, imaging modalities require different minimal contrast agent concentrations to be present at the site of interest. NIRF and the nuclear techniques only require concentrations of contrast agent in the nM – pM range, whereas MRI requires that the magnetically active component of a contrast agent is present at effective concentrations in the sub-mM range [52].

The nature of the targets used for molecular imaging, greatly dictates the type of contrast agent that can be used. Extracellular matrix proteins, such as elastin, fibrin and collagen are targets that are often abundantly present, while other targets are present only very sparsely. The highly abundant molecular markers can be targeted using low molecular weight contrast agents with a size of only a few nm (see Figure 1). Targeting of these markers generally leads to high accumulation of contrast agent, enabling detection by imaging modalities with a relatively low intrinsic sensitivity. In contrast, sparse molecular markers, which can have a concentration as low as  $10^{-9}$  to  $10^{-13}$  mol/g [53], require alternative targeting strategies to reach levels of contrast agent that enable detection by techniques with a relatively low sensitivity to contrast agents, such as MRI. For MRI, several amplification strategies have been reported in literature, which include the use of high-payload contrast agents such as micelles, liposomes and micro-emulsions that deliver several hundreds to thousands contrast agent moieties per targeting event. Another amplification strategy is targeting of a receptor that recycles itself back to the cellular membrane after docking of a contrast agent and subsequent cell internalization. Other strategies that lead to an increase in contrast agent at the site of interest are entrapment in the cell after internalization of contrast agents by cells [54], target-specific oligomerization of small ligands [55] or the use of dual-ligand contrast agents that are targeted to two markers simultaneously [56].

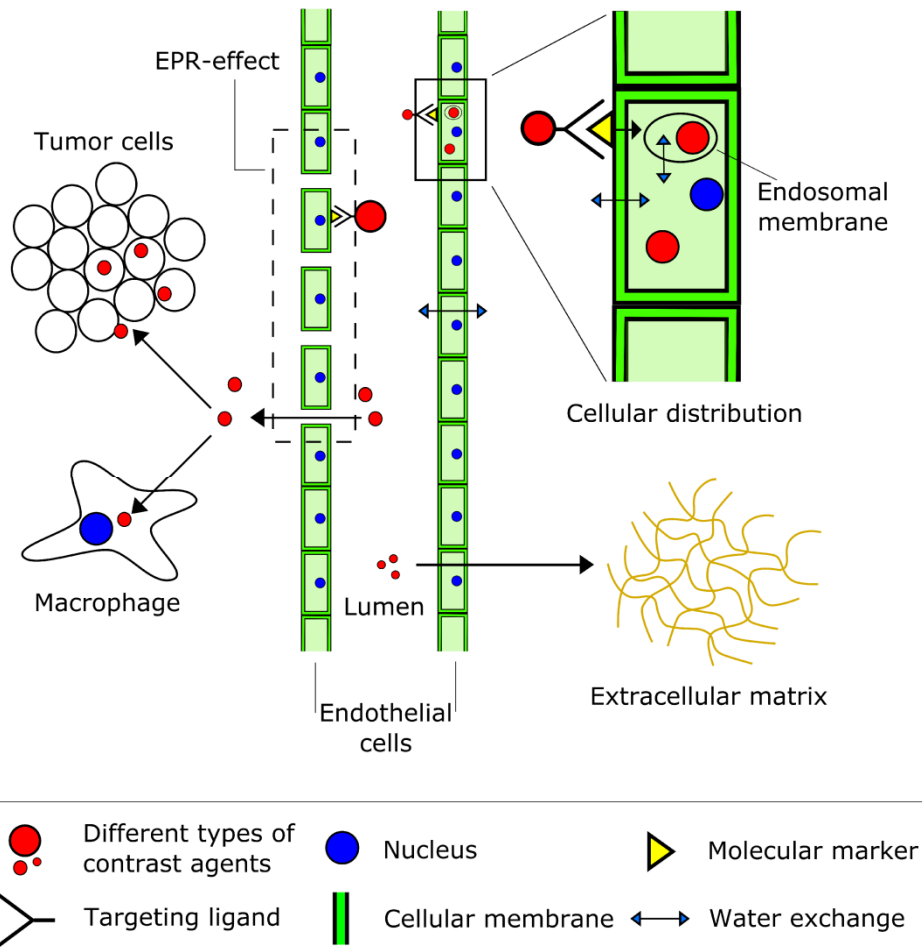


**Figure 1, Schematic drawing of some of the factors that influence the *in vivo* behavior of contrast agents.** Immediately after intravenous injection, the contrast agents will disperse in the vascular compartment (indicated by "Lumen" in the central part of the figure). Access to the extravascular compartment depends on a range of factors, including the size of the contrast agent. In many tissues, low-molecular weight agents are able to permeate the endothelial cell layer lining the blood vessel (large bottom-right arrow) and thus can reach targets that are located in the extravascular, extracellular compartment (including extracellular matrix components). In contrast, high-molecular weight contrast materials are generally only able to reach targets that are directly accessible from the bloodstream, *i.e.*, targets that are expressed on the endothelial cell layer. Binding of the molecular imaging probe to its target may trigger internalization of the complex. This situation is depicted in the upper right part of the scheme and is particularly relevant for MRI. Depending on the nature of the contrast agent and the contrast mechanism that is exploited, internalization may alter the efficacy of the MRI contrast agent in a complicated fashion. This is one of the major topics of this thesis. In certain disease situations, the endothelial cell lining is impaired (top left), enabling also larger contrast agents to extravasate from the blood stream. This situation is often encountered in tumors and in states of tissue inflammation and frequently not only leads to enhanced extravascular delivery of high-molecular weight contrast materials but also to their prolonged retention (the enhanced permeability and retention, or EPR, effect). Clearly in this case, large contrast agents are suited for molecular imaging of extravascular targets. Many diseases are associated with the presence of inflammatory cells, such as macrophages, in the extravascular space (bottom left). This may negatively affect the specificity of molecular imaging read-outs, as these cells often have phagocytotic activity, which especially promotes the internalization of foreign (nano)particles.

Another important parameter is the location of the molecular marker, as this may greatly influence the chance of successful targeting (Figure 1). Many different molecular markers are available for monitoring diseases such as cancer, atherosclerosis, myocardial infarction, stroke and Alzheimer's disease. Several of these markers, such as  $\alpha_v\beta_3$ , VCAM-1, ICAM-1, P-selectin, E-selectin, are present on the endothelial cells lining the blood vessels. Such targets are relatively easy to reach via the bloodstream with contrast agents varying in size from a few nm to a few  $\mu\text{m}$ . Later stages of a disease often involve the occurrence of apoptosis or necrosis or the presence of macrophages, processes that are mainly located beyond the endothelial layer. Imaging of apoptosis, necrosis or macrophages, requires the contrast agent to diffuse out of the blood stream to reach its target. In general, these markers can only be reached by using smaller contrast agents, since larger particles are not able to diffuse into the tissue. However, the endothelial cell lining is not properly aligned during inflammation or in the neovasculature formed in tumor tissue. These processes cause the formation of pores in the vessel wall, allowing macromolecular structures ( $<500\text{ nm}$ ) to enter the interstitial space. This phenomenon is called the enhanced permeability and retention effect (EPR-effect) (Figure 1) [57].

### **1.3 Problem definition**

To be able to measure molecular processes, using contrast agents, several criteria have to be fulfilled. The imaging technique will need a high sensitivity, preferably in the low nanomolar to picomolar range. Besides a high sensitivity the modality of choice also needs a high spatial resolution on preferably the cellular scale. Furthermore not only a high sensitivity and resolution are important, but also the ability to quantify the signal, *i.e.* being able to determine the local concentration of the targeted contrast agent is highly desired.

This thesis has focused on the use of contrast agents for molecular imaging using  $^1\text{H}$  MRI.  $^1\text{H}$  MRI has the advantage of providing high spatial and temporal resolution with excellent soft tissue contrast. Furthermore, MRI yields information on the structure, the function and metabolism of tissues *in vivo*. A major limitation of MRI for molecular imaging, however, is its intrinsically low sensitivity to detect contrast agents. A distinct feature of MRI is that most  $^1\text{H}$  MRI contrast agents are not signal emitting moieties themselves. Not the contrast agent itself is measured, but its influence on the magnetic properties of surrounding water protons. Therefore other parameters, such as contrast agent confinement, water diffusion and the local water concentration are of influence on the efficacy of the contrast agent.

Figure 2 illustrates that the effects of cellular confinement should be carefully considered, when interpreting molecular MR imaging. This figure shows a cross-section of an atherosclerotic plaque in the carotid artery of a mouse. The atherosclerotic plaque was targeted using a VCAM-1 recognizing antibody conjugated to a gadolinium-containing, paramagnetic liposome. In yellow the endothelial lining of the vessels can be appreciated. The red color represents a fluorophore that was incorporated in the lipid bilayer of the abovementioned liposome. The microscopy data show that the contrast agent was internalized by the endothelial cells and that targeting was successful. Disappointingly, only relatively weak contrast enhancement was detected using  $T_1$ -weighted MRI (not shown). Figure 2B shows a magnification of the square in Figure 2A which has roughly the dimension of a MRI pixel ( $100 \times 100 \mu\text{m}^2$ ).

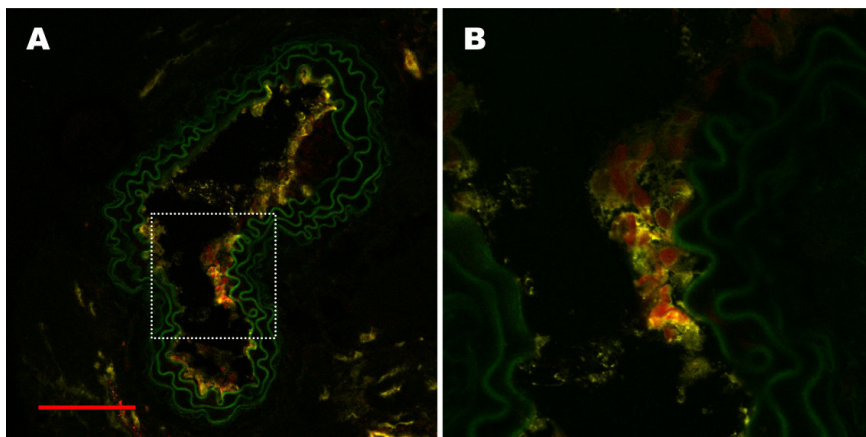


**Figure 2, CLSM image of a cross-section of an atherosclerotic plaque present in the carotid artery of an apo-E  $-/-$  mouse. Images were made 24 hr post injection of a VCAM-1 targeted paramagnetic liposome. Yellow represents endothelial cells, red is contrast agent, green is elastin autofluorescence. bar = 100  $\mu\text{m}$ . A) cross-section overview, B) enlargement of square in A Courtesy of G.S. van Bochove (Eindhoven University of Technology), unpublished observations.**

Several *in vitro* and *in vivo* experiments have confirmed that the abovementioned factors indeed play an important role in the detection and quantification potential of  $T_1$ -based contrast agents used for molecular imaging. Several groups have reported a reduction in  $r_1$  relaxivity, *i.e.* the efficiency of the contrast agent to lower the  $T_1$  relaxation rate (in units of  $\text{mM}^{-1}\text{s}^{-1}$ ), after internalization of the contrast agent by cells. This phenomenon is called quenching of the relaxivity. A reduction in  $T_1$ -shortening efficacy of Gd-HPDO3A has been reported by Terreno *et al.* [58]. The authors describe that internalization of this low molecular weight contrast agent in endosomes by pinocytosis severely lowered the longitudinal relaxivity. For contrast agents present in the cytoplasm quenching only occurred at very high concentrations.

Brekke *et al.* [59, 60] labeled neural stem cells for cell tracking purposes, with another gadolinium-based contrast agent, gadolinium rhodamine dextran (GRID). Both *in vivo* and *in vitro* analysis showed that the GRID-labeled cells induced signal attenuation on both  $T_2$ - and  $T_2^*$ -weighted images. However, only a modest signal gain was obtained on  $T_1$ -weighted images. Kobayashi *et al.* [61] have also observed reduced longitudinal relaxivity after internalization of avidin-dendrimer-(1B4M-Gd)<sub>254</sub> into tumor cells. Lewin *et al.* [62] have investigated the internalization of Gd-EOB-DTPA in rat cultured hepatocytes and two hepatoma cell lines, observing reduced longitudinal relaxivity of the internalized contrast agent. Quenching of the longitudinal relaxivity using a targeted contrast agent has been reported by Geniatti Crich *et al.* [63]. She describes the targeting of the amino acid transporter system of hepatoma cells using the low molecular weight contrast agent Gd-DOTAMA-C<sub>6</sub>-Gln. Although several groups have reported the occurrence of quenching of the  $r_1$  relaxivity, relatively little is known about the cause of this phenomenon [64]. Terreno *et al.* [58] attributed the reduced longitudinal relaxivity to limited water exchange consequent to contrast agent entrapment in subcellular compartments (see Figure 1: blue arrows).

If the causes and consequences of the quenching of the relaxivity are identified, strategies can be developed to prevent this phenomenon from occurring. Furthermore, quenching of the longitudinal relaxivity hampers the translation from signal intensity to contrast agent concentration, since the relaxivity of the contrast agent is altered upon internalization. Quantification of the concentration of contrast agent is not only very beneficial for molecular MRI, but also for MRI monitored drug delivery and MR mediated cell tracking.

## 1.4 Aim of this thesis

**The aim of this thesis was to study the effects of internalization of lipid based MR contrast agents by cells, focusing on cellular location, relaxometry and quantification.**

## 1.5 Approach

To assess the influence of internalization of lipid based MR contrast agents on cellular location, relaxometry and quantification, an *in vitro* strategy was developed (Figure 3). An *in vitro* model setup was needed, since the *in vivo* situation does not allow studying cellular location, contrast agent concentration and relaxometric parameters simultaneously over time. Furthermore, blood flow, pharmacokinetics and the presence of a variety of cells all interacting



differently with the contrast agents used, further complicate the interpretation of data. In the *in vitro* model developed in this thesis, human umbilical vein derived endothelial cells (HUVECs) were incubated with either targeted or non-targeted MR contrast agents for different periods of time. To obtain information on efficacy of the contrast agents, the *in vitro* approach combined a variety of techniques including MRI, MRS, fluorescent activated cell sorting (FACS), inductively coupled plasma atomic emission spectroscopy (ICP-AES), Cryo-TEM and confocal laser scanning microscopy (CLSM).

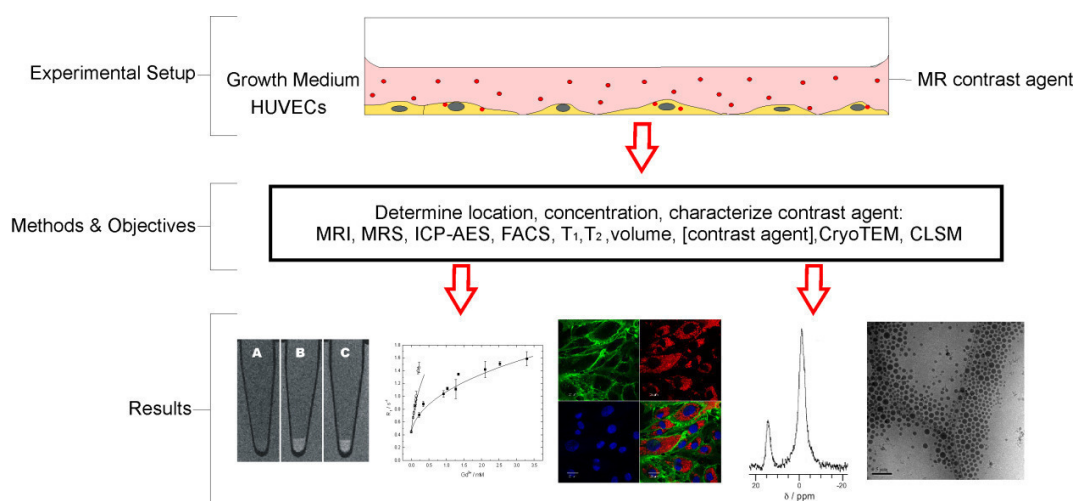


**Figure 3, Experimental setup employed in this thesis. HUVECs were grown in culture flasks and on gelatin coated coverslips. After incubation with the MR contrast agent, HUVECs were harvested. The pellets formed were analyzed by a variety of techniques, while HUVECs grown on coverslips were subjected to CLSM to locate the contrast agent. Quantification of the uptake was assessed by ICP-AES and MRS.**

## HUVECs

Human umbilical vein derived endothelial cells (HUVECs) have been used as a model system for angiogenesis in various studies [65-68]. The cells were exposed to growth factors that play a role during angiogenesis, such as vascular endothelial growth factor (VEGF), basic fibroblastic growth factor (bFGF), hypoxia-induced growth factor-1 $\alpha$  (HIF-1 $\alpha$ ) and epidermal growth factor (EGF), to express high levels of the  $\alpha_v\beta_3$  integrin. The  $\alpha_v\beta_3$  integrin is able to bind a variety of extracellular matrix components containing an RGD (Arg-Gly-Asp)-sequence such as present in vitronectin, fibronectin and fibrinogen. In peptide form, the RGD sequence is therefore an excellent ligand for targeting of this integrin. After a ligand binds the  $\alpha_v\beta_3$  integrin, the ligand-receptor complex is internalized via either caveolae or clathrin mediated uptake mechanisms. Following cellular internalization, the  $\alpha_v\beta_3$  integrin proceeds to early endosomes. There, the integrin is either further trafficked to the perinuclear recycle center,

followed by its recycling to the cellular membrane or trafficked back to the cellular membrane immediately [69].

### **Lipid based nanoparticles**

In this thesis a variety of lipid based paramagnetic contrast agents was used to study the effect of internalization on relaxometric parameters and quantification. Lipid based nanoparticles have been used in the past decade for various applications such as drug delivery [70] and contrast enhanced MRI [71]. They are composed of amphiphilic molecules, mainly phospholipids that are known for their biocompatibility. Most lipid based particles have the ability to carry drugs. Hydrophobic drugs can be incorporated in the lipid layer, or in the core of the nanoparticles. Hydrophilic drugs can be bound to the surface of the nanoparticle or can be incorporated in the lumen of a liposome. Figure 4 shows schematic examples of different types of lipid based nanoparticles. A liposome (shown in Figure 4A) can be described as a spherical lipid bilayer enclosing an aqueous compartment. Liposomes can be produced by either extrusion or sonification and are typically sized to have a narrow range of diameters (typically between 60 nm to 1  $\mu\text{m}$ ). In Figure 4B a schematic representation of an emulsion is drawn. An emulsion contains a hydrophobic core which is covered by a monolayer of phospholipids or other amphiphiles that make it watersoluble. The hydrophobic core may consist of natural oils, such as soybean and mineral oil, medium or long chain triglycerides or iodine- or fluor-containing compounds [70]. Emulsions are typically available in the same size range as liposomes. Smaller lipid based nanoparticles are depicted in Figure 4C-E. Micelles (Figure 4C) have a size of 10-50 nm, depending on the lipids used and the size of the inorganic core, if present. Micelles are formed by the hydrophobic associative interaction of the tails of amphiphiles. Closely related to the micelles are micellar nanoparticles that contain an inorganic core. Hydrophobic coated nanoparticles like quantum dots (Figure 4D) or iron oxide (Figure 4E) can be coated with a micellar shell of PEG-containing lipids to make them water soluble [71]. The lipid bi- or monolayer of a nanoparticle normally contains amphiphiles as a main component. Generally phospholipids are used with two carbon tails containing typically 16 or 18 carbon atoms per chain. Cholesterol can be added to lower ion- and water-exchange rates and to stabilize the lipid layer. A nanoparticle can further be equipped with for instance fluorophores, for fluorescence imaging, or MR contrast agents such as Gd-DTPA or Gd-DOTA conjugated to a phospholipid, for MRI detection. To influence pharmacokinetic properties, PEG-conjugated lipids can be introduced, resulting in a prolonged blood circulation half-life. Furthermore the nanoparticle can be modified with a targeting ligand that can be introduced by modification of the distal end of the

PEG-lipids, by for instance native chemical ligation [72], sulfhydryl coupling [71] or avidin-biotin complexation [73].

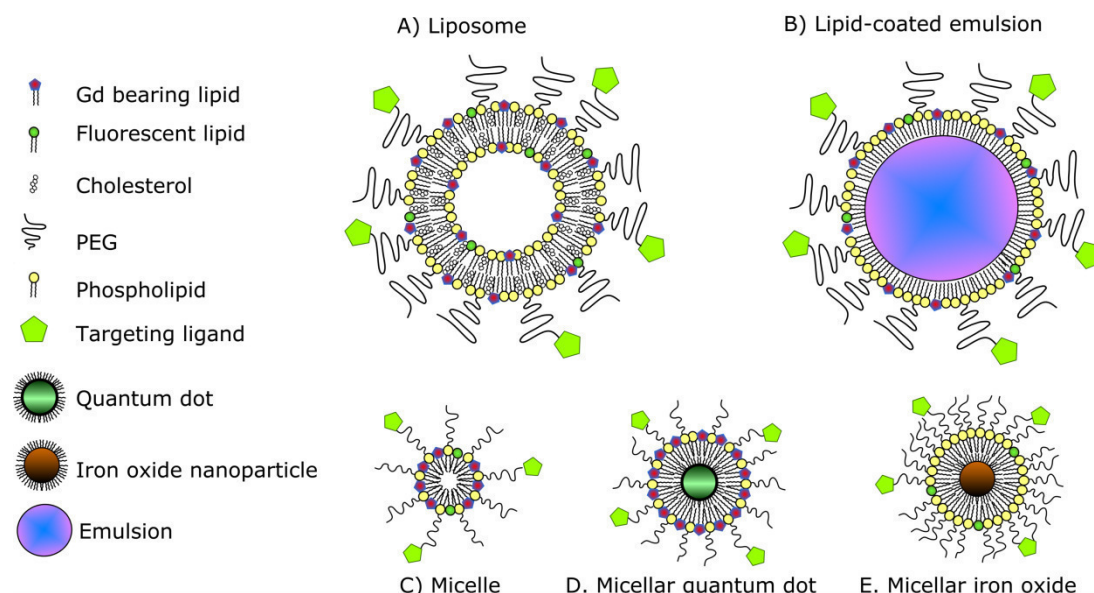


**Figure 4, Lipid based paramagnetic nanoparticles. A) liposome, B) emulsion, C) micelle, D) micellar quantum dot, E) iron oxide. The column on the left shows the components of the nanoparticles.**

### Experimental Setup

Throughout this thesis several experiments have been performed in which HUVECs were incubated with different lipid based contrast agents that were conjugated with a RGD-peptide. Incubations with non-conjugated contrast agents served as a model system for nonspecific uptake. HUVECs were typically incubated with MR contrast agents for a period of time varying from 0 – 24 hr. In some cases, prolonged incubation times were explored. After incubation three types of samples were prepared. Samples were harvested and pelleted for MRI, residual cells were used for FACS analysis, and HUVECs grown on gelatin-coated coverslips were incubated and subsequently fixed for confocal laser scanning microscopy. The cell pellets were allowed to settle for at least 4 days and subsequently  $T_1$  and  $T_2$  maps and volume of the pellets were measured using MRI. After MRI analysis, the samples were destructed and inductively coupled plasma atomic emission spectroscopy was used to determine the concentration of the contrast agent. Fluorescent activated cell sorting was used to determine the mean fluorescent intensity per cell, which is a measure for contrast agent uptake. HUVECs grown on gelatin-coated coverslips were stained for several molecular markers including  $\alpha_v\beta_3$  and CD31 to determine the cellular location by means of confocal laser scanning microscopy. By combining knowledge on

location (CLSM), concentration of the contrast agent (ICP-AES, MRS) and  $T_1$  and  $T_2$ , insights can be obtained in the contrast agent efficacy in relation to its cellular location and concentration.

## **1.6 Outline of this thesis**

This thesis describes the effects of cellular internalization of lipid based MR contrast agents on their intracellular distribution and their relaxometric properties. Chapter 2 describes the *in vitro* setup, in which HUVECs serve as a model system. Using this model, the effect of internalization was studied using RGD-conjugated liposomes. Results were compared to their non-targeted counterparts. Chapter 3 describes a mathematical model which was designed to describe the effects of internalization on the relaxometric properties that were reported in Chapter 2. Chapter 4 deals with dynamic changes in relaxometric properties of cell-internalized paramagnetic liposomes, as studied over a period of 5 days. In Chapter 5, paramagnetic quantum dots were studied in a similar fashion as in Chapter 2. Paramagnetic quantum dots are approximately five times smaller than the liposomes used in Chapter 2. This difference in size may influence cellular uptake routes and thus lead to other, possibly more favorable relaxometric properties. Since translation of the changes in  $^1\text{H}$  MR signal intensity to absolute contrast agent concentration is very challenging, two multimodal approaches were developed. In Chapter 6, a fluorine based paramagnetic emulsion served as a platform for detection by parallel  $^1\text{H}$  and  $^{19}\text{F}$  MRI, and subsequent quantification using  $^{19}\text{F}$  MRI and MRS. In Chapter 7 the excellent quantification properties of SPECT were combined with the outstanding spatial resolution of  $^1\text{H}$  MRI, by equipping a liposome with both gadolinium containing lipids and a SPECT label. Finally, Chapter 8 gives a general discussion and main conclusions of the work presented in this thesis.

## Literature

1. Weissleder, R., U. Mahmood, *Radiology*, 2001. **219**(2): p. 316-333.
2. Weissleder, R., *Science*, 2006. **312**(5777): p. 1168-1171.
3. Sanz, J., Z.A. Fayad, *Nature*, 2008. **451**(7181): p. 953-957.
4. Jaffer, F.A., D.E. Sosnovik, M. Nahrendorf, *et al.*, *J Mol Cell Cardiol*, 2006. **41**(6): p. 921-933.
5. Wunder, A., J. Klohs, U. Dirnagl, *Neuroscience*, 2009. **158**(3): p. 1161-1173.
6. Stoll, G., M. Bendszus, *Neuroscience*, 2009. **158**(3): p. 1151-1160.
7. Quon, A., S.S. Gambhir, *J Clin Oncol*, 2005. **23**(8): p. 1664-1673.
8. Wieder, H.A., B.L. Brucher, F. Zimmermann, *et al.*, *J Clin Oncol*, 2004. **22**(5): p. 900-908.
9. Mulder, W.J., K. Castermans, J.R. van Beijnum, *et al.*, *Angiogenesis*, 2009. **12**(1): p. 17-24.
10. Cai, W., X. Zhang, Y. Wu, *et al.*, *J Nucl Med*, 2006. **47**(7): p. 1172-1180.
11. Bremer, C., S. Bredow, U. Mahmood, *et al.*, *Radiology*, 2001. **221**(2): p. 523-529.
12. Blankenberg, F.G., J.L. Vanderheyden, H.W. Strauss, *et al.*, *Nat Protoc*, 2006. **1**(1): p. 108-110.
13. Schellenberger, E.A., D. Sosnovik, R. Weissleder, *et al.*, *Bioconjug Chem*, 2004. **15**(5): p. 1062-1067.
14. van Tilborg, G.A., W.J. Mulder, N. Deckers, *et al.*, *Bioconjug Chem*, 2006. **17**(3): p. 741-749.
15. Lee, J.H., Y.M. Huh, Y.W. Jun, *et al.*, *Nat Med*, 2007. **13**(1): p. 95-99.
16. Wang, C., J. Chen, T. Talavage, *et al.*, *Angew Chem Int Ed Engl*, 2009. **48**(15): p. 2759-2763.
17. Medarova, Z., L. Rashkovetsky, P. Pantazopoulos, *et al.*, *Cancer Res*, 2009. **69**(3): p. 1182-1189.
18. Thomas, T.P., A.K. Patri, A. Myc, *et al.*, *Biomacromolecules*, 2004. **5**(6): p. 2269-2274.
19. Veisoh, O., C. Sun, C. Fang, *et al.*, *Cancer Res*, 2009. **69**(15): p. 6200-6207.
20. Artemov, D., N. Mori, R. Ravi, *et al.*, *Cancer Res*, 2003. **63**(11): p. 2723-2727.
21. Libby, P., P.M. Ridker, A. Maseri, *Circulation*, 2002. **105**(9): p. 1135-1143.
22. Nahrendorf, M., F.A. Jaffer, K.A. Kelly, *et al.*, *Circulation*, 2006. **114**(14): p. 1504-1511.
23. McAteer, M.A., A.M. Akhtar, C. von Zur Muhlen, *et al.*, *Atherosclerosis*, 2009.
24. Kelly, K.A., J.R. Allport, A. Tsoukas, *et al.*, *Circ Res*, 2005. **96**(3): p. 327-336.
25. Trivedi, R.A., C. Mallawarachi, U.K.-I. JM, *et al.*, *Arterioscler Thromb Vasc Biol*, 2006.
26. Amirbekian, V., M.J. Lipinski, K.C. Briley-Saebo, *et al.*, *Proc Natl Acad Sci U S A*, 2007. **104**(3): p. 961-966.
27. Nahrendorf, M., H. Zhang, S. Hembrador, *et al.*, *Circulation*, 2008. **117**(3): p. 379-387.
28. Izquierdo-Garcia, D., J.R. Davies, M.J. Graves, *et al.*, *Stroke*, 2009. **40**(1): p. 86-93.
29. Tawakol, A., R.Q. Migrino, G.G. Bashian, *et al.*, *J Am Coll Cardiol*, 2006. **48**(9): p. 1818-1824.
30. Haider, N., D. Hartung, S. Fujimoto, *et al.*, *J Nucl Cardiol*, 2009. **16**(5): p. 753-762.
31. Lancelot, E., V. Amirbekian, I. Brigger, *et al.*, *Arterioscler Thromb Vasc Biol*, 2008. **28**(3): p. 425-432.
32. Laufer, E.M., H.M. Winkens, M.F. Corsten, *et al.*, *Q J Nucl Med Mol Imaging*, 2009. **53**(1): p. 26-34.
33. Kolodgie, F.D., J. Narula, A.P. Burke, *et al.*, *Am J Pathol*, 2000. **157**(4): p. 1259-1268.
34. Miserus, R.J., M.V. Herias, L. Prinzen, *et al.*, *JACC Cardiovasc Imaging*, 2009. **2**(8): p. 987-996.
35. Botnar, R.M., A.S. Perez, S. Witte, *et al.*, *Circulation*, 2004. **109**(16): p. 2023-2029.
36. Flacke, S., S. Fischer, M.J. Scott, *et al.*, *Circulation*, 2001. **104**(11): p. 1280-1285.
37. Spuentrup, E., R.M. Botnar, A.J. Wiethoff, *et al.*, *Eur Radiol*, 2008. **18**(9): p. 1995-2005.
38. Burtea, C., S. Laurent, O. Murariu, *et al.*, *Cardiovasc Res*, 2008. **78**(1): p. 148-157.
39. Winter, P.M., A.M. Morawski, S.D. Caruthers, *et al.*, *Circulation*, 2003. **108**(18): p. 2270-2274.
40. Sosnovik, D.E., E.A. Schellenberger, M. Nahrendorf, *et al.*, *Magn Reson Med*, 2005. **54**(3): p. 718-724.
41. Chen, J., C.H. Tung, J.R. Allport, *et al.*, *Circulation*, 2005. **111**(14): p. 1800-1805.
42. Nahrendorf, M., D.E. Sosnovik, P. Waterman, *et al.*, *Circ Res*, 2007. **100**(8): p. 1218-1225.
43. Meoli, D.F., M.M. Sadeghi, S. Krassilnikova, *et al.*, *J Clin Invest*, 2004. **113**(12): p. 1684-1691.
44. Caravan, P., B. Das, S. Dumas, *et al.*, *Angew Chem Int Ed Engl*, 2007. **46**(43): p. 8171-8173.
45. Helm, P.A., B.A. French, P. Caravan, *et al.*, *Molecular imaging of collagenous scar tissue in chronic myocardial infarction using a targeted contrast agent*. 2007, ISMRM. p. 864.
46. McAteer, M.A., N.R. Sibson, C. von Zur Muhlen, *et al.*, *Nat Med*, 2007. **13**(10): p. 1253-1258.
47. Breckwoldt, M.O., J.W. Chen, L. Stangenberg, *et al.*, *Proc Natl Acad Sci U S A*, 2008. **105**(47): p. 18584-18589.
48. Cagnin, A., D.J. Brooks, A.M. Kennedy, *et al.*, *Lancet*, 2001. **358**(9280): p. 461-467.

49. Klohs, J., M. Grafe, K. Graf, *et al.*, *Stroke*, 2008. **39**(10): p. 2845-2852.
50. Higuchi, M., N. Iwata, Y. Matsuba, *et al.*, *Nat Neurosci*, 2005. **8**(4): p. 527-533.
51. Dimou, E., J. Booij, M. Rodrigues, *et al.*, *Curr Alzheimer Res*, 2009. **6**(3): p. 312-319.
52. Massoud, T.F., S.S. Gambhir, *Genes Dev*, 2003. **17**(5): p. 545-580.
53. Nunn, A.D., K.E. Linder, M.F. Tweedle, *Q J Nucl Med*, 1997. **41**(2): p. 155-162.
54. Phelps, M.E., *Proc Natl Acad Sci U S A*, 2000. **97**(16): p. 9226-9233.
55. Bogdanov, A., Jr., L. Matuszewski, C. Bremer, *et al.*, *Mol Imaging*, 2002. **1**(1): p. 16-23.
56. Kluza, E., D.W. van der Schaft, P.A. Hautvast, *et al.*, *Nano Lett*, 2010. **10**(1): p. 52-58.
57. Nagayasu, A., K. Uchiyama, H. Kiwada, *Adv Drug Deliv Rev*, 1999. **40**(1-2): p. 75-87.
58. Terreno, E., S. Geninatti Crich, S. Belfiore, *et al.*, *Magn Reson Med*, 2006. **55**(3): p. 491-497.
59. Brekke, C., S.C. Williams, J. Price, *et al.*, *Neuroimage*, 2007. **37**(3): p. 769-782.
60. Brekke, C., S.C. Morgan, A.S. Lowe, *et al.*, *NMR Biomed*, 2007. **20**(2): p. 77-89.
61. Kobayashi, H., S. Kawamoto, T. Saga, *et al.*, *Bioconjug Chem*, 2001. **12**(4): p. 587-593.
62. Lewin, M., O. Clement, P. Belguise-Valladier, *et al.*, *Invest Radiol*, 2001. **36**(1): p. 9-14.
63. Geninatti Crich, S., C. Cabella, A. Barge, *et al.*, *J Med Chem*, 2006. **49**(16): p. 4926-4936.
64. Zhang, Z., E.J. van den Bos, P.A. Wielopolski, *et al.*, *Magma*, 2005. **18**(4): p. 175-185.
65. Mulder, W.J., R. Koole, R.J. Brandwijk, *et al.*, *Nano Lett*, 2006. **6**(1): p. 1-6.
66. Sheu, J.R., M.H. Yen, Y.C. Kan, *et al.*, *Biochim Biophys Acta*, 1997. **1336**(3): p. 445-454.
67. Koning, G.A., R.M. Schiffelers, M.H. Wauben, *et al.*, *Arthritis Rheum*, 2006. **54**(4): p. 1198-1208.
68. Koch, A.E., M.M. Halloran, C.J. Haskell, *et al.*, *Nature*, 1995. **376**(6540): p. 517-519.
69. Caswell, P.T., J.C. Norman, *Traffic*, 2006. **7**(1): p. 14-21.
70. Muller, R.H., K. Mader, S. Gohla, *Eur J Pharm Biopharm*, 2000. **50**(1): p. 161-177.
71. Mulder, W.J., G.J. Strijkers, G.A. van Tilborg, *et al.*, *NMR Biomed*, 2006. **19**(1): p. 142-164.
72. Reulen, S.W., W.W. Brusselaars, S. Langereis, *et al.*, *Bioconjug Chem*, 2007. **18**(2): p. 590-596.
73. Nobs, L., F. Buchegger, R. Gurny, *et al.*, *J Pharm Sci*, 2004. **93**(8): p. 1980-1992.



## Chapter **2**

### **The cellular compartmentalization of internalized paramagnetic liposomes strongly influences both $T_1$ and $T_2$ relaxivity**

**Based on:**

*The cellular compartmentalization of internalized paramagnetic liposomes strongly influences both  $T_1$  and  $T_2$  relaxivity*

M.B. Kok, S. Hak, W.J.M. Mulder, D.W.J. van der Schaft, G.J. Strijkers, K. Nicolay

Magnetic Resonance in Medicine, 2009. **61**(5): p. 1022-32



**Abstract:**

In recent years, numerous  $Gd^{3+}$ -based contrast agents have been developed to enable target-specific MR imaging of *in vivo* processes at the molecular level. The combination of powerful contrast agents and amplification strategies, aimed at increasing the contrast agent dose at the target site, is an often-used strategy to improve the sensitivity of biomarker detection. One such amplification mechanism is to target a disease-specific cell membrane receptor that can undergo multiple rounds of internalization following ligand binding and thus shuttle a sizeable amount of contrast agent into the target cell. An example of such a membrane receptor is the  $\alpha_v\beta_3$  integrin. The goal of this study was to investigate the consequences of this amplification approach for the  $T_1$ - and  $T_2$ -shortening efficacy of a paramagnetic contrast agent. Cultured endothelial cells were incubated with paramagnetic liposomes that were conjugated with a cyclic RGD-peptide to enable internalization via the  $\alpha_v\beta_3$  integrin receptor. Non-targeted liposomes served as a control. This study showed that  $\alpha_v\beta_3$  targeting dramatically increased the uptake of paramagnetic liposomes. This targeting strategy, however, strongly influenced both the longitudinal and transverse relaxivity of the internalized paramagnetic liposomes.

## Introduction

$Gd^{3+}$ -based contrast agents are used in a multitude of magnetic resonance imaging (MRI) applications. An emerging application is molecular MR imaging, in which targeted contrast agents are used to visualize sparse molecular epitopes expressed as a consequence of pathological processes. Particularly the targeting of markers that are readily accessible from the blood stream has been studied with considerable success, *e.g.* in cancer, atherosclerosis and myocardial infarction [1-4]. Besides the imaging of disease processes,  $Gd^{3+}$ -based contrast agents have also been used for *in vitro* labeling of cells, allowing their tracking with MRI after implantation in for instance the brain [5, 6], the kidney [7], following stroke [8], and in tumor models [9].

For many *in vivo* processes, specific molecular markers are present in very low concentrations ranging from approximately  $10^{-9}$  to  $10^{-13}$  mol/g [10]. Therefore, the success of molecular MRI strictly depends on the use of technologies that lead to an as large as possible effect on the relaxation rate of water protons. Up to now, improving the efficacy of molecular MR imaging with paramagnetic contrast agents has mainly focused on the incorporation of high payloads of gadolinium, *e.g.* in liposomes, dendrimers, micelles and micro-emulsions [11, 12] as well as on the design of gadolinium chelates that have higher molar relaxivities like Gd-HOPO [13], Gd-cyclo-PCTA12 [14] and Gd-AAZTA [15]. A third option to improve the detection sensitivity is to make use of amplification strategies to reach as high a dose of contrast agent as possible at the targeted site. One such option in case of angiogenesis imaging is targeting the  $\alpha_v\beta_3$  integrin using for instance an RGD-peptide sequence. This specific integrin has been used as a target in several studies using a variety of imaging techniques including MRI, ultrasound, PET, SPECT, and NIRF [16]. An attractive feature of the  $\alpha_v\beta_3$  integrin for amplification purposes is its fast recycling kinetics. After ligand binding and endocytosis, the  $\alpha_v\beta_3$  integrin proceeds to early endosomes. There, the integrin is either recycled to the cellular membrane immediately (short loop) or further trafficked to the perinuclear recycle center and subsequently recycled to the cellular membrane (long loop). These recycling loops have a median duration of typically 3 min for the short loop and 10 min for the long loop [17]. This suggests that targeting of the  $\alpha_v\beta_3$  integrin provides an excellent amplification strategy that will lead to a high dose of contrast agent inside the targeted cells. Since  $Gd^{3+}$ -based contrast agents strongly depend on the kinetics of water proton exchange between the  $Gd^{3+}$ -ion and the bulk water, it is of key importance to study the uptake of contrast agent on the cellular level and the effect of cellular location and concentration on longitudinal ( $T_1$ ) and transverse ( $T_2$ ) relaxation, especially if large doses of contrast agent are taken up.

To that aim, the present study made use of an *in vitro* approach in which human umbilical vein derived endothelial cells (HUVECs) served as a model system that exhibits abundant expression of the  $\alpha_v\beta_3$  integrin [18]. The integrin was targeted using a cyclic RGD-peptide conjugated to liposomes that contained both amphiphilic Gd-chelates and fluorescent lipids. Liposomes without the cyclic RGD-peptide served as a control system for non-specific uptake. The association and uptake of contrast agents by the cells was monitored using several techniques. Confocal laser scanning microscopy (CLSM) was used to determine the cellular location of the contrast agent. Furthermore,  $T_1$ - and  $T_2$ -measurements of loosely packed cell pellets were combined with inductively coupled plasma atomic emission spectrometry (ICP-AES) to determine both the longitudinal and transverse relaxivity of cell associated contrast agent. A toxicology assay provided insights in the possible cytotoxic effect of the liposomal contrast agent.

## Methods

### Materials

1,2-Distearoyl-*sn*-glycero-3-phosphocholine (DSPC), cholesterol, 1,2-distearoyl-*sn*-glycero-3-phosphoethanolamine-N-[methoxy(polyethyleneglycol)-2000] (PEG<sub>2000</sub>-DSPE), 1,2-distearoyl-*sn*-glycero-3-phosphoethanolamine-N-[maleimide(polyethyleneglycol)-2000] (Mal-PEG<sub>2000</sub>-DSPE) and 1,2-dipalmitoyl-*sn*-3-phosphoethanolamine-N-[lissamine rhodamine B sulfonyl] (rhodamine-PE) were obtained from Avanti Polar Lipids (Alabaster, AL, USA). Gd-diethylenetriaminepentaacetic acid-bis(stearylamide) (Gd-DTPA-BSA) was purchased from Gateway Chemical Technology (St. Louis, MO, USA). Endothelial Growth Medium-2 (EGM-2) and human umbilical vein derived endothelial cells (HUVECs) were ordered with Lonza Bioscience (Switzerland). Monoclonal mouse anti-human CD31 antibody was obtained from Dakocytomation (Glostrup, Denmark). Polyclonal rabbit anti- $\alpha_v\beta_3$  integrin primary antibody was purchased from Millipore (Billerica, MA, USA). DAPI, Alexa Fluor 488 conjugated goat anti-mouse secondary antibody and Alexa Fluor 488 conjugated goat anti-rabbit secondary antibody were from Molecular Probes Europe BV (Leiden, The Netherlands). Cyclic RGD, c(RGDf(-S-acetylthioacetyl)K) and c(RGDfK), was synthesized by Ansynth Service BV (Roosendaal, The Netherlands). All other chemicals were obtained from Sigma (St. Louis, MO, USA) and were of analytical grade or the best grade available.

### Liposome preparation and characterization:

200 nm-diameter liposomes containing Gd-DTPA-BSA, DSPC, cholesterol, PEG<sub>2000</sub>-DSPE and Mal-PEG<sub>2000</sub>-DSPE at a molar ratio of 0.75/1.10/1/0.075/0.075 were produced by lipid film hydration and extrusion according to Mulder *et al.* [19]. In short, the lipids were dissolved in a 1:5 methanol:chloroform mixture. As a fluorescent marker, 0.1 mole percent of rhodamine-PE was added. A lipid film was created by evaporating the chloroform/methanol mixture using a Rotavapor R200 (Buchi, Flawil, Switzerland). Then the lipid film was hydrated at 67 °C using a HEPES buffered saline solution (HBS), containing 20 mM HEPES and 135 mM NaCl (pH 6.7). The lipid suspension was extruded at 67 °C, twice through a single 200 nm polycarbonate membrane (Whatman, Kent, UK) and 6 times through a double 200 nm polycarbonate membrane. After extrusion, half of the liposome suspension was modified with a cyclic RGD-peptide (6 µg/µmol total lipid) to target the  $\alpha_v\beta_3$ -integrin. The cyclic RGD-peptide was deacetylated and coupled to the distal end of Mal-PEG<sub>2000</sub>-DSPE. After incubation overnight, at 4 °C, both batches of liposomes were centrifuged at 310,000 g for 45 min. Centrifugation was used, in case of RGD-liposomes, to remove unconjugated RGD-peptide. The pellets were resuspended in HBS, pH 7.4. Lipid concentration

was measured by phosphate determination according to Rouser *et al.* [20]. Size and size-distribution of the liposomes was determined with dynamic light scattering (DLS) (Zetasizer Nano, Malvern, UK). Both the longitudinal and transverse relaxivity were determined by fitting  $R_1$  ( $1/T_1$ ) and  $R_2$  ( $1/T_2$ ) values as a function of the gadolinium concentration of the liposome suspension as determined using inductively coupled plasma atomic emission spectroscopy (ICP-AES) by Philips Research (Eindhoven, The Netherlands), using the least squares method. In the remainder of this paper we refer to liposomes that were conjugated with RGD as RGD-liposomes. Non-targeted liposomes that were not conjugated with a targeting ligand will be referred to as NT-liposomes.

#### Cell Culture:

Human umbilical vein derived endothelial cells (HUVECs) were used in all experiments. Cells were stored in liquid nitrogen upon arrival. Before use, the cells were quickly thawed in a water bath ( $T = 37\text{ }^\circ\text{C}$ ) and divided over 2 gelatin coated T75 TCPS flasks (VWR, West Chester, PA, USA). Cells were cultured in a humidified incubator at  $37\text{ }^\circ\text{C}$  with 5%  $\text{CO}_2$ . The EGM-2 medium was replaced every 2-3 days. Cells were subcultures at 80-90% confluency according to procedures provided by Lonza Bioscience (Switzerland).

#### Experimental Setup

Cells of passage 3 or 4 were used for all experiments at 80-90% confluency. Incubation was carried out on both gelatin-coated coverslips, for CLSM analysis, and in gelatin-coated T75 TCPS culture flasks, for MRI, FACS and ICP-AES analysis. All measurements were done in triplicate for both types of liposomes and each incubation time. To start the experiment, medium was replaced by either RGD-liposome or NT-liposome containing medium at a concentration of  $1\text{ }\mu\text{mol}$  total lipid per ml. 4 mL of liposome containing medium was added to the T75 gelatin-coated TCPS flasks and 0.5 mL of medium was added to the gelatin-coated coverslips. The incubation time with liposome containing medium was varied between 0 and 24 hr. After incubation, the cells were washed twice with 5 mL prewarmed ( $37\text{ }^\circ\text{C}$ ) medium and once with 5 mL prewarmed ( $37\text{ }^\circ\text{C}$ ) HEPES-buffered saline solution to remove non-adherent liposomes. After these washing steps, the cells grown on coverslips were fixed using 4% PFA for 15 min at room temperature. Cells in culture flasks were detached using 2 mL 0.25% trypsin 1 mM EDTA·4Na (Lonza Bioscience, Switzerland). The trypsin solution was neutralized using 4 mL trypsin neutralizing solution (Lonza Bioscience, Basel, Switzerland). Cells were spun down at 220 g and the supernatant was removed and the cell pellet was resuspended in 150  $\mu\text{L}$  4% paraformaldehyde solution in PBS and transferred to a 300  $\mu\text{L}$  Eppendorf cup. A

loosely-packed cell pellet was allowed to form by 4 days of storage in the dark at 4 °C.

#### Variation of the number of RGD-peptides per liposome

A single batch of liposomes was divided equally in 8 falcon tubes. Different amounts (0, 0.012, 0.03, 0.06, 0.12, 0.6, 1.2, 6.0  $\mu\text{g}/\mu\text{mol}$  total lipid) of RGD-peptide were added to the falcon tubes to obtain liposomes containing a different net number of RGD peptides per liposome. The number of RGD-peptides was estimated assuming  $4.2 \cdot 10^5$  lipids per liposome, a yield of 70% after extrusion and near complete coupling efficiency of the RGD-peptide. HUVECs of passage 4 were incubated for 6 hr with liposomes containing a varying number of RGD-peptides (0-5000) to assess uptake efficiency.

#### Lysotracker green

HUVECs of passage 3 were cultured on a gelatin coated Lab-Tek II chambered coverglasses (Thermo Fisher Scientific, Waltham, MA, USA) and incubated for 6 hr with both RGD-liposomes, using a concentration of 1  $\mu\text{mol}$  total lipid per ml, and Lysotracker green (Invitrogen, Carlsbad, CA USA), at a concentration of 1.5  $\mu\text{M}$ . After 6 hr of incubation the cells were rinsed three times with 2 mL of medium and subsequently analyzed using CLSM.

#### Magnetic Resonance Imaging of cell pellets

The  $T_1$  and  $T_2$  relaxation times and the volume of the pellets were measured using a 6.3 T horizontal bore animal MR scanner (Bruker, Ettlingen, Germany). All measurements were carried out at room temperature. Longitudinal and transverse relaxation times were measured in a 3 cm diameter send and receive quadrature-driven birdcage coil (Rapid Biomedical, Würzburg, Germany). The Eppendorf tubes containing the loosely-packed cell pellets were placed in a custom made holder (4 tubes at a time) that was filled with HEPES buffered saline solution to facilitate shimming.  $T_1$  was measured using a fast inversion recovery segmented FLASH sequence with an echo time (TE) of 1.5 ms, a repetition time (TR) of 3.0 ms, a flip angle of  $60^\circ$ , and an inversion time (TI) ranging from 67 ms to 4800 ms in 80 steps. Overall repetition time was 20 s. Field of view (FOV) was  $3 \times 3 \text{ cm}^2$ , using a matrix size of  $128 \times 128$ , a slice thickness of 0.75 mm and 2 averages.  $T_2$  was measured using a multi-slice multi-echo sequence with TE ranging between 9 and 288 ms in 32 steps and a TR of 1000 ms. FOV was  $3 \times 2.2 \text{ cm}^2$ , slice thickness was 0.75 mm using a matrix size of  $128 \times 128$ . Number of averages was 4. From the images a  $T_1$ - or  $T_2$ -map was calculated using Mathematica (Wolfram Research Inc, Champaign, IL, USA).  $T_1$  and  $T_2$  of the different cell pellets were determined by selecting a region-of-interest within the pellet.  $T_1$ -weighted images were measured using a multi-slice

spin-echo sequence with TE = 10.3 ms and TR = 500 ms. FOV was 3x3 cm<sup>2</sup>, slice thickness was 0.75 mm using a matrix size of 256x192. Number of averages was 1. The volume of the cell pellet was determined for each sample separately in a 0.7 cm diameter solenoid coil using a 3D FLASH sequence with TE = 3.2 ms, TR = 25 ms and a flip angle of 30°. FOV was 1.6x1.6x1.6 cm<sup>3</sup>, matrix size was 128x128x128. Number of averages was 1. Pellet volume was determined by manually setting threshold values to select the voxels inside the pellet. The remaining voxels were multiplied by the voxel volume to obtain the total volume of the pellet. The concentration of gadolinium in each cell pellet was determined by dividing the gadolinium content as determined by ICP-AES by the pellet volume.

#### Immunofluorescence

After fixation, the coverslips with HUVECs incubated with liposomes were stained using a mouse anti-human CD31 antibody to visualize the cellular membrane. The cells were rinsed for 5 min with PBS followed by 60 min of incubation with the primary mouse anti-human CD31 antibody (1:40 dilution). Subsequently the cells were washed 3x 5 min with PBS followed by 30 min of incubation with a secondary Alexa Fluor 488 goat anti-mouse IgG antibody (1:200 dilution). The cells were washed 3x 5 min with PBS and the nuclei were stained for 5 min with DAPI. After staining of the nuclei the cells were rinsed 3x 5 min with PBS and subsequently mounted on a microscopy slide using Mowiol Mounting Medium.

For staining of the  $\alpha_v\beta_3$  integrin, first a 15 min blocking step was used, consisting of incubation with 5% (v/v) rabbit serum in PBS, which was followed by incubation with the primary mouse anti- $\alpha_v\beta_3$  integrin antibody (1:50 dilution) for 60 min. Next, the cells were rinsed 3x 5 min with PBS and subsequently incubated with Alexa Fluor 488 goat anti-mouse IgG antibody (dilution 1:200) for 1 hr. Then cells were washed 3x 5 min with PBS and the nuclei were stained for 5 min with DAPI. After staining of the nuclei the cells were rinsed 3x 5 min with PBS and subsequently mounted on a microscopy slide using Mowiol Mounting Medium.

#### Confocal Laser Scanning Microscopy

Confocal fluorescence images were recorded at room temperature on a Zeiss LSM 510 META system using a Plan-Apochromat<sup>®</sup> 63x/1.4 NA oil-immersion objective. Alexa Fluor 488 and rhodamine-PE were excited using the 488 and 543 nm line of a HeNe laser, respectively. The fluorescence emission of Alexa Fluor 488 and Lysotracker green were recorded with photomultiplier tubes (Hamamatsu R6357) after spectral filtering with a NFT 490 nm beamsplitter

followed by a 500-550 nm bandpass filter. Rhodamine-PE emission was analyzed using the Zeiss Meta System in a wavelength range of 586-704 nm. DAPI staining of nuclei was visualized by two-photon excitation fluorescence microscopy performed on the same Zeiss LSM 510 system. Excitation at 780 nm was provided by a pulsed Ti:Sapphire laser (Chameleon™; Coherent, Santa Clara, CA, USA), and fluorescence emission was detected with a 395-465 nm bandpass filter. All experiments were combined in multitrack mode and acquired confocally.

#### Toxicology

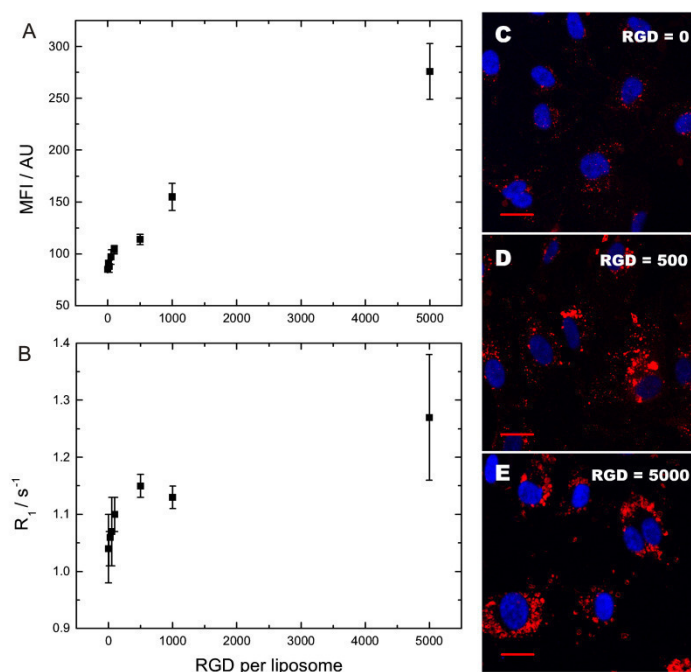
HUVECs were seeded into 96-well plates ( $5 \cdot 10^3$  cells/well) and cultured overnight prior to the experiment in a humidified incubator (5% CO<sub>2</sub>, 37 °C). Culture medium was removed and replaced by culture medium containing liposomes or unconjugated RGD-peptides. Seven groups were defined; 1) RGD-liposomes, 2) NT-liposomes, 3) RGD-liposomes without rhodamine-PE and Gd-DTPA-BSA, 4) NT-liposomes without rhodamine-PE and Gd-DTPA-BSA, 5) RGD-liposomes without rhodamine-PE, 6) NT-liposomes without rhodamine-PE, and 7) RGD-peptide. For liposomes that did not contain the Gd-DTPA-BSA, the gadolinium containing lipid was replaced by an equivalent amount of DSPC. HUVECs were incubated for 24 hr with a concentration of either 1 or 5 mM total lipid, or in case of free RGD-peptide, an equal concentration of RGD-peptide as present in the RGD-liposome suspension (6 and 30 µg/ml, respectively). After incubation with the liposomes, the cell viability was measured using the XTT assay as described by Scudiero *et al.* [21].



## Results

### *Liposome characteristics*

To study the effect of cellular uptake of contrast agents on  $T_1$  and  $T_2$  relaxation rates, RGD- and NT-liposomes were prepared. After centrifugation, typical lipid concentrations of approximately 30 mM in the final liposome suspension were obtained. DLS showed a single peak in intensity mode with a z-average of 185 nm for both RGD- and NT-liposomes and a poly dispersity index (PDI) of 0.18 for RGD-liposomes and 0.16 for NT-liposomes. Longitudinal and transverse relaxivity were determined at 6.3 T and 20°C. Measurements showed  $r_1 = 2.1 \pm 0.1 \text{ mM}^{-1}\text{s}^{-1}$  and  $2.3 \pm 0.1 \text{ mM}^{-1}\text{s}^{-1}$ , and  $r_2 = 17.3 \pm 0.1 \text{ mM}^{-1}\text{s}^{-1}$  and  $19.6 \pm 0.1 \text{ mM}^{-1}\text{s}^{-1}$ , for RGD- and NT-liposomes, respectively.



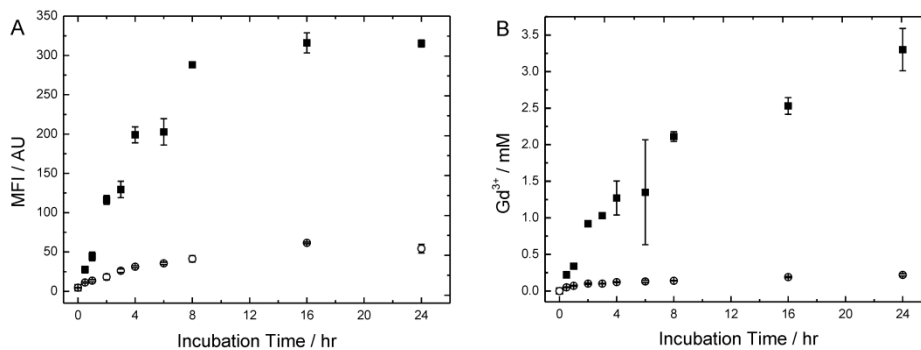
**Figure 1, Mean fluorescence intensity per cell (MFI) (A) and  $R_1$  (B) as a function of the number of RGD-peptides conjugated per liposome. Data represent mean  $\pm$  SD ( $n=3$ ). C-E) CLSM images of HUVECs incubated with liposomes containing 0, 500 and 5000 RGD-peptides per liposome, respectively. Blue = DAPI, red = rhodamine, red bar = 25  $\mu\text{m}$ . Note that the laser intensity used to obtain image C and D was eightfold higher than the intensity used to obtain image E.**

Figure 1A shows FACS data on the uptake of RGD-liposomes as a function of the number of conjugated RGD-peptides. The uptake of liposomes was increased for liposomes with higher number of peptides. Figure 1B shows the corresponding longitudinal relaxation rate ( $R_1$ ). Higher numbers of conjugated RGD-peptides led to an increase in  $R_1$ , although the increase in  $R_1$  between 500 and 5000

peptides per liposome was less profound. CLSM images of cells incubated with liposomes conjugated with 0, 500 and 5000 RGD peptides are shown in Figure 1C-E. Distinct differences can be observed between Figure 1C and E. Figure 1E shows larger accumulations (1-5  $\mu\text{m}$ ) than is the case in Figure 1C (0.4-1  $\mu\text{m}$ ). Figure 1D displays an intermediate situation with both small and large accumulations.

#### Cellular uptake of paramagnetic liposomes

After incubation of the cells with liposomes, the uptake of contrast agents was analyzed using FACS and inductively coupled plasma atomic emission spectrometry (ICP-AES). FACS was used to measure the rhodamine-PE content and ICP-AES was used to determine the gadolinium content of the HUVECs. Figure 2A shows the results of the FACS analysis with the mean fluorescence intensity of rhodamine-PE per cell as a function of incubation time.



**Figure 2, A) Mean fluorescence intensity per cell (MFI) as a function of incubation time and B) Gadolinium concentration as a function of incubation time for RGD-liposomes (solid squares) and NT-liposomes (open circles). Data represent mean  $\pm$  SD (n=3).**

Figure 2A clearly shows a higher uptake of RGD-liposomes compared to NT-liposomes. For both HUVECs incubated with RGD- or NT-liposomes an increase in fluorescence intensity was observed up to 8 hr of incubation. Thereafter the fluorescence intensity increased only slightly. In order to quantify the gadolinium content of the cells, ICP-AES was used. Figure 2B shows the gadolinium concentration in the pellets as a function of incubation time and a similar trend was observed as determined with FACS analysis. In pellets of HUVECs incubated with RGD-liposomes, the concentration of gadolinium increased from 0.22 mM after 0.5 hr of incubation up to 3.3 mM after 24 hr. In contrast, the uptake of NT-liposomes was much lower and the gadolinium concentration in the pellets varied from 0.05 mM (0.5 hr) and 0.22 mM (24 hr).

### Relaxometry

The  $R_1$  and  $R_2$  relaxation rates of HUVEC cell pellets were determined at 6.3 T as a function of the incubation time and, hence, the concentration of cell-associated gadolinium. Figure 3A shows the relationship between  $R_1$  and incubation time and illustrates that, although RGD-liposomes were taken up to a much larger extent than NT-liposomes, a similar range of  $R_1$  values was obtained. The relaxation rate ( $R_1$ ) of the HUVECs incubated with RGD-liposomes increased rapidly from a pre-incubation value of  $0.45 \text{ s}^{-1}$  to  $1.4 \text{ s}^{-1}$  at 8 hr. Thereafter, the  $R_1$  only slightly increased to a value of  $1.6 \text{ s}^{-1}$  at 24 hr of incubation. For incubations with NT-liposomes the  $R_1$  of the pellets increased in a similar fashion from  $0.45 \text{ s}^{-1}$  to a value of  $1.0 \text{ s}^{-1}$  at 8 hr. Thereafter the  $T_1$  relaxation rate showed a further increase to  $1.4 \text{ s}^{-1}$  for 16 and 24 hr of incubation. Longitudinal relaxation rates for HUVECs incubated with RGD-liposomes were only slightly higher than  $T_1$  relaxation rates for HUVECs incubated with NT-liposomes for incubation times of 16 and 24 hr.

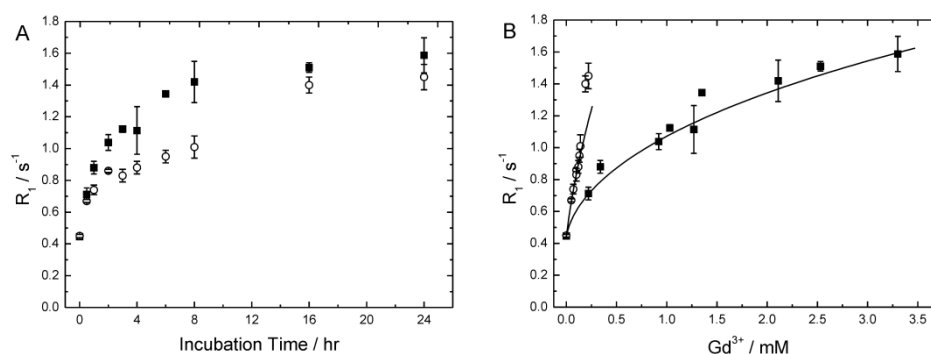


**Figure 3, A)  $R_1$  as a function of incubation time for HUVECs incubated with RGD-liposomes (solid squares) or NT-liposomes (open circles). B)  $R_1$  versus gadolinium concentration of HUVECs incubated with RGD-liposomes (solid squares) or NT-liposomes (open circles). Data represent mean  $\pm$  SD ( $n=3$ ). Solid lines represent model calculations as explained in the discussion and conclusions section.**

The small differences in longitudinal relaxation rates between pellets of HUVECs after incubation with either RGD-liposomes or NT-liposomes are further illustrated by Figure 4 in which  $T_1$ -weighted images of three different cell pellets, as measured at 6.3 T, are shown. Pellet A contained cells that were not incubated with contrast agent, while pellet B and C contained cells incubated for 2 hr with RGD- and NT-liposomes, respectively. Pellet A is essentially iso-intense with the medium above, whereas pellet B and C can easily be distinguished as a consequence of the reduced  $T_1$  caused by the incubation with either RGD- or NT-liposomes. Although the gadolinium concentration was 9-fold higher for the sample incubated with RGD-liposomes compared to sample C, similar signal

intensities were observed in these  $T_1$ -weighted images. This indicates a lower  $T_1$ -shortening efficacy of the cell-associated RGD-liposomes compared to the cell-associated NT-liposomes, as evident also in Figure 3.

The efficacy of a contrast agent is usually expressed as the relaxivity ( $r_1$  or  $r_2$ ) in  $\text{mM}^{-1}\text{s}^{-1}$ , which is the slope of the relaxation rate as a function of the gadolinium concentration. To get an indication of the relaxivity of cell-associated paramagnetic liposomes, relaxation rates were plotted as a function of the gadolinium concentrations of the pellets in Figure 3B. For NT-liposomes a linear relationship between  $R_1$  and  $[\text{Gd}^{3+}]$  was found. The slope was determined using the least squares method and resulted in a longitudinal relaxivity ( $r_1$ ) of  $4.7 \pm 0.3 \text{ mM}^{-1}\text{s}^{-1}$ . For RGD-liposomes a nonlinear relationship was found, that was indicative of a progressively reduced  $r_1$ , throughout the range of concentrations of gadolinium.

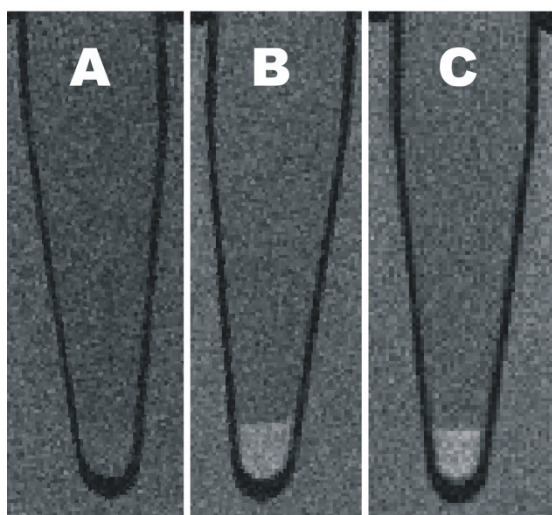


**Figure 4, Typical example of  $T_1$ -weighted images of cell pellets of HUVECs after: A) control incubation, B) 2hr incubation with RGD-liposomes, C) 2hr incubation with NT-liposomes.**

The slope at the beginning and at the end of the curve was determined by fitting a linear relationship through the first three points and the last three points, respectively. This resulted in an estimated  $r_1 = 1.3 \pm 0.1 \text{ mM}^{-1}\text{s}^{-1}$  in the low gadolinium concentration range and an  $r_1 = 0.1 \pm 0.1 \text{ mM}^{-1}\text{s}^{-1}$  in the high concentration range, indicating a remarkably lower relaxivity for higher levels of cell-associated contrast agent.

Transverse relaxation rates ( $R_2$ ) versus incubation time are plotted in Figure 5A.  $R_2$  increased from  $14 \text{ s}^{-1}$  to  $100 \text{ s}^{-1}$  in pellets of HUVECs incubated with RGD-liposomes. In contrast,  $R_2$  for HUVECs incubated with NT-liposomes only increased from  $14 \text{ s}^{-1}$  to  $19 \text{ s}^{-1}$ . To get estimates of the transverse relaxivity, the transverse relaxation rates were plotted versus the gadolinium concentration in

Figure 5B and C. In contrast to  $R_1$  as a function of  $[\text{Gd}^{3+}]$ , an essentially linear relationship was found for incubations with both RGD-liposomes and NT-liposomes. Using the least squares method, the transverse relaxivity ( $r_2$ ) was determined, which resulted in  $r_2 = 26.9 \pm 1.2 \text{ mM}^{-1}\text{s}^{-1}$  for RGD-liposomes (Figure 5B) and  $r_2 = 15.6 \pm 2.8 \text{ mM}^{-1}\text{s}^{-1}$  for NT-liposomes (Figure 5C).

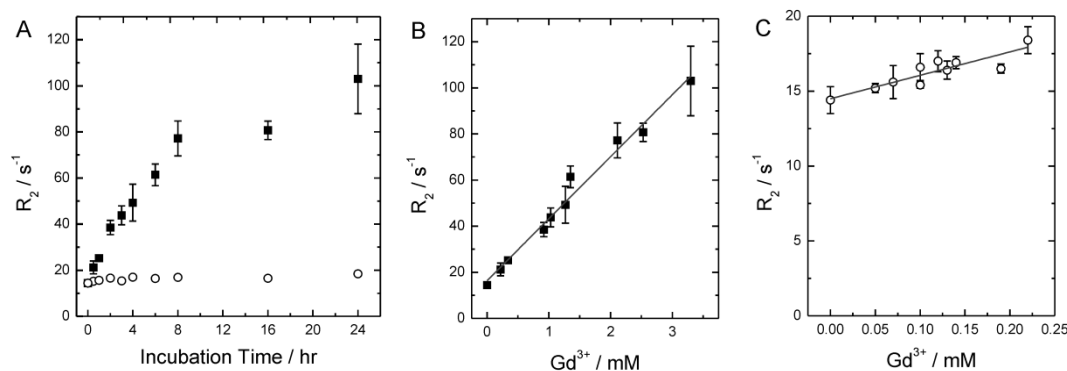


**Figure 5, A)  $R_2$  as a function of incubation time for pellets of HUVECs incubated with either RGD-liposomes (solid squares) or NT-liposomes (open circles). B,C)  $R_2$  as a function of  $[\text{Gd}^{3+}]$  for HUVECs incubated with RGD-liposomes (B) and NT-liposomes (C). Solid lines are linear fits to the experimental data resulting in  $r_2 = 26.9 \pm 1.2 \text{ mM}^{-1}\text{s}^{-1}$  and  $15.6 \pm 2.8 \text{ mM}^{-1}\text{s}^{-1}$  for RGD- and NT-liposomes, respectively. Data represent mean  $\pm$  SD ( $n=3$ ).**

### Microscopy

The cellular location of the liposomal contrast agent was determined using CLSM, by exploiting the rhodamine-PE present in the bilayer of the liposomes. Figure 6 shows confocal images of HUVECs grown on gelatin coated coverslips incubated with either RGD- or NT-liposomes. Cell morphology changed during the experiment, *i.e.* confluency increased from 80% to approximately 100%, due to cell proliferation. Both RGD- and NT-liposomes accumulated in the perinuclear region. However, clear differences in uptake between RGD- and NT-liposomes were observed. Up to at least 6 hr of incubation, the RGD-liposomes were mainly located in the perinuclear region in spherical 1-5  $\mu\text{m}$  diameter vesicles. After 6-8 hr of incubation, also more diffuse patterns were observed throughout the cytoplasm. After 24 hr of incubation with RGD-liposomes, the contrast agent was found throughout almost the entire cell. Incubation with NT-liposomes, on the other hand, resulted in a perinuclear intracellular distribution in sharply defined 0.4-1.0  $\mu\text{m}$  diameter spherical vesicles (up to 24 hr of incubation). No detectable association of liposomes with the cellular membrane was observed for both RGD- and NT-liposome incubated HUVECs.

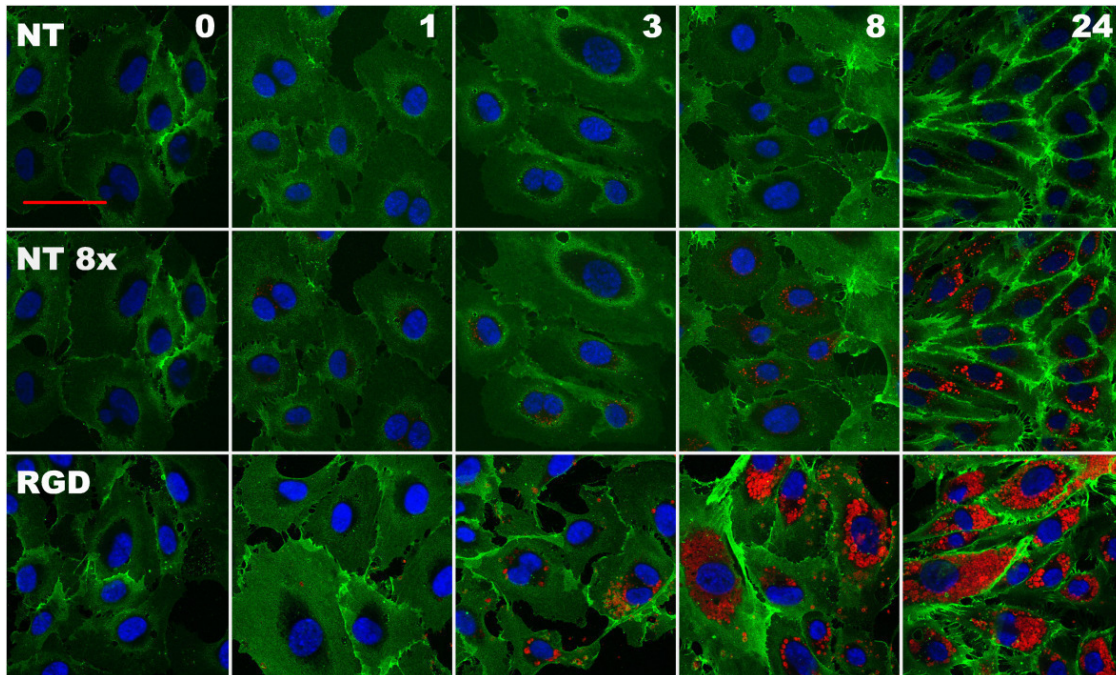


**Figure 6, CLSM images of HUVECs incubated with RGD-liposomes (RGD) or NT-liposomes (NT). Blue = DAPI, red = rhodamine, green = CD31, red bar = 50 $\mu$ m. The number shown in the top right corner of each column shows the incubation time in hours. Note that the laser intensity used to obtain NT 8x images (middle row) was eightfold higher than the intensity used to obtain the other images (bottom and top row).**

To further investigate the cell trafficking of the liposomes, the  $\alpha_v\beta_3$  integrin was visualized by immunofluorescence (Figure 7A and B). The images in Figure 7A and B were taken after 16 hr of incubation with either RGD-liposomes (A) or NT-liposomes (B). The integrin was detected both in the cytoplasm of the cell as well as on the cellular membrane. The intracellular location was observed for all incubation times. The magnification in the top left corner of Figure 7A provides clear evidence for association of  $\alpha_v\beta_3$  integrin to vesicles that are also positive for rhodamine-PE. For incubations with NT-liposomes, most of the rhodamine-PE positive vesicles were  $\alpha_v\beta_3$  negative (Figure 7B). Figure 7C and D show CLSM images of HUVECs incubated for 6 hr with both RGD-liposomes and LysoTracker green, a well known marker for acidic intracellular vesicles, like lysosomes. The arrowheads point to vesicles that showed colocalization of rhodamine PE and LysoTracker green. All rhodamine PE positive vesicles were LysoTracker green positive. As a control Figure 7E and F show CLSM images of HUVECs incubated for 6 hr with RGD-liposomes only, demonstrating that rhodamine-PE did not cause positive signal in the green channel (Figure 7F).



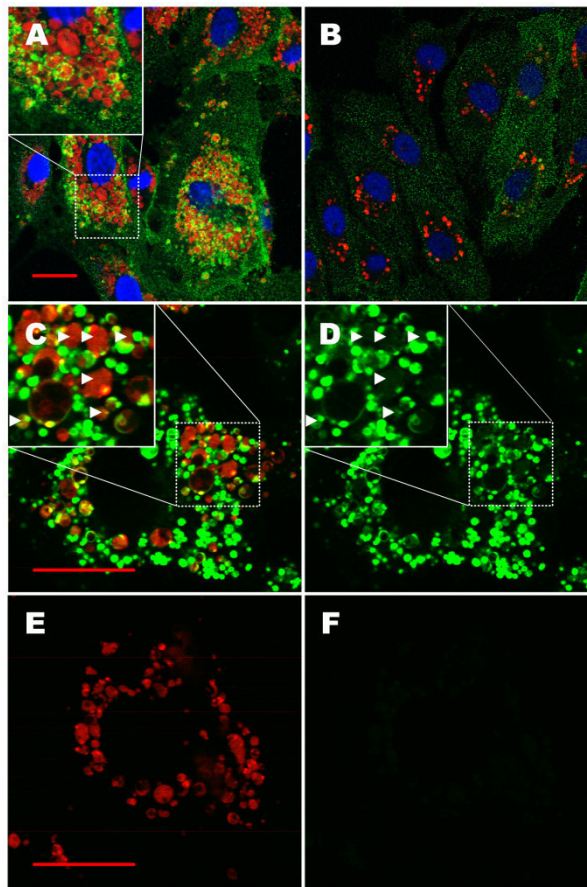


**Figure 7, A-B)** CLSM images of HUVECs stained for  $\alpha_v\beta_3$  integrin (green) incubated with RGD-liposomes (A) and incubated with NT-liposomes (B) for 16 hr. **C-D)** CLSM images of a single HUVEC incubated with Lysotracker green (green) and RGD liposomes (red): (C) merged image of the Lysotracker green and rhodamine channel and (D) the Lysotracker green channel alone. Arrowheads point to areas that show colocalization of rhodamine PE and Lysotracker green. The insets in frame A, C and D show magnifications of the areas indicated by the squares. **E-F)** CLSM images of a single HUVEC incubated with RGD liposomes; merged image of green and rhodamine channel (E) and the green channel only (F), indicating that the green signal as observed in C and D originates from Lysotracker green only. Blue = DAPI, red = rhodamine, red bar = 25  $\mu\text{m}$ .

### Toxicology assay

An XTT assay was performed to determine, whether the present findings were compromised by potential cytotoxic effects of the liposomal contrast agent. In Figure 8, the results are shown of incubations with different types of liposomes. Seven groups were defined to assess the potential cytotoxic effects of three components of the liposome, *i.e.* Gd-DTPA-BSA, rhodamine-PE and the RGD-peptide. Two lipid concentrations were used; 1 mM total lipid concentration, which was used throughout the experiment and a 5 times higher concentration was used to ensure detection of potential cytotoxic effects. The first two

columns show that the paramagnetic liposomes exhibited no cytotoxic effect when probed by the XTT assay. This is further explored by experiments with liposomes in which the gadolinium lipid was replaced by DSPC (column 3 and 4). To test whether there might be any cytotoxic effect of rhodamine-PE, liposomes were used that did not contain rhodamine-PE. No negative effect of rhodamine-PE on cell viability was observed (column 5 and 6). Finally, HUVECs were incubated with non-conjugated cyclic RGD-peptide to test if the peptide itself showed any cytotoxic effects. No adverse effect was observed for the peptide (column 7).

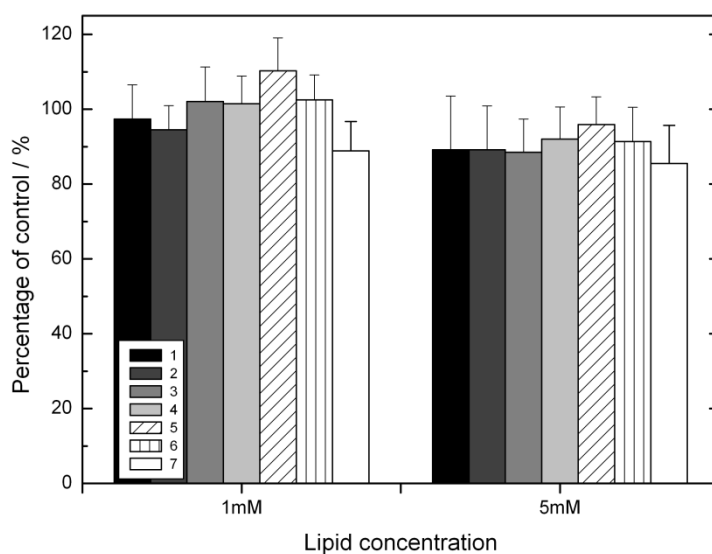


**Figure 8, Cytotoxicity tests of different liposome formulations and the RGD-peptide. Seven different conditions were tested and normalized to control incubated cells; 1) RGD-liposomes, 2) NT-liposomes, 3) RGD-liposomes without rhodamine-PE and Gd-DTPA-BSA, 4) NT-liposome without rhodamine-PE and Gd-DTPA-BSA, 5) RGD-liposomes without rhodamine-PE, 6) NT-liposomes without rhodamine-PE and 7) free RGD-peptide. Data represent mean  $\pm$  SD (n=12).**



### Discussion and Conclusions

In this chapter an *in vitro* approach was used to study the effect of cellular uptake of paramagnetic liposomes on  $T_1$  and  $T_2$  relaxation rates. First, the effect of the number of RGD-peptides conjugated to individual liposomes was investigated. An increase in number of RGD-peptides per liposome led to an increase in both the uptake of liposomes, as was previously described by Koning *et al.* [22], as well as to an increase in the  $R_1$ . All subsequent incubations were carried out with liposomes containing approximately 5000 RGD-peptides per liposome to ensure high uptake. FACS and ICP-AES analysis showed that RGD-conjugated liposomes were taken up to a much larger extent than NT-liposomes. Remarkably, no large differences in longitudinal relaxation rates were observed when comparing pellets of HUVECs incubated with RGD-liposomes with pellets incubated for the same duration with NT-liposomes. For RGD-liposomes a nonlinear relationship between longitudinal relaxation rates and the gadolinium concentration was found, that was indicative of a reduced  $r_1$ , throughout the range of concentrations of gadolinium, whereas for incubation with NT-liposomes a linear relationship was found. Transverse relaxation rates also showed clear differences between RGD- and NT-liposome incubations displaying a linear relationship with gadolinium concentration in both cases. XTT assays revealed no cytotoxic effects for both the RGD- and the NT-liposomes. The internalization process was further investigated using CLSM and showed distinct differences in intracellular location of the targeted and non-targeted liposomal contrast agents.

We hypothesize that differences in the mechanism of uptake between the  $\alpha_v\beta_3$ -integrin targeted contrast agent and the untargeted contrast agent may explain the pronounced differences in  $T_1$  shortening as observed during this study. It is generally accepted that the formation of caveolae after binding of a ligand to the  $\alpha_v\beta_3$  integrin is the main mechanism of internalization of this receptor [17]. After ligand binding and endocytosis, the  $\alpha_v\beta_3$  integrin proceeds to early endosomes. There, the integrin is further trafficked to the perinuclear recycle center, followed by its recycling to the cellular membrane. CLSM images showed that the  $\alpha_v\beta_3$  integrin is present on the membranes of the vesicles containing RGD-liposomes in the perinuclear region. Colocalization of LysoTracker green and the rhodamine PE showed that liposomes were contained within lysosomal vesicles in the cell. NT-liposomes could be internalized by either non-specific endocytosis or pinocytosis. The latter two mechanisms are responsible for the uptake of substances dissolved or suspended in extracellular fluids into endosomal compartments. To explain the reduced longitudinal relaxivity of the RGD-liposomes after internalization by HUVECs, two parameters may play an

important role, *i.e.* the concentration of contrast agent in the intracellular vesicles after internalization and the size of these vesicles.

It is proposed that the membranes surrounding the cytoplasmic vesicles, in which the liposomes are concentrated, limit the water exchange that is needed for optimal longitudinal relaxation of water protons by paramagnetic contrast agents. When the concentration of contrast agent in the cytoplasmic vesicles is high, the longitudinal relaxation rate of the water inside the compartments will also be very high. However, the water inside these cytoplasmic vesicles is only a small fraction of the total amount of water present in an imaging voxel. Therefore, the exchange of water across the vesicular membranes plays an important role and could, in case of a high concentration of confined contrast agent, be the limiting factor for efficient exchange of magnetization between the vesicular and the cytoplasmic compartment.

The second parameter that could have influenced the relaxivity is the size of the cytoplasmic vesicles containing the contrast agent. CLSM data showed an increase in size of the cytoplasmic vesicles containing RGD-liposomes over time. This increase in size reduces the surface-to-volume ratio of the vesicle and therefore lowers the water exchange over the vesicular membrane, thus reducing the effective longitudinal relaxivity. The size of the vesicles in case of NT-liposomes, also increased over time, but remained smaller than the vesicles found after incubation with RGD-liposomes.

The differences in the observed longitudinal relaxivity between NT- and RGD-liposomes can be understood in more detail within the framework of a 3-compartment exchange model, which will be described in detail in Chapter 3. The calculations were based on a model voxel that includes an extracellular, a cytoplasmic and a vesicular compartment (indicated with sub-scripts  $e$ ,  $c$  and  $v$ , respectively). The longitudinal  $^1\text{H}_2\text{O}$  relaxation rate was calculated by solving the Bloch-McConnell equations including water exchange between the compartments. The model seems excellently suited to describe our experimental findings, where contrast agent was found distributed in a varying number of relatively small (in case of incubation with NT-liposomes) or large vesicles (in case of incubation with RGD-liposomes) located in the cellular cytoplasm. In Figure 3B the solid lines represent the result of calculations using this model, where contrast agent was accumulated in a varying number of either  $n_v = 0 - 200$  small, or  $n_v = 0 - 20$  large vesicles, representing the NT- and RGD-liposome incubations, respectively. The diameters of the small and large vesicles were taken to be 2 and 5  $\mu\text{m}$ , respectively, while a cell diameter of 30  $\mu\text{m}$  was assumed. Number and size of the vesicles are in agreement with experimental

observations. Further input parameters were: the volume fraction of the extracellular compartment ( $v_e = 0.5$ ), the volume fraction of individual vesicles ( $v_v = 0.148 \cdot 10^{-3}$  and  $v_v = 2.32 \cdot 10^{-3}$  for small and large vesicles, respectively), the total water fraction ( $f_w = 0.8$ ), the  $^1\text{H}_2\text{O}$  diffusional permeability coefficient of the membranes ( $P_d = 20 \mu\text{m/s}$  [23]), which was assumed equal for both cellular and vesicular membranes, and the  $^1\text{H}_2\text{O}$  relaxation rate constants for the different compartments ( $R_{1e} = 0.4 \text{ s}^{-1}$ ,  $R_{1c} = 0.5 \text{ s}^{-1}$ ,  $R_{1v} = 0.4 + r_1[\text{CA}]_v \text{ s}^{-1}$ ) in the absence of exchange.  $R_{1v}$  was different from the other compartments to simulate the presence of contrast agent in the vesicles using a relaxivity value  $r_1 = 4.7 \text{ mM}^{-1}\text{s}^{-1}$ , with  $[\text{CA}]_v = 0-9 \text{ mM}$  and  $[\text{CA}]_v = 0-76 \text{ mM}$  for small and large vesicles, respectively.

As can be seen in Figure 3B, model and experimental data are in good agreement. From the calculation the difference between contrast accumulations in an increasing number of small or large vesicles can be understood. The model-derived data corroborates the proposed hypothesis and indicates that, since the relaxation rate in the large vesicles is very high due to the presence of a high concentration of contrast agent, the water exchange across the vesicular membrane is not fast enough to distribute this high relaxivity over the entire voxel, and therefore a lower, *i.e.* quenched, relaxivity is observed. For the smaller vesicles, the surface-to-volume ratio is much larger and consequently water exchange across the vesicular membrane is more efficient leading to a reduced quenching effect. Hence, the quenching effect is negligible in this case. The origin of the quenching effect lies therefore in the inadequate exchange of magnetization across the vesicular membranes.

Interestingly the longitudinal relaxivity,  $r_1$ , after incubation with NT-liposomes ( $4.7 \pm 0.3 \text{ mM}^{-1}\text{s}^{-1}$ ), is twice as high as that of liposomes in suspension in HBS, pH 7.4. ( $2.3 \pm 0.1 \text{ mM}^{-1}\text{s}^{-1}$ ). An explanation for the increase in relaxivity might be that the structural integrity of the liposomes is compromised within the intracellular compartments. In intact liposomes, the  $T_1$ -shortening efficacy of the gadolinium containing lipids on the inside of the liposome is greatly diminished since the water diffusion over the liposomal membrane is very low [24, 25]. If the integrity of the liposomes is compromised, the gadolinium containing lipids, localized in the inner leaflet of the liposomal membrane, may be engaged in  $T_1$ -shortening of the extraliposomal water leading to an effective doubling of the relaxivity. Furthermore, the longitudinal relaxivity could be influenced by the presence of macromolecules [26].

Quenching of the longitudinal relaxivity, as was found in this study, has also been reported in other studies using non-targeted cell-internalized paramagnetic

contrast agents. A reduction in T<sub>1</sub>-shortening efficacy of Gd-HPDO3A has been reported by Terreno *et al.* [27]. The authors describe that internalization of this low molecular weight contrast agent in endosomes by pinocytosis severely lowered the longitudinal relaxivity. Terreno *et al.* observed quenching of longitudinal relaxivity in case of the uptake of Gd-HPDO3A in endosomes, whereas for contrast agents present in the cytoplasm quenching only occurred at very high concentrations. Brekke *et al.* [6, 28] labeled neural stem cells for cell tracking purposes, with a gadolinium based contrast agent, gadolinium rhodamine dextran (GRID). Both *in vivo* and *in vitro* analysis showed that the GRID-labeled cells induced signal attenuation on both T<sub>2</sub>- and T<sub>2</sub>\*-weighted images. In line with our observations, only a modest signal gain was obtained on T<sub>1</sub>-weighted images. Kobayashi *et al.* [29] have also observed reduced longitudinal relaxivity after internalization of avidin-dendrimer-(1B4M-Gd)<sub>254</sub> into tumor cells. Lewin *et al.* [30] have investigated the internalization of Gd-EOB-DTPA in rat cultured hepatocytes and two hepatoma cell lines, observing reduced longitudinal relaxivity efficacy of the internalized contrast agent. A study that showed quenching of the longitudinal relaxivity using a targeted contrast agent has been reported by Geniatti Crich *et al.* [31]. This study describes the targeting of the amino acid transporter system of hepatoma cells using the low molecular weight contrast agent Gd-DOTAMA-C<sub>6</sub>-Gln.

For both HUVECs incubated with either RGD- or NT-liposomes, the transverse relaxation rate increased linearly with concentration and no evidence for quenching of r<sub>2</sub> was observed across the entire range of uptake levels. The r<sub>2</sub> of HUVEC incubated with NT-liposomes was approximately equal to the r<sub>2</sub> of both RGD-liposomes and NT-liposomes in suspension. In contrast, the r<sub>2</sub> of RGD-liposomes internalized by HUVECs was twice as high. We infer that the accumulations of contrast agent within the large intracellular vesicles lead to an increased susceptibility induced T<sub>2</sub> relaxation effect on nearby diffusing water protons.

This study showed that the effective relaxation enhancement as brought about by an internalized paramagnetic contrast agent critically depends on its intracellular localization and/or concentration. The longitudinal relaxivity of internalized α<sub>v</sub>β<sub>3</sub>-targeted liposomes was much lower than that of NT-liposomes. Although it remains to be demonstrated, this quenching effect may also occur *in vivo*, which would hamper the detection of targeted contrast agent with T<sub>1</sub>-weighted MRI. It might be beneficial to design targeted contrast agents that are either not taken up in or that are released from endosomes. Several techniques have been suggested to release macromolecules from endosomes or to avoid endosomation. Photochemical internalization, as described by

Hogset *et al.* [32] and Fretz *et al.* [33], releases macromolecules from endocytic vesicles into the cytoplasm by incorporation of a photosensitizer in the endosomal membranes that can be activated by light and induces leakage of endosomal membranes. This technique can possibly also be used to deliver endosomal paramagnetic contrast agents into the cytoplasm. Furthermore, cell penetrating peptides have been used to bypass endosomation and enable vehicle delivery into the cytoplasm [34-37].

In conclusion, this study showed that the mechanism of cellular uptake influences both the longitudinal and transverse relaxivity of paramagnetic liposomes. It is therefore of key importance to understand the mechanisms of uptake of targeted contrast agents and the effect it has on the relaxivity properties of contrast agents in order to improve the efficacy of molecular and cellular MRI.

**Acknowledgements**

Dr. C.S. Springer Jr. is acknowledged for his insightful discussions regarding the modeling of the experimental data.

## Literature

1. Briley-Saebo, K.C., W.J. Mulder, V. Mani, *et al.*, *J Magn Reson Imaging*, 2007. **26**(3): p. 460-479.
2. Strijkers, G.J., W.J. Mulder, G.A. van Tilborg, *et al.*, *Anticancer Agents Med Chem*, 2007. **7**(3): p. 291-305.
3. Cyrus, T., G.M. Lanza, S.A. Wickline, *J Cardiovasc Magn Reson*, 2007. **9**(6): p. 827-843.
4. Mulder, W.J., G.J. Strijkers, E. Vucic, *et al.*, *Top Magn Reson Imaging*, 2007. **18**(5): p. 409-417.
5. Himmelreich, U., S. Aime, T. Hieronymus, *et al.*, *Neuroimage*, 2006. **32**(3): p. 1142-1149.
6. Brekke, C., S.C. Williams, J. Price, *et al.*, *Neuroimage*, 2007. **37**(3): p. 769-782.
7. Biancone, L., S.G. Crich, V. Cantaluppi, *et al.*, *NMR Biomed*, 2007. **20**(1): p. 40-48.
8. Modo, M., K. Mellodew, D. Cash, *et al.*, *Neuroimage*, 2004. **21**(1): p. 311-317.
9. Vuu, K., J. Xie, M.A. McDonald, *et al.*, *Bioconjug Chem*, 2005. **16**(4): p. 995-999.
10. Nunn, A.D., K.E. Linder, M.F. Tweedle, *Q J Nucl Med*, 1997. **41**(2): p. 155-162.
11. Caravan, P., *Chem Soc Rev*, 2006. **35**(6): p. 512-523.
12. Mulder, W.J., G.J. Strijkers, G.A. van Tilborg, *et al.*, *NMR Biomed*, 2006. **19**(1): p. 142-164.
13. Jocher, C.J., M. Botta, S. Avedano, *et al.*, *Inorg Chem*, 2007. **46**(12): p. 4796-4798.
14. Port, M., I. Raynal, L. Vander Elst, *et al.*, *Contrast Media Mol Imaging*, 2006. **1**(3): p. 121-127.
15. Aime, S., L. Calabi, C. Cavallotti, *et al.*, *Inorg Chem*, 2004. **43**(24): p. 7588-7590.
16. Mulder, W.J., A.W. Griffioen, G.J. Strijkers, *et al.*, *Nanomed*, 2007. **2**(3): p. 307-324.
17. Caswell, P.T., J.C. Norman, *Traffic*, 2006. **7**(1): p. 14-21.
18. Brooks, P.C., R.A. Clark, D.A. Cheresch, *Science*, 1994. **264**(5158): p. 569-571.
19. Mulder, W.J., G.J. Strijkers, A.W. Griffioen, *et al.*, *Bioconjug Chem*, 2004. **15**(4): p. 799-806.
20. Rouser, G., S. Fkeischer, A. Yamamoto, *Lipids*, 1970. **5**(5): p. 494-496.
21. Scudiero, D.A., R.H. Shoemaker, K.D. Paull, *et al.*, *Cancer Res*, 1988. **48**(17): p. 4827-4833.
22. Koning, G.A., R.M. Schiffelers, M.H. Wauben, *et al.*, *Arthritis Rheum*, 2006. **54**(4): p. 1198-1208.
23. Garrick, R.A., U.S. Ryan, F.P. Chinard, *Am J Physiol*, 1988. **255**(3 Pt 1): p. C311-314.
24. Terreno, E., A. Sanino, C. Carrera, *et al.*, *Journal of Inorganic Biochemistry*, 2008. **102**(5-6): p. 1112.
25. Strijkers, G.J., W.J.M. Mulder, R.B. van Heeswijk, *et al.*, *Magnetic Resonance Materials in Physics, Biology and Medicine*, 2005. **18**(4): p. 186-192.
26. Stanisz, G.J., Henkelman, R.M., *Magnetic Resonance in Medicine*, 2000. **44**(5): p. 665-667.
27. Terreno, E., S. Geninatti Crich, S. Belfiore, *et al.*, *Magn Reson Med*, 2006. **55**(3): p. 491-497.
28. Brekke, C., S.C. Morgan, A.S. Lowe, *et al.*, *NMR Biomed*, 2007. **20**(2): p. 77-89.
29. Kobayashi, H., S. Kawamoto, T. Saga, *et al.*, *Bioconjug Chem*, 2001. **12**(4): p. 587-593.
30. Lewin, M., O. Clement, P. Belguise-Valladier, *et al.*, *Invest Radiol*, 2001. **36**(1): p. 9-14.
31. Geninatti Crich, S., C. Cabella, A. Barge, *et al.*, *J Med Chem*, 2006. **49**(16): p. 4926-4936.
32. Hogset, A., L. Prasmickaite, P.K. Selbo, *et al.*, *Adv Drug Deliv Rev*, 2004. **56**(1): p. 95-115.
33. Fretz, M.M., A. Hogset, G.A. Koning, *et al.*, *Pharm Res*, 2007. **24**(11): p. 2040-2047.
34. Torchilin, V.P., R. Rammohan, V. Weissig, *et al.*, *Proc Natl Acad Sci U S A*, 2001. **98**(15): p. 8786-8791.
35. Lewin, M., N. Carlesso, C.H. Tung, *et al.*, *Nat Biotechnol*, 2000. **18**(4): p. 410-414.
36. Josephson, L., C.H. Tung, A. Moore, *et al.*, *Bioconjug Chem*, 1999. **10**(2): p. 186-191.
37. Medarova, Z., W. Pham, C. Farrar, *et al.*, *Nat Med*, 2007. **13**(3): p. 372-377.

## Chapter **3**

### **A three-compartment $T_1$ -relaxation model for intracellular paramagnetic contrast agents**

**Based on:**

*A three-compartment  $T_1$ -relaxation model for intracellular paramagnetic contrast agents*

G.J. Strijkers, S. Hak, M.B. Kok, C.S. Springer Jr, K. Nicolay  
Magnetic Resonance in Medicine, 2009, 61(5), p. 1049-1058



**Abstract**

The goal of this work was to elaborate a model describing the effective longitudinal relaxation rate constant  $R_1$  for  $^1\text{H}_2\text{O}$  in three cellular compartments experiencing possible equilibrium water exchange, and to apply this model to explain the effective  $R_1$  dependence on the overall concentration of cell-internalized  $\text{Gd}^{3+}$ -based contrast agent (CA). The model voxel comprises three compartments representing extracellular, cytoplasmic and vesicular (*e.g.* endosomal, lysosomal) subcellular spaces. Relaxation parameters were simulated using a modified Bloch-McConnell equation including magnetization exchange between the three compartments. With the model several possible scenarios for internalized CA distribution were evaluated. Relaxation parameters were calculated for contrast agent restricted to the cytoplasmic or vesicular compartments. The size or the number of CA-loaded vesicles was varied. The simulated data were then separately fitted with empirical mono- and bi-exponential inversion recovery expressions. The voxel CA-concentration dependencies of  $R_1$  can be used to qualitatively and quantitatively understand a number of different experimental observations reported in the literature. Most importantly the simulations reproduced the relaxivity “quenching” for cell-internalized contrast agent that has been observed.

## Introduction

A common application of traditional  $Gd^{3+}$ -based contrast agents (CA) is dynamic contrast-enhanced MRI (DCE-MRI). This involves intravenous injection of a CA bolus into the blood compartment after which the agent may extravasate into the extracellular compartment in the tissue region of interest to report on *e.g.* tissue perfusion or blood-tissue-barrier leakage. Transient changes in the  $T_1$  and  $T_2$  relaxation time constants of the tissue water proton MR signals are monitored [1]. Although the agent may extravasate, it generally is not able to cross the cellular membranes into the intracellular spaces and therefore distributes in the extracellular compartment only, before being washed out again for subsequent renal clearance.

In recent years numerous novel targeted  $Gd(III)$ -based CAs have been developed. These agents are designed to report on cellular processes, *e.g.* by specific binding of the agent to disease specific receptors expressed on the cellular membranes of pathological cells [2]. Following binding, however, in many cases the CA will be shuttled into the intracellular space by receptor mediated endocytosis or phagocytosis [3]. In the field of cellular imaging the aim is to deliberately load (for example, stem-) cells with CA *in vitro* to enable subsequent *in vivo* visualization of cell implantation, migration and homing [4]. These new applications thus have in common that CA will distribute at least partly within the cytoplasm or a subcellular compartment – in distinct contrast to the CA fate during DCE-MRI studies.

Since generally MRI voxel dimensions are much larger than cellular dimensions, the observed CA-induced  $T_1$  and  $T_2$  relaxation changes will be a voxel-averaged contribution from those of intravascular, extracellular, cytoplasmic and subcellular compartmental  $^1H_2O$  signals. However, because tissue water molecules are not static but diffusing within and exchanging between compartments with lifetimes comparable to  $T_1$ ,  $T_2$  and the vital timing parameters of the MRI experiment, the observed  $T_1$  and  $T_2$  values will not be simple weighted averages of contributions from the different compartments but averages that include the effects of equilibrium inter-compartmental water exchange.

The effects of intercompartmental exchange on the tissue  $^1H_2O$   $T_1$  value have been extensively considered for the DCE-MRI situation [5-7]. It is well recognized from these studies that intravascular and/or interstitial CA compartmentalization and water exchange kinetics between the intravascular, extracellular and cytoplasmic compartments can lead to non-linear dependence of  $R_1$  ( $\equiv 1/T_1$ ) on CA concentration. This is caused by the fact that as the amount

of compartmental CA changes the so-called relaxographic “shutter-speed” for transmembrane water exchange processes also changes [7]. This leads to a temporal variation of the NMR system’s exchange condition. Therefore correct quantitative interpretation of DCE-MRI data must account for these shutter-speed effects.

In this paper, we have concentrated on  $R_1$  changes caused by cell-internalized CA that are mediated by water exchange kinetics and shutter-speed effects. We have specifically addressed CA accumulation in cytoplasmic or in subcellular (vesicular) compartments. This work was motivated by recent reports on *in vitro* and *in vivo* multi-exponential  $T_1$ -relaxation and non-linear concentration-dependence of  $R_1$  for CA-loaded cells. These were attributed to relaxivity “quenching” due to limited water exchange consequent to CA entrapment in cytoplasmic or subcellular compartments (Chapter 2 and refs. [8-16]). Before the well-known *Xenopus* development study that introduced “smart” CAs [17], the investigators were (poorly) advised against going to the trouble of injecting the latter into an embryonic cell. It was mistakenly assumed that equilibrium transcytolemmal water exchange is sufficiently rapid as to render this compartmentalization irrelevant. Possibly the only way to completely elaborate potential consequences of subcellular CA compartmentalization in detail is with model simulations.

## Methods

### Model

Figure 1 shows a cartoon of the model voxel enclosing a cell with three kinds of compartments into which water and CA may be distributed: extracellular, cytoplasmic, and/or vesicular (e.g. endosomal, lysosomal, nuclear, etc.), indicated with subscripts lower-case e, c and v, respectively. The effective  $R_1$  of the whole voxel  $^1\text{H}_2\text{O}$  was determined by the different compartmental  $R_1$  values and the equilibrium exchange of water molecules between the compartments. The extracellular-cytoplasmic and cytoplasmic-vesicular exchange processes were considered important. The volume fraction inaccessible to water and mobile aqueous solutes was ascribed to the cytoplasmic compartment, and indicated as "macro" in Figure 1. The intracellular nuclear compartment was not explicitly considered in the simulations.

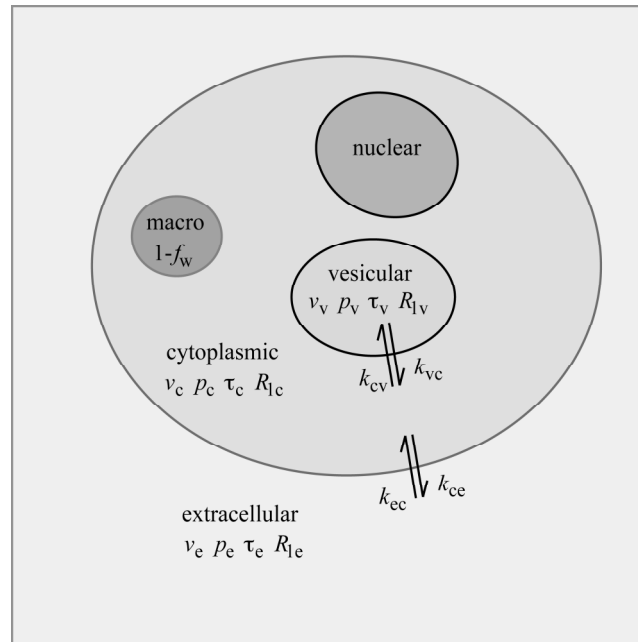


**Figure 1, Model voxel containing an extracellular compartment and a cell with cytoplasmic and vesicular compartments. Equilibrium exchange of water between extracellular and cytoplasmic, as well as between cytoplasmic and vesicular compartments is considered. The "macro" label designates the tissue volume fraction inaccessible to mobile aqueous solutes.**

Transport processes within the Figure 1 model voxel can be mathematically described using the framework of a three-site exchange model (3SX) of nuclear magnetization [7, 18-21]. This was used to account for the equilibrium water exchange processes between the extracellular, the cytoplasmic and the vesicular compartments. Exchange from the extracellular to the vesicular compartment was considered to occur *via* the cytoplasmic compartment. Thus we have a

linear 3SX model with no direct exchange between the extracellular and vesicular compartments. Since there is a model voxel for each cell, there are many model voxels in an image voxel. We will see that these exchange considerations can nicely account for relaxivity “quenching” phenomena reported by a number of investigators.

### Theory

Model input parameters are: the water mole fractions of the different compartments,  $p_e$ ,  $p_c$  and  $p_v$ ; the volume fractions,  $v_e$ ,  $v_c$  and  $v_v$ ; the total accessible volume fraction,  $f_w$ ; the  $^1\text{H}_2\text{O}$  longitudinal relaxation rate constants in the absence of exchange,  $R_{1e}$ ,  $R_{1c}$ ,  $R_{1v}$ ; the relaxivity of the contrast agent  $r_1$ ; the mean compartmental water molecule lifetimes,  $\tau_e$ ,  $\tau_c$ ,  $\tau_v$ ; the rate constants for water exchange between the compartments,  $k_{ce}$ ,  $k_{ec}$ ,  $k_{cv}$ ,  $k_{vc}$ ; the vesicle radius  $r_v$ ; the number of vesicles  $n_v$ ; the cell radius  $r_c$ ; and finally the  $\text{H}_2\text{O}$  membrane diffusional permeability coefficient,  $P_d$ .

Volume fractions, water fractions and total water fraction are interrelated according to

$$\begin{aligned} v_e &= p_e f_w \\ v_c &= p_c f_w + (1 - f_w) \\ v_v &= p_v f_w \end{aligned} \quad [1]$$

and

$$\begin{aligned} p_e + p_c + p_v &= 1 \\ v_e + v_c + v_v &= 1. \end{aligned} \quad [2]$$

Here  $(1 - f_w)$  represents the volume fraction of non-aqueous constituents. Exchange rate constants and water lifetimes are related through the sets of equations

$$\begin{aligned} k_{ce} &= \tau_c^{-1} - \frac{p_v}{p_c} \tau_v^{-1} \\ k_{ec} &= \tau_e^{-1} \end{aligned} \quad [3]$$

and

$$\begin{aligned} k_{cv} &= \tau_c^{-1} - \frac{p_e}{p_c} \tau_e^{-1} \\ k_{vc} &= \tau_v^{-1} \end{aligned} \quad [4]$$

for exchange between extracellular and cytoplasmic (transcytolemmal), and between cytoplasmic and vesicular (transvesiculemmal) compartments, respectively. The mass balance relates the water fractions and the life times via

$$\frac{P_c}{\tau_c} = \frac{P_e}{\tau_e} + \frac{P_v}{\tau_v}. \quad [5]$$

The vector of the three compartmental  $^1\text{H}_2\text{O}$  longitudinal magnetizations

$$\mathbf{M} = (M_e, M_c, M_v) \quad [6]$$

is subject to relaxation and exchange *via* the Bloch equation modified for three-site exchange in matrix notation [5, 7, 18, 20, 22]

$$\frac{d\mathbf{M}}{dt} = \mathbf{X} \cdot \mathbf{M} + \mathbf{C}, \quad [7]$$

with

$$\mathbf{X} = \begin{pmatrix} -(R_{1e} + k_{ec}) & k_{ce} & 0 \\ k_{ec} & -(R_{1c} + k_{ce} + k_{cv}) & k_{vc} \\ 0 & k_{cv} & -(R_{1v} + k_{vc}) \end{pmatrix} \quad [8]$$

the relaxation-and-exchange matrix and

$$\mathbf{C} = (R_{1e}M_{0e}, R_{1c}M_{0c}, R_{1v}M_{0v}). \quad [9]$$

Equation 7 is the Bloch-McConnell differential rate law [23], for which a solution can be written for the case of an inversion recovery (IR) experiment

$$\mathbf{M}(\text{TI}) = (\mathbf{I} - 2 e^{\text{TI} \mathbf{X}}) \cdot \mathbf{M}_0, \quad [10]$$

with

$$\mathbf{M}_0 = -\mathbf{X}^{-1} \cdot \mathbf{C} \quad [11]$$

the equilibrium (Boltzmann) magnetization and TI the inversion time. The observed signal intensity  $S$  is proportional to  $M(\text{TI})$ .

The effect of CA cellular internalization was included by expressing the appropriate x compartmental (cytoplasmic or vesicular) relaxation rate constant  $R_{1x}$  (in the absence of exchange) according to

$$R_{1x} = R_{1x0} + r_{1x} [CA_x] \quad [12]$$

and

$$[CA_T] = v_x [CA_x], \quad [13]$$

in which  $R_{1x0}$  is the rate constant without CA,  $r_{1x}$  the CA relaxivity (unit,  $\text{mM}^{-1}\text{s}^{-1}$ ),  $[CA_x]$  the CA concentration (unit, mM) in compartment x and  $[CA_T]$  the voxel-based concentration (would be tissue concentration, *in vivo*).

For a single spherical vesicle with radius  $r_v$ , volume  $V_v = \frac{4}{3}\pi r_v^3$  and membrane surface area  $A_v = 4\pi r_v^2$ , the unidirectional water efflux rate constant (reciprocal average vesicular water lifetime) can be expressed as [24]:

$$\tau_v^{-1} = P_{dv} \frac{A_v}{V_v} = \frac{3P_{dv}}{r_v}. \quad [14]$$

The extracellular compartment has a total volume  $V_E$  and membrane surface area  $A_E$ , and since the extracellular compartment can be considered a terminal compartment the reciprocal average extracellular water lifetime is

$$\tau_e^{-1} = P_{dc} \frac{A_E}{V_E}. \quad [15]$$

Since the extracellular compartment is not spherical, Eq. 15 cannot be simplified directly in a similar fashion as Eq. 14. However, the single cell in the model voxel can be assumed spherical with radius  $r_C$ , volume  $V_C = \frac{4}{3}\pi r_C^3$  and membrane surface area  $A_C = 4\pi r_C^2$ . Note that here an upper-case C subscript indicates a property of an individual cell (including vesicles), while a lower-case c indicates the cytoplasmic space. Since the extracellular compartment and the cell share the same membrane surface area,  $A_E = A_C$ .

Furthermore, using  $V_E = \{v_e / (v_c + v_v)\} V_C$ , Eq. 15 can be conveniently reduced to

$$\tau_e^{-1} = P_{dc} \frac{A_E}{V_E} = \frac{3P_{dc}}{r_C} \frac{v_c + v_v}{v_e}. \quad [16]$$

We have also assumed that the diffusional permeability coefficients of the vesicle ( $P_{dv}$ ) and cell ( $P_{dc}$ ) membranes are equal, and labeled these  $P_d$ . The vesicle membrane is likely derived from the cytolemma, though the  $P_d$  values can also have (active) contributions from cellular metabolic processes, and these could differ for  $P_{dv}$  and  $P_{dc}$ . Consequently, the average water lifetimes in all three compartments are expressed as functions of  $P_d$ . Variation of the number of cytoplasmic vesicles can now be included by

$$v_v = n_v v_V, \quad [17]$$

with  $n_v$  the number of vesicles and  $v_V$  the voxel volume fraction occupied by a single vesicle.

#### *Model simulations*

All calculations were performed in Mathematica 6 (Wolfram Research, Inc.). Inversion recovery curves were simulated using inversion times (TI) ranging from 0 to 5000 ms in steps of 5 ms, and Eq. 10. Next, the resulting simulated time points were separately fitted with empirical mono-

$$S_1 = 1 - 2 e^{-TI R_1} \quad [18]$$

and bi-exponential

$$S_2 = f_{2A} (1 - 2 e^{-TI R_{1A}}) + f_{2B} (1 - 2 e^{-TI R_{1B}}) \quad [19]$$

IR expressions (single- and double-valued relaxation rate constants, respectively). Here  $R_1$  as well as  $R_{1A}$  and  $R_{1B}$  represent *empirical* relaxation rate constants for the total model voxel signal. These contrast with the molecular rate constants for the individual compartments used in Eq. 8, 9 and 12. Likewise  $f_{2A}$  and  $f_{2B}$  are the *apparent* fractions of fast- (large  $R_{1A}$ ) and slow-relaxing (small  $R_{1B}$ ) populations contributing to the measured recovery. Of course, Eqs. 7 to 9 provide for potential triple-exponential relaxation. However, it is impractical to expect to resolve this experimentally.



For model calculations 1, 2 and 3, we have fixed  $v_e = 0.5$ ,  $r_C = 10 \mu\text{m}$  [25],  $f_w = 0.8$ , and the  $\text{H}_2\text{O}$  diffusional membrane permeability coefficient  $P_d = 10 \mu\text{m/s}$  [25]. The relaxation rate constants of the three compartments with no CA and in the absence of exchange were assumed to be  $R_{le0} = 0.4 \text{ s}^{-1}$ ,  $R_{lc0} = 0.5 \text{ s}^{-1}$  and  $R_{lv0} = 0.4 \text{ s}^{-1}$ . The CA relaxivity, assumed equal for CA in the cytoplasm or vesicles, was  $r_1 = 4.2 \text{ mM}^{-1}\text{s}^{-1}$ , a typical value for low molecular weight CAs such as Gd(III)-DTPA or Gd(III)-HPDO3A at high magnetic field and the pertinent temperature. Thus, all parameter values chosen are quite reasonable and precedented. In this sense, there are no adjustable parameters used here. Table 1 lists the numerical parameter values employed in the calculations described below. Calculated property values are reported as function of voxel CA concentration, up to 1.8 mM.

#### Calculation 1 : cytoplasmic or vesicular contrast agent

The first calculation was performed for CA distributed either in the cytoplasmic or in a single large vesicular compartment. As above,  $r_C = 10 \mu\text{m}$ : the radius of the single vesicular compartment was taken as  $r_V = 3.5 \mu\text{m}$  (Chapter 2 and refs. [8, 16]), resulting in  $v_c = 0.479$  and  $v_v = 0.021$ . The cytoplasmic CA concentration was varied between 0 and 3.76 mM. Then, the CA was confined to the vesicular compartment to illustrate the increased relaxivity quenching encountered when a given voxel CA amount is confined to a smaller space. The CA concentration in the vesicular compartment was varied between 0 and 85.7 mM.

#### Calculation 2 : vesicle size influence

Here the CA was confined to only the vesicular compartment. The effects on the relaxation rate constant of differently sized CA-containing vesicles was calculated for either  $n_v = 5$  large or  $n_v = 220$  small vesicles. Large and small single vesicles had radii of  $r_V = 3.5 \mu\text{m}$  and  $r_V = 1.0 \mu\text{m}$ , respectively (Chapter 2 and refs. [8, 16]), resulting in  $v_c = 0.393$  and  $v_v = 0.107$  in each case.

#### Calculation 3 : vesicle number variation

The last calculation was performed to illustrate the effects on the relaxation rate constant of an increasing number of identical CA-containing vesicles (a monodisperse distribution). The vesicular CA concentration was fixed at 16.8 mM. The vesicle number ( $n_v$ ) was varied between 0 and 5 for large vesicles and between 0 and 220 for small vesicles. Non-integer values for vesicle numbers were allowed because statistical averaging of a large model voxel

number (in an image voxel) was assumed. Individual large and small vesicles had radii of  $r_V = 3.5 \mu\text{m}$  and  $r_V = 1.0 \mu\text{m}$ , respectively.

Calculation 4 : comparison with literature data

Finally, we have performed calculations with input parameters based on two different literature reports [13, 16], where relaxivity quenching was observed as a consequence of endosomal entrapment of Gd- and FeO-based CAs, respectively. The parameter values for these calculations are detailed in the last two columns of Table 1. In short, the CAs were distributed in vesicular compartments. CA concentration in the vesicles was varied up to a voxel concentration of 0.25 mM. We assumed a vesicular radius of 1  $\mu\text{m}$ . Appropriate relaxivities for the two different CAs were used. Only the vesicle number ( $n_V$ ) was adjusted for comparison with the experimental data. These were not formal multiparametric fittings.



## Results

### Calculation 1

Figure 2 displays mono- (A, B) and bi-exponential (C, D) fittings (Eqs. 18 and 19) of the simulated inversion recovery curves (open circles) for cytoplasmic CA distribution with voxel CA concentrations of 0.1 mM (A, C) and 1.6 mM (B, D). The IR curves for the low CA concentration case are fitted very well with Eq. 18 (mono-exponential), while fitting with Eq. 19 (bi-exponential) results in only a small improvement that cannot be appreciated visually. On the other hand, the simulated IR data for the high CA concentration is clearly better described as a bi-exponential inversion recovery (D) than a mono-exponential (B). In Figure 3, 4 and 5, parameters from both mono- and bi-exponential fittings of simulated IR data are presented.

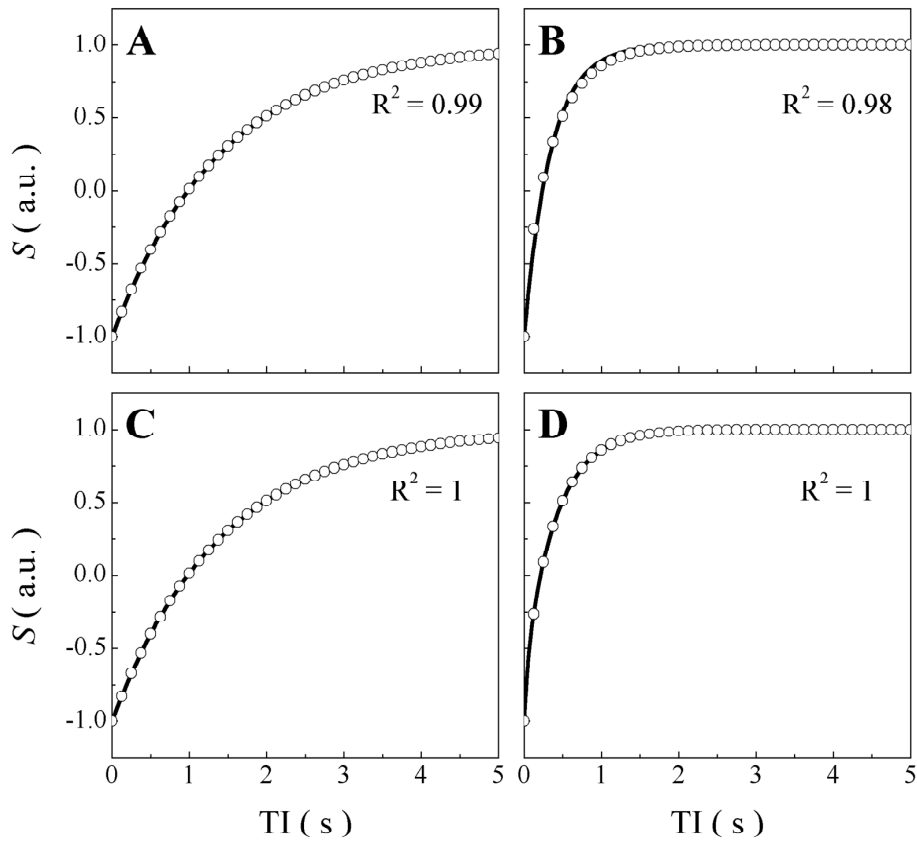


**Figure 2** Simulated inversion recovery curves for cytoplasmic CA distribution with voxel CA concentrations of (A, C) 0.1 mM and (B, D) 1.6 mM. Open circles are simulated data points, while solid lines are the fittings with (A, B) Eq. 18 (mono-exponential) and (C, D) Eq. 19 (bi-exponential). To avoid cluttering only 40 data points along the inversion recovery curve are displayed. The  $R^2$  values for the fittings are indicated in the figure.

In Figure 3 the fitted  $^1\text{H}_2\text{O}$  relaxation parameters are plotted as function of voxel CA concentration for CA distributed in either the cytoplasm or a single large vesicular compartment. We will focus first on CA confined to the cytoplasm (left panels in Figure 3).

In Figure 3A empirical  $R_1$  values from fitting simulated data with the mono-exponential inversion recovery expression (Eq. 18) are displayed.  $R_1$  increases with increasing voxel CA concentration. However, the dependence is distinctly non-linear. The origin of the progressive decrease in effective relaxivity (the slope of this curve) can be seen in Figure 3G, which plots the simulated relaxographic shutter-speeds  $|R_{1c} - R_{1v}|$  and  $|R_{1c} - R_{1e}|$  (which are equal), and invariant exchange rate constant sums  $k_{cv} + k_{vc}$  and  $k_{ce} + k_{ec}$  for transvesiclemmal and transcytolemmal exchange, respectively. Above a CA concentration of about 0.9 mM the shutter-speed  $|R_{1c} - R_{1e}|$  becomes higher than the transcytolemmal exchange rate constants sum  $k_{ce} + k_{ec}$ , which means that this system has clearly departed from the fast-exchange limit (FXL) and probably even the fast-exchange-regime (FXR) entering the slow-exchange-regime (SXR) [25]. Above approximately 1.0 mM, transvesiclemmal exchange also appears to slow as  $|R_{1c} - R_{1v}|$  becomes larger than  $k_{cv} + k_{vc}$ . For the system of any particular exchange process, the SXR condition is characterized by incomplete averaging of the compartmental relaxation rate constants and consequently bi-exponential relaxation can in principle be observed (Figure 2B and D). Though the FXR and SXR conditions are strictly defined only for two-site-exchange, the characteristic mismatch seen in Figure 2B is the definitive criterion for the SXR [25]. The two asterisks in Figure 3A correspond to the low (A, C) and high (B, D) voxel CA concentrations of Figure 2. Even though the CA is strictly located in the cytoplasm here, the water-filled intracellular vesicle is still present and the equilibrium transvesiclemmal water exchange is therefore still influential.

When the respective relaxographic shutter-speed is sufficiently lower than the transcytolemmal or transvesiclemmal exchange rate constant sum, the system approaches the FXL, which is characterized by complete weighted averaging of the compartmental relaxation rate constants and mono-exponential relaxation (Figure 2A and C). In Figure 3, 4 and 5 calculated parameters are plotted with dashed traces when in the FXL/FXR condition and with solid lines when at least one exchange process has departed the FXL/FXR for the SXR condition.

Figure 3C and E show the results from bi-exponential fittings of the simulated inversion recovery relaxation curves. The relaxation rate constant  $R_{1A}$  strongly

increases with CA concentration, while  $R_{1B}$  saturates at higher concentrations. The apparent population fraction  $f_{1A}$  increases (from zero) with increasing concentration, while  $f_{1B}$  decreases (from unity). In the right hand panels (B, D, F) of Figure 3, relaxation parameter resulting from fittings of simulated inversion recovery curves are presented for the same amounts of CA as in the left hand panels, but all sequestered in the single, large subcellular vesicular compartment. In Figure 3B it is immediately apparent that the relaxation rate constant levels off at a much smaller value and at a much smaller CA concentration value than in Figure 3A. The voxel CA relaxivity, *i.e.* the slope of  $R_1$  versus voxel CA concentration, becomes effectively zero above about 0.25 mM. This effect has been observed experimentally and was termed relaxivity "quenching" (Chapter 2 and refs. [8, 14, 15]). The origin of this effect lies in the fact that all CA molecules are now restricted to a small subcellular compartment, with the resulting higher concentrations. Consequently, the transvesiculemmal relaxographic shutter-speed  $|R_{1c} - R_{1v}|$  increases very rapidly with increasing voxel CA concentration (Figure 3H). The equilibrium transvesiculemmal water exchange system therefore already departs the FXL at concentrations above 0.25 mM and the difference between the shutter-speed and transvesiculemmal exchange rate constant sum is much higher than for CA distributed uniformly in the cytoplasm (note the differences in ordinate ranges between Figure 3C and 3D and between Figure 3G and 3H). In Figure 3D and 3F the corresponding bi-exponential relaxation rate constants and apparent population fractions for the vesicular CA case are presented. Although  $R_{1A}$  becomes much larger (in Figure 3D) than in Figure 3C and enjoys a much larger relaxivity, it contributes little to the measured relaxation rate constant as the apparent population fraction  $f_{1A}$  remains small (Figure 3F).

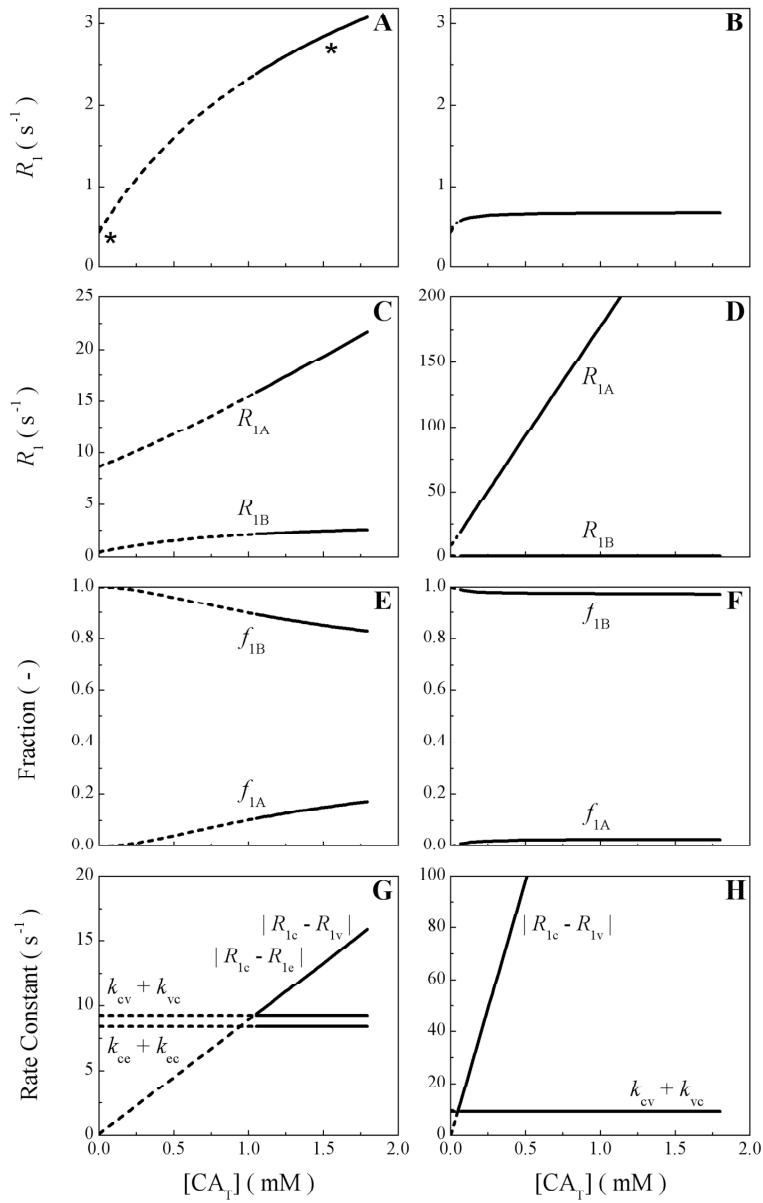


**Figure 3, Relaxation parameters as function of voxel CA concentration for CA distributed in the cytoplasmic (A, C, E, G) or one large vesicular (B, D, F, H) compartment. (A, B) Relaxation rate constant  $R_1$ . (C, D) Fast (large  $R_{1A}$ ) and slow (small  $R_{1B}$ ) relaxation rate constant contributions. (E, F) Apparent population fractions of fast ( $f_{1A}$ ) and slow ( $f_{1B}$ ) contributions. (G, H) Relaxographic shutter-speeds  $|R_{1c} - R_{1v}|$  and  $|R_{1c} - R_{1e}|$ , and exchange rate constant sums  $k_{cv} + k_{vc}$  and  $k_{ce} + k_{ec}$ . Lines are dashed at CA concentrations for which the three compartments can be considered in the FXL/FXR. Model parameter values are given in Table 1.**

### Calculation 2

In actual *in vivo* and *in vitro* situations, the CA is likely to distribute in more than a single subcellular vesicular compartment (Chapter 2 and refs. [3, 8, 16]). In Figure 4 the calculated relaxation parameters are displayed for CA sequestered uniformly in  $n_v = 5$  large (left hand panels) or  $n_v = 220$  small (right hand panels) vesicles. The total endosomal volume fraction was fixed at  $v_v = 0.11$  for each case.

In the Figure 4 left hand panels, similar relaxation parameter behavior is observed as for the case of a single large vesicular compartment ( $n_v = 1$ ) presented in the Figure 3 right hand panels. The effect of distributing the same amount of CA throughout five large vesicles is that the transvesiclemmal exchange kinetics increases slightly because of the decreased  $v_c$  value: that is,  $\tau_c$  is decreased and  $k_{cv}$  is increased (as is  $k_{ce}$ ) (Figure 4G). This was included in the model *via* Eqs. 14 to 17. As a consequence, FXL departure sets in at a somewhat larger CA concentration (Figure 4A) than in Figure 3B, resulting in a slightly larger effective  $R_1$ .

Increasing the number of vesicles from 5 large to 220 small ones increases the transvesiclemmal exchange kinetics substantially, as shown by the significantly larger  $k_{cv} + k_{vc}$  value in Figure 4H. Consequently, the FXL is departed at a much larger concentration (Figure 4B) than for the large vesicles (Figure 4A), resulting in a larger  $R_1$  and quenching only at larger CA concentrations. Although the larger relaxation rate constant  $R_{1A}$  is greater for the five vesicles of Figure 4C than for the 220 vesicles of Figure 4D, the resulting effective single-valued relaxation rate constant  $R_1$  is nevertheless greater for the 220 smaller vesicles (Figure 4B), because  $R_{1A}$  contributes with a much higher apparent population fraction  $f_{1A}$  (Figure 4F) to the observed total relaxation rate constant.



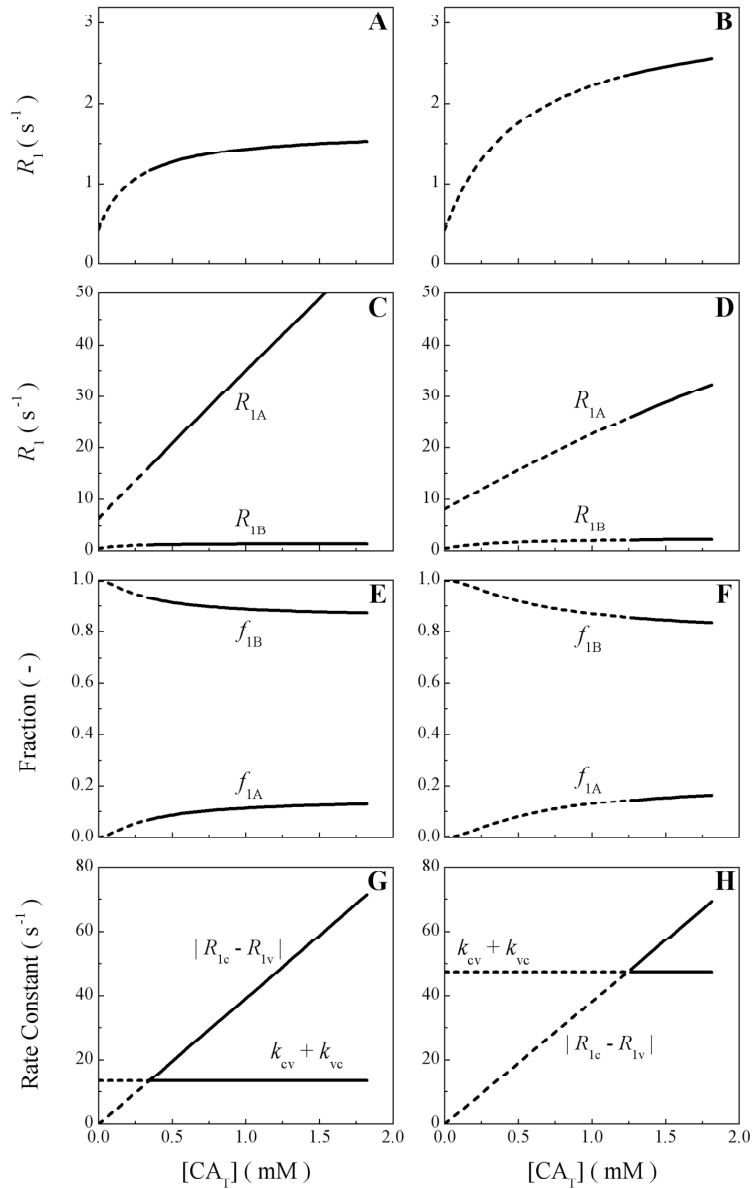


**Figure 4, Relaxation parameters as function of voxel CA concentration for CA distributed in 5 large (A, C, E, G) or 220 small (B, D, F, H) vesicles. (A, B) Relaxation rate constant  $R_1$ . (C, D) Fast (large  $R_{1A}$ ) and slow (small  $R_{1B}$ ) relaxation rate constant contributions. (E, F) Apparent population fractions of fast ( $f_{1A}$ ) and slow ( $f_{1B}$ ) contributions. (G, H) Relaxographic shutter-speed  $|R_{1c} - R_{1v}|$  and exchange rate constant sums  $k_{cv} + k_{vc}$ . Lines are dashed at CA concentrations for which the three compartments can be considered in the FXL/FXR. Model parameter values are given in Table 1.**

### Calculation 3

The results of calculation 3, the case in which the number of CA-loaded vesicles is varied, are presented in Figure 5. The figure panels are analogous to those of Figure 3 and 4. The vesicles were either large (left hand panels) or small (right hand panels). Since the vesicular CA concentration is constant, the relaxographic shutter-speed  $|R_{1c} - R_{1v}|$  for transvesicular exchange is also constant as shown in Figure 5G and H. The sum of transvesiculemmal exchange rate constants  $k_{cv} + k_{vc}$ , however, increases with increasing number of vesicles. The reason for this is that although  $k_{vc}$  is independent of the number of vesicles (Eq. 13),  $k_{cv}$  increases due to a decrease in the cytoplasmic volume fraction  $v_c$ .

Nevertheless, for the whole voxel CA concentration range considered here, the system is in the SXR condition since  $|R_{1c} - R_{1v}|$  is always significantly greater than  $k_{cv} + k_{vc}$ . This is reflected in the empirical  $R_1$  values in Figure 5A and B, which increase almost linearly with reduced slope.  $R_1$  does not saturate as was observed in Figure 3 and 4, which might present an opportunity to experimentally distinguish an increase in the number of CA-loaded vesicles from a constant number of vesicles with increasing CA concentration. The effective relaxivity for CA sequestered in the small vesicles is less quenched (Figure 5B) because of the larger transvesiculemmal exchange rate constants consequent to the larger vesicular surface-to-volume ratio (Figure 5H). This resulted in a greater contribution of the fast relaxation rate constant  $R_{1A}$  to the total relaxation rate constant  $R_1$  (compare Figure 5E with Figure 5F). In contrast to calculations 1 and 2,  $R_{1A}$  decreases with increasing CA concentration. This is caused by the fact that with increasing CA concentration (and decreasing  $v_c$ ) the transvesiculemmal exchange actually speeds up; the system goes back toward the FXR as  $k_{cv} + k_{vc}$  approaches  $|R_{1c} - R_{1v}|$  (Figure 5H). This is in distinct contrast to calculations 1 and 2 where this system leaves the FXR and approaches the SXR with increasing CA concentration.

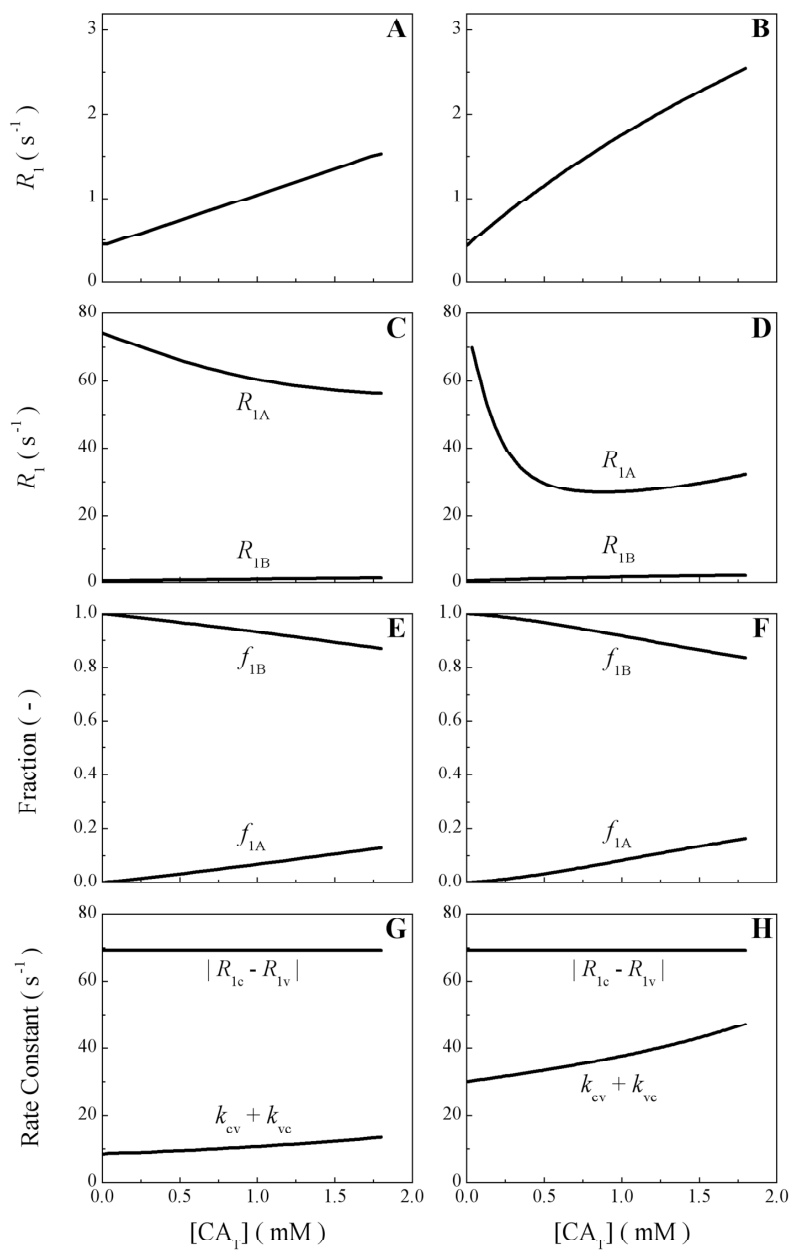


**Figure 5, Relaxation parameters as function of voxel CA concentration with variation of the number of CA-loaded vesicles from 0 to 5 large (A, C, E, G) or 0 to 220 small (B, D, F, H) vesicles. Figure panels are analogous to those of Figure 4. Model parameter values are given in Table 1.**

#### Calculation 4

For some validation, we have compared calculated relaxation rate constant CA-concentration dependences with literature reports. Figure 6A shows the observed  $^1\text{H}_2\text{O}$  relaxation rate constants for rat hepatoma cells incubated with Gd-DOTAMA- $\text{C}_6$ -Gln (open circles, data from ref. [13]). Gd-DOTAMA- $\text{C}_6$ -Gln is targeted towards the glutamine transporter system and is internalized into cells through receptor-mediated endocytosis. The solid curve is calculated for CA internalized into 35 1  $\mu\text{m}$  radius vesicles. Our model is able to quantitatively reproduce the quenching behavior, which occurs as a consequence of the endosomal CA entrapment. The agreement is remarkably good.

A second quantitative comparison is shown in Figure 6B, which displays the observed  $^1\text{H}_2\text{O}$  relaxation rate constants for RAW264.7 mouse macrophages incubated with anionic maghemite nanoparticles (open circles, data from ref. [16]). Here, the solid line is a calculation for the CA internalized into 20, 1- $\mu\text{m}$  radius vesicles. Thus, also for this FeO-based contrast agent, very good agreement between measured and calculated longitudinal relaxation rate constant CA-concentration dependence was found.

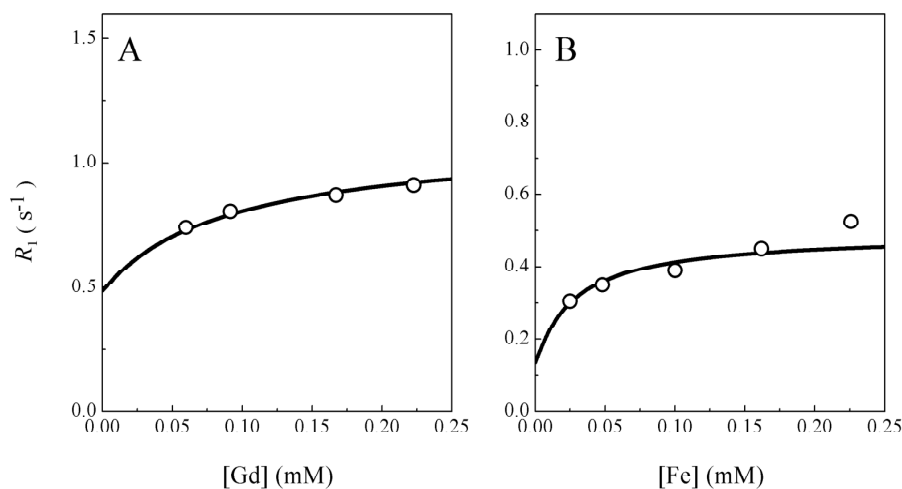


**Figure 6, Comparison of model calculations with experimental data. (A) Observed  $^1\text{H}_2\text{O}$  relaxation rate constants for rat hepatoma cells incubated with Gd-DOTAMA- $\text{C}_6$ -Gln (open circles). Reproduced with permission from ref. [13], Copyright 2006 American Chemical Society. The solid curve is calculated by the model with contrast agent internalized into 35 1- $\mu\text{m}$  radius vesicles. (B) Observed  $^1\text{H}_2\text{O}$  relaxation rate constants for RAW264.7 mouse macrophages incubated with anionic maghemite nanoparticles (open circles). Reproduced with permission from ref. [16], Copyright 2003 John Wiley & Sons, Inc. The solid curve is calculated by the model with contrast agent internalized into 20 1- $\mu\text{m}$  radius vesicles. Model parameter values are given in Table 1.**

**Discussion**

In this paper we have presented a three-compartment model to describe the  $T_1$ -relaxation time constant of systems with cell-internalized CA. The model employs a voxel containing three relevant compartments: extracellular, cytoplasmic and vesicular. Relaxation parameters were calculated for CA distributed in the cytoplasmic or in the vesicular compartments. The size and the number of CA-loaded vesicles were varied.

For the calculations we have chosen an extracellular volume fraction of 0.5. The extracellular water fractions in white matter and grey matter brain are estimated to be about 0.5 and 0.24 - 0.34, respectively, while about 0.09 - 0.19 for muscle tissue [25]. In tumor tissue the extracellular volume fraction can be considerably larger or smaller, depending on tumor type. For *in vitro* studies on loosely packed cell pellets this fraction may be in the range of 0.4 - 0.7. Our choice of  $v_e = 0.5$  is therefore applicable for *in vitro* studies on cell pellets but can be chosen differently when concentrating on specific tissue types. The volume fraction of non-aqueous constituents is conventionally ascribed to the cytoplasmic space [25].

The relatively large vesicular volume fraction (up to  $v_v = 0.107$ ) was motivated by recent reports on large accumulations of CA-loaded vesicles (Chapter 2 and refs. [8, 15, 16]). In calculations 2 and 3 vesicle radii of 3.5 and 1  $\mu\text{m}$  were assumed, which is in the range of experimentally observed endosomal and lysosomal vesicle sizes (Chapter 2 and refs. [8, 16]). The starting relaxation rate constants of the individual compartments in the absence of CA were chosen based on measurements of cell suspensions and literature values at typical field strengths and temperatures. The cytoplasmic  $^1\text{H}_2\text{O}$  relaxation rate constant was taken to be somewhat greater than the extracellular and vesicular values because of the typically larger cytoplasmic macromolecular volume fraction (Chapter 2 and ref. [8]).

It should be noted that for Eqs. 4-6 to be valid, intracellular mixing has to be sufficiently rapid that inverse mean residence times are a good approximation for first order elimination rate constants. Using the 3D Einstein diffusion equation,  $\langle r^2 \rangle = 6 D t_D$ , and assuming  $D = 1.5 \mu\text{m}^2/\text{ms}$  (a conservatively small value for mean intracellular water self-diffusion), and cell radius  $r_C = 10 \mu\text{m}$ , we obtain an average time for intracellular diffusion of  $t_D \approx 11 \text{ ms}$ , which is at least an order of magnitude smaller than typical cytoplasmic egress rate constant reciprocals. For example, for calculation 1 we obtained  $\tau_c = 170 \text{ ms}$ .

The analysis of the inversion recovery curves simulated with the three-compartment model was conducted using both mono- as well as bi-exponential fittings. For most of the calculations performed at high CA concentrations, each system was in its SXR condition, which means that bi-exponential fitting is more appropriate than mono-exponential fitting. In fact, since we are dealing with three compartments a tri-exponential fitting could be even more appropriate. However, because of noise in actual experimental data, only fitting with no more than two inversion recovery population fractions can normally be justified. Nevertheless, in an actual experimental setting the inversion recovery MRI sequence has to be executed with typically a long repetition time, which means that often only a limited number of inversion points can be recorded within a reasonable acquisition time. Consequently, even bi-exponential fitting is often inaccurate for experimental data and therefore we have also performed mono-exponential fitting resulting in an effective  $R_1$  of the whole voxel for the full CA concentration range.

It is tempting to assign the bi-exponential fitting relaxation rate constants  $R_{1A}$  and  $R_{1B}$  and corresponding population fractions  $f_{1A}$  and  $f_{1B}$  to water in the cytoplasmic or vesicular and extracellular compartments, respectively (A designating the CA-containing compartment). However, it is important to realize that these represent only *apparent* relaxation rates and population fractions. These would reflect true compartmental parameters only in the absence of exchange, the no-exchange-limit (NXL). In the slow-exchange-limit (SXL),  $f_{1A} = p_v$  or  $p_c$  (whichever has the CA), and  $f_{1B} = (p_c + p_e)$  or  $(p_v + p_e)$ . In the NXL, ( $\tau_x^{-1} \rightarrow 0$ ), additionally  $R_{1A} = R_{1v}$  or  $R_{1c}$  and  $R_{1B} = (p_c R_{1c0} + p_e R_{1e0})$  or  $(p_v R_{1v0} + p_e R_{1e0})$  [27].

In recent years there have been a number of reports on reduced relaxivity of cell-internalized CAs. Kobayashi *et al.* [12] have observed reduced longitudinal relaxivity after internalization of a Gd(III)-based CA into tumor cells. Lewin and coworkers [11] have investigated the internalization of Gd(III)-EOB-DTPA in cultured rat hepatocytes and two hepatoma cell lines, observing reduced longitudinal relaxivity of the internalized CA. Billotey *et al.* [16] have studied the uptake of anionic maghemite nanoparticles by macrophages and investigated their relaxation properties. It was shown that the intracellular confinement of maghemite nanoparticles within micrometer-sized endosomes resulted in significant longitudinal relaxivity decrease. Similarly, Simon *et al.* [10] have evaluated the effects of intracellular compartmentalization of ultrasmall superparamagnetic iron oxide (USPIO) in macrophages. Consistently lower longitudinal and transverse relaxivities were observed for the compartmentalized CA as compared to free USPIO. Relaxivity quenching was

observed for rat hepatoma cells incubated with Gd-DOTAMA-C<sub>6</sub>-Gln targeted towards the glutamine transporter system [13]. Terreno *et al.* [8] investigated several procedures to effectively shuttle Gd(III)-based CA into a rat hepatocarcinoma cell line. Internalization of the CA into the cytoplasm, which was achieved by electroporation, yielded considerably higher relaxivity as compared to CA entrapped in vesicles resulting from CA pinocytosis. Cytoplasmic CA distribution resulted in bi-exponential longitudinal relaxation behavior. Brekke *et al.* [15] have labeled murine neural stem cells with a bimodal Gd(III)-rhodamine-dextran (GRID) CA with similar findings. Finally, chapter 2 of this thesis describes experiments in which endothelial cells were labeled with paramagnetic liposomes targeted towards the  $\alpha_v\beta_3$ -integrin to specifically address the issue of the relaxivity quenching using a targeted agent. The targeted liposomes were internalized into large perinuclear vesicles by receptor-mediated endocytosis, which resulted in a considerable longitudinal relaxivity quenching.

Recently, an alternative MR cell-tracking approach has been introduced, which induces intracellular expression of an MR reporter protein for CEST (chemical exchange saturation transfer) MR contrast [27]. The sensitivity of this technique, and its quantitative analysis, will also crucially depend on equilibrium transcytolemmal water exchange kinetics. Most of the above studies have in common that considerably reduced longitudinal relaxivity was observed for CA internalized into cytoplasmic or subcellular compartments. Reference [8] is an important, even seminal, paper because it featured derivation of an (admittedly approximate) "pseudo-3SX" model to account for this. That report was submitted before the comprehensive, matrix-based 3SX model [7] appeared. The pseudo-3SX model suffers from constraint to the special case when the vesicular <sup>1</sup>H<sub>2</sub>O signal is negligible (" $<1\%$ "). Thus, it cannot accommodate calculations for significant vesicular volume fraction ( $v_v$ ) values. In contrast, our rigorous 3SX calculations are not so constrained, and run up to  $v_v = 0.107$  ( $\sim 11\%$ ) in Calculation 3 (Figure 5), as necessitated by recent experiments. Thus, the model presented in this paper provides a more general theoretical basis for this quenching behavior. Qualitatively and quantitatively the calculated CA-concentration dependencies of the relaxation rate constants are in good agreement with experimental findings. Quantitative comparisons were made with two different reports on relaxivity quenching of cell internalized Gd- and FeO-based CAs (refs. [13, 16]). By adjustment of only the vesicle number ( $n_v$ ) very good agreements between calculated and measured relaxation rate constant concentration dependencies were obtained. The present implementation includes three compartments. However, it is possible to increase the number to include for example an intravascular compartment in order to

model the relaxation behavior of a targeted CA *in vivo*. The model may be used to evaluate the design of CAs that evade entrapment and therefore quenching, which is highly desirable for *in vivo* cellular imaging and applications of targeted CAs.



### **Conclusions**

In summary, we have presented a three-compartment model to describe the longitudinal relaxivity of cell-internalized CA. Several scenarios for internalized CA fate were evaluated, including cytoplasmic as well as vesicular distributions. The observed dependence of  $R_1$  with CA concentration can be used to qualitatively and quantitatively understand a number of different experimental observations in the literature. Most importantly the calculations reproduce the relaxivity quenching for cell-internalized CA that has been observed experimentally.

## Literature

1. Strijkers, G.J., W.J. Mulder, G.A. van Tilborg, *et al.*, *Anticancer Agents Med Chem*, 2007. **7**(3): p. 291-305.
2. Mulder, W.J., A.W. Griffioen, G.J. Strijkers, *et al.*, *Nanomed*, 2007. **2**(3): p. 307-324.
3. Aime, S., A. Barge, C. Cabella, *et al.*, *Curr Pharm Biotechnol*, 2004. **5**(6): p. 509-518.
4. Modo, M., M. Hoehn, J.W. Bulte, *Mol Imaging*, 2005. **4**(3): p. 143-164.
5. Yankeelov, T.E., W.D. Rooney, X. Li, *et al.*, *Magn Reson Med*, 2003. **50**(6): p. 1151-1169.
6. Yankeelov, T.E., J.J. Luci, L.M. Debusk, *et al.*, *Magn Reson Med*, 2008. **59**(2): p. 326-335.
7. Li, X., W.D. Rooney, C.S. Springer, *Magn Reson Med*, 2005. **54**(6): p. 1351-1359 [Erratum: *Magn Reson Med* 2006;1355:1217.].
8. Terreno, E., S. Geninatti Crich, S. Belfiore, *et al.*, *Magn Reson Med*, 2006. **55**(3): p. 491-497.
9. Tanimoto, A., K. Oshio, M. Suematsu, *et al.*, *J Magn Reson Imaging*, 2001. **14**(1): p. 72-77.
10. Simon, G.H., J. Bauer, O. Saborovski, *et al.*, *Eur Radiol*, 2006. **16**(3): p. 738-745.
11. Lewin, M., O. Clement, P. Belguise-Valladier, *et al.*, *Invest Radiol*, 2001. **36**(1): p. 9-14.
12. Kobayashi, H., S. Kawamoto, T. Saga, *et al.*, *Bioconjug Chem*, 2001. **12**(4): p. 587-593.
13. Geninatti Crich, S., C. Cabella, A. Barge, *et al.*, *J Med Chem*, 2006. **49**(16): p. 4926-4936.
14. Brekke, C., S.C. Williams, J. Price, *et al.*, *Neuroimage*, 2007. **37**(3): p. 769-782.
15. Brekke, C., S.C. Morgan, A.S. Lowe, *et al.*, *NMR Biomed*, 2007. **20**(2): p. 77-89.
16. Billotey, C., C. Wilhelm, M. Devaud, *et al.*, *Magn Reson Med*, 2003. **49**(4): p. 646-654.
17. Louie, A.Y., M.M. Huber, E.T. Ahrens, *et al.*, *Nat Biotechnol*, 2000. **18**(3): p. 321-325.
18. Spencer, R.G., K.W. Fishbein, *J Magn Reson*, 2000. **142**(1): p. 120-135.
19. Mulkern, R.V., A.R. Bleier, I.K. Adzamlı, *et al.*, *Biophys J*, 1989. **55**(2): p. 221-232.
20. Horska, A., J. Horsky, R.G.S. Spencer, *Measurement of Spin-Lattice Relaxation-Times in Systems Undergoing Chemical-Exchange*, in *J Magn Reson Ser A*. 1994. p. 82-89.
21. Galbán, C.J., R.G. Spencer, *Magn Reson Med*, 2007. **58**(1): p. 8-18.
22. Woessner, D.E., *J Chem Phys*, 1961. **35**(1): p. 41-48.
23. McConnell, H.M., *J Chem Phys*, 1958. **28**: p. 430-431.
24. Chen, S.T., C.S. Springer, *Biophys Chem*, 1981. **14**(4): p. 375-388.
25. Landis, C.S., X. Li, F.W. Telang, *et al.*, *Magn Reson Med*, 1999. **42**(3): p. 467-478.
26. Garrick, R.A., U.S. Ryan, F.P. Chinard, *Am J Physiol*, 1988. **255**(3 Pt 1): p. C311-314.
27. Gilad, A.A., M.T. McMahon, P. Walczak, *et al.*, *Nat Biotechnol*, 2007. **25**(2): p. 217-219.



## Chapter **4**

### **Dynamic changes in $^1\text{H}$ -MR relaxometric properties of cell-internalized paramagnetic liposomes, as studied over a 5-day period**

**Based on:**

*Dynamic changes in  $^1\text{H}$ -MR relaxometric properties of cell-internalized paramagnetic liposomes, as studied over a 5-day period*

M.B. Kok, G.J. Strijkers, K. Nicolay

Submitted

**Abstract**

Molecular imaging based on MRI requires the use of amplification strategies in order to achieve sufficient sensitivity for the detection of low-level molecular markers. Recently, we described a combination of two amplification methods: (i) the use of paramagnetic liposomes that can be prepared with a high payload of  $Gd^{3+}$ -containing lipid, and (ii) targeting to a cell-surface receptor that can undergo multiple rounds of nanoparticle delivery in the cell, followed by recycling to the cell membrane. Liposome uptake was monitored over a period of 24 hr and was found to lead to massive delivery in subcellular compartments. The present study was aimed to monitor the longer-term fate of the cell-internalized contrast material by studying its relaxometric properties over 5 days, following an initial 24 hr loading period. Circa 25% of the  $Gd^{3+}$ -content delivered to the cells via integrin-targeted liposomes was lost in the first 24 hr, which led to 65% and 77% reductions in  $R_1$  and  $R_2$ , respectively, as compared to the original  $R_1$  and  $R_2$  enhancements. This implies that the remaining cell-associated gadolinium had relatively low effective  $r_1$  and  $r_2$  relaxivities. It is proposed that this is due to gradual release of  $Gd^{3+}$  from the chelate in the cell, followed by sequestration in a MR silent state. Most of the gadolinium internalized by cells following incubation with non-targeted liposomes was released in the 5-day follow-up period.

## Introduction

The field of molecular MR imaging concerns the development and use of targeted contrast agents with the aim to visualize molecular markers that are up-regulated during disease. One prominent approach in molecular MRI is the use of  $\text{Gd}^{3+}$ -based paramagnetic contrast agents that produce a local shortening of the  $T_1$  relaxation time. The most suitable design of these  $\text{Gd}^{3+}$ -based agents depends on the specific application, such as the abundance and accessibility of the intended target. Low numbers of  $\text{Gd}^{3+}$  per contrast agent construct may suffice for high-level targets, while a high Gd payload is typically required for the detection of low-level targets. Nanoparticles can be equipped with many Gd-chelates and therefore are extensively studied for their utility in molecular MRI [1, 2]. In recent years, we have explored the use of paramagnetic liposomes, a major class of biocompatible nanoparticles that can be prepared in a range of sizes, generally between 50 and 500 nm [1]. The liposomes are mainly made from naturally occurring lipids, such as phosphatidylcholine and cholesterol, and therefore their prime constituents are biocompatible and well suited for biomedical applications. For MRI contrast, we typically include 25 mole percent of a non-natural lipid, which contains a Gd-chelate in the polar head group. The Gd-chelate is thus located in the interface between the hydrophobic interior of the liposomal bilayer and the surrounding aqueous medium, ensuring efficient access of bulk water protons to the paramagnetic center. Relaxometric studies of paramagnetic liposomes, equipped with 25 mole percent Gd-DTPA-bis(stearylamide) [3], indicated that their relaxivity  $r_1$  should enable the detection of molecular markers in the sub-nM concentration range. Based on these findings, we have recently studied the *in vitro* homing of cyclic RGD-conjugated paramagnetic liposomes to cultured endothelial cells over-expressing the  $\alpha_v\beta_3$ -integrin cell-surface receptor. This cyclic RGD-integrin ligand-target couple has been widely studied and therefore is very attractive for investigating critical aspects of target-specific MRI. The initial studies involved up to 24 hr incubations of human umbilical vein endothelial cells (HUVEC) with RGD-conjugated and non-conjugated liposomes (Chapter 2). It was found that functional, integrin-targeted liposomes were abundantly taken up by the HUVEC and were mainly localized in intracellular vesicles in the perinuclear region of the cell. The uptake of RGD-liposomes most likely occurred via receptor-mediated endocytosis as the  $\alpha_v\beta_3$ -integrin is known to be an internalizing receptor. This is, in principle, an attractive targeting concept: it involves the receptor to recycle back to the cell membrane after cargo delivery, thus enabling amplified uptake of imaging agent into the target cell over-expressing the disease marker. Functional paramagnetic liposomes were taken up by HUVEC in a 15-fold higher amount than their non-functional counterparts (Chapter 2). Importantly, however, the increase in cellular longitudinal relaxation rate  $R_1$  brought about by

integrin-targeted and non-targeted particles differed much less (circa 3.7- versus 3.4-fold, respectively). This implies that the effective relaxivity  $r_1$  of the functional liposomes was strongly reduced compared to its intrinsic value. Using mathematical modeling as was presented in Chapter 3, convincing evidence was presented that this so-called  $r_1$  quenching effect is due to confinement of the paramagnetic material in a low-volume fraction intracellular compartment from which water proton exchange with the bulk is too slow to come to full expression of the intrinsic liposomal  $r_1$ . The effects of cell internalization of the liposomes on their  $r_2$  were relatively small and rather indicated a somewhat increased  $T_2$  shortening effect (Chapter 2). Cytotoxicity assays indicated that the high amounts of cell-internalized liposomes caused minimal cell death over the 24-hr incubation period (Chapter 2).

The purpose of the present study was to examine the relaxometric properties of HUVEC-associated paramagnetic liposomes over a period of 5 days. To this aim, HUVEC were incubated with either  $\alpha_v\beta_3$ -integrin targeted or non-targeted liposomes for 24 hr. After this initial loading period, fresh liposome-free growth medium was supplied and cell samples were collected over a period of 120 hr and analyzed using MRI, fluorescent activated cell sorting (FACS), inductively coupled plasma mass spectrometry (ICP-MS) and confocal laser scanning microscopy (CLSM). These experiments provide important insights in the longer-term fate of cell-internalized liposomes and possible changes in their effective  $T_1$ - and  $T_2$ -shortening capacity. This study is also relevant for MRI-based cell tracking research, in which cells are loaded *in vitro* with paramagnetic contrast agent, followed by *in vivo* implantation and long-term MRI monitoring of cell migration [4-8].

## Materials and Methods

### Materials

1,2-Distearoyl-*sn*-glycero-3-phosphocholine (DSPC), cholesterol, 1,2-distearoyl-*sn*-glycero-3-phosphoethanolamine-N-[methoxy(polyethyleneglycol)-2000] (PEG<sub>2000</sub>-DSPE), 1,2-distearoyl-*sn*-glycero-3-phosphoethanolamine-N-[maleimide(polyethyleneglycol)-2000] (Mal-PEG<sub>2000</sub>-DSPE) and 1,2-dipalmitoyl-*sn*-3-phosphoethanolamine-N-[lissamine rhodamine B sulfonyl] (rhodamine-PE) were obtained from Avanti Polar Lipids (Alabaster, AL, USA). Gd-diethylenetriaminepentaacetic acid-bis(stearylamide) (Gd-DTPA-BSA) was purchased from Gateway Chemical Technology (St. Louis, MO, USA). Endothelial Growth Medium-2 (EGM-2) and human umbilical vein derived endothelial cells (HUVECs) were ordered with Lonza Bioscience (Switzerland). Monoclonal mouse anti-human CD31 antibody was obtained from Dakocytomation (Glostrup, Denmark). Polyclonal rabbit anti- $\alpha_v\beta_3$  integrin primary antibody was purchased from Millipore (Billerica, MA, USA). DAPI, Alexa Fluor 488 conjugated goat anti-mouse secondary antibody and Alexa Fluor 488 conjugated goat anti-rabbit secondary antibody were from Molecular Probes Europe BV (Leiden, The Netherlands). Cyclic RGD (RGD, c(RGDf(-S-acetylthioacetyl)K)) was synthesized by Ansynth Service BV (Roosendaal, The Netherlands). All other chemicals were obtained from Sigma (St. Louis, MO, USA) and were of analytical grade or the best grade available.

### Liposome preparation and characterization

200 nm-diameter liposomes containing Gd-DTPA-BSA, DSPC, cholesterol, PEG<sub>2000</sub>-DSPE and Mal-PEG<sub>2000</sub>-DSPE at a molar ratio of 0.75/1.10/1/0.075/0.075 were produced by lipid film hydration and extrusion according to Mulder *et al.* [9]. In short, the lipids were dissolved in a 1:5 methanol:chloroform mixture. As a fluorescent marker, 0.1 mole percent of rhodamine-PE was added. A lipid film was created by evaporating the chloroform/methanol mixture using a Rotavapor R200 (Buchi, Flawil, Switzerland). Then the lipid film was hydrated at 67 °C using a HEPES buffered saline solution (HBS), containing 20 mM HEPES and 135 mM NaCl (pH 6.7). The lipid suspension was extruded at 67 °C, twice through a single 200 nm polycarbonate membrane (Whatman, Kent, UK) and 6 times through a double 200 nm polycarbonate membrane. After extrusion, half of the liposome suspension was modified with a RGD-peptide (6  $\mu\text{g}/\mu\text{mol}$  total lipid) to target the  $\alpha_v\beta_3$ -integrin. The RGD-peptide was deacetylated and coupled to the distal end of Mal-PEG<sub>2000</sub>-DSPE. After incubation overnight, at 4 °C, both batches of liposomes were centrifuged at 310,000 g for 45 min. Centrifugation was used, in case of RGD-liposomes, to remove unconjugated RGD-peptide. The pellets were resuspended in HBS, pH 7.4. Lipid concentration was measured by phosphate



determination according to Rouser *et al.* [10]. Size and size-distribution of the liposomes was determined with dynamic light scattering (DLS) (Zetasizer Nano, Malvern, UK) at 25 °C. The gadolinium concentration was determined using inductively coupled plasma atomic emission spectroscopy (ICP-AES) by Philips Research (Eindhoven, The Netherlands). Both the longitudinal and transverse relaxivity were determined (6.3 T, 20 °C) by fitting  $R_1$  ( $1/T_1$ ) and  $R_2$  ( $1/T_2$ ) values as a function of the gadolinium concentration of the liposome suspension using the least squares method. In the remainder of this paper we refer to liposomes that were conjugated with cyclic RGD as RGD-liposomes. Non-targeted liposomes that were not conjugated with a targeting ligand will be referred to as NT-liposomes.

#### Cell Culture

Human umbilical vein derived endothelial cells (HUVECs) were used in all experiments. Cells were stored in liquid nitrogen upon arrival. Before use, the cells were quickly thawed in a water bath ( $T = 37$  °C) and divided over 2 gelatin-coated T75 TCPS flasks (VWR, West Chester, PA, USA). Cells were cultured in a humidified incubator at 37 °C with 5%  $\text{CO}_2$ . The EGM-2 medium was replaced every 2-3 days. Cells were cultured according to procedures provided by the supplier. For the experiments, HUVECs were grown to 100% confluency and immediately used thereafter.

#### Experimental Setup

Cells of passage 3 or 4 were used for all experiments at 100% confluency. Incubation was carried out on both gelatin-coated coverslips, for CLSM analysis, and in gelatin-coated T75 TCPS culture flasks, for MRI, FACS and ICP-AES analysis. All measurements were done in triplicate for both types of liposomes and each incubation time. To start the experiment, HUVECs were initially loaded with contrast agent by incubating them with either RGD- or NT-liposomes for 24 hr using medium containing a concentration of 1  $\mu\text{mol}$  total lipid per mL. 4 mL of liposome containing medium was added to each T75 gelatin-coated TCPS flask and 0.5 mL of medium was added to each gelatin-coated coverslip. After the initial 24-hr liposome incubation, the contrast agent-containing medium was aspirated and the cells were washed three times to remove non-adherent liposomes. Thereafter 20 mL and 2.5 mL of fresh medium was supplied to each T75 TCPS culture flask and gelatin coated coverslip, respectively. Samples were collected after up to 120 hr of incubation with fresh medium. After incubation, the cells were washed twice with 5 mL pre-warmed (37 °C) HEPES-buffered saline solution. After these washing steps, the cells grown on coverslips were fixed using 4% PFA for 15 min at room temperature. Cells in culture flasks were detached using 2 mL 0.25% trypsin 1 mM EDTA·4Na (Lonza

Bioscience, Switzerland). The trypsin solution was neutralized using 4 mL trypsin neutralizing solution (Lonza Bioscience, Basel, Switzerland). Cells were spun down at 220 g and the supernatant was removed and the cell pellet was resuspended in 200  $\mu\text{L}$  4% paraformaldehyde solution in PBS and transferred to a 300  $\mu\text{L}$  Eppendorf cup. A loosely-packed cell pellet was allowed to form by 4 days of storage in the dark at 4  $^\circ\text{C}$ . Remaining cells were resuspended in 300  $\mu\text{L}$  of PBS and used as cell suspension for FACS analysis (BD FACSCanto, BD Bioscience, Franklin Lakes, NJ, USA)

#### Magnetic Resonance Imaging of cell pellets

The  $T_1$  and  $T_2$  relaxation times and the volume of the pellets were measured using a 6.3 T horizontal bore animal MR scanner (Bruker, Ettlingen, Germany). All measurements were carried out at room temperature. Longitudinal and transverse relaxation times were measured in a 3-cm-diameter send and receive quadrature-driven birdcage coil (Rapid Biomedical, Rimpar, Germany). The Eppendorf tubes containing the loosely-packed cell pellets were placed in a custom made holder (4 tubes at a time) that was filled with HEPES buffered saline solution to facilitate shimming.  $T_1$  was measured using a fast inversion recovery segmented FLASH sequence with: TE = 1.5 ms, TR = 3.0 ms,  $\alpha = 60^\circ$ , inversion time (TI) = 67 to 4800 ms in 80 steps, FOV =  $3 \times 3 \text{ cm}^2$ , matrix =  $128 \times 128$ , slice thickness = 0.75 mm and NA = 2. The overall repetition time was 20 s.  $T_2$  was measured using a multi-spin-echo sequence with: TE = 9 to 288 ms in 32 steps, TR = 1000 ms, FOV =  $3.0 \times 2.2 \text{ cm}^2$ , matrix =  $128 \times 128$ , slice thickness = 0.75 mm, and NA = 4. From the images a  $T_1$ - or  $T_2$ -map was calculated using Mathematica (Wolfram Research Inc, Champaign, IL, USA).  $T_1$  and  $T_2$  of the different cell pellets were determined by selecting a region-of-interest within the pellet. The volume of the cell pellet was determined for each sample separately in a 0.7-cm-diameter solenoid coil using a 3D FLASH sequence with: TE = 3.2 ms, TR = 25 ms,  $\alpha = 30^\circ$ , FOV =  $1.6 \times 1.6 \times 1.6 \text{ cm}^3$ , matrix =  $128 \times 128 \times 128$ , and NA = 1. Pellet volume was determined by manually setting threshold values to select the voxels inside the pellet. The segmented voxels were multiplied by the voxel volume to obtain the total volume of the pellet. The concentration of gadolinium in each cell pellet was determined by dividing the gadolinium content as determined by ICP-AES by the pellet volume.

#### Immunofluorescence

After fixation, the coverslips with HUVECs incubated with liposomes were stained using a mouse anti-human CD31 antibody to visualize the cellular membrane. The cells were rinsed for 5 min with PBS followed by 60 min of incubation with the primary mouse anti-human CD31 antibody (1:40 dilution).

Subsequently the cells were washed 3x 5 min with PBS followed by 30 min of incubation with a secondary Alexa Fluor 488 goat anti-mouse IgG antibody (1:200 dilution). The cells were washed 3x 5 min with PBS and the nuclei were stained for 5 min with DAPI. After staining of the nuclei the cells were rinsed 3x 5 min with PBS and subsequently mounted on a microscopy slide using Mowiol Mounting Medium. For staining of the  $\alpha_v\beta_3$  integrin, first a 15 min blocking step was used, consisting of incubation with 5% (v/v) rabbit serum in PBS, which was followed by incubation with the primary mouse anti- $\alpha_v\beta_3$  integrin antibody (1:50 dilution) for 60 min. Next, the cells were rinsed 3x 5 min with PBS and subsequently incubated with Alexa Fluor 488 goat anti-mouse IgG antibody (dilution 1:200) for 1 hr. Then cells were washed 3x 5 min with PBS and the nuclei were stained for 5 min with DAPI. After staining of the nuclei, the cells were rinsed 3x 5 min with PBS and subsequently mounted on a microscopy slide using Mowiol Mounting Medium.

#### Confocal Laser Scanning Microscopy

Confocal fluorescence images were recorded at room temperature on a Zeiss LSM 510 META system using a Plan-Apochromat<sup>®</sup> 63x/1.4 NA oil-immersion objective. Alexa Fluor 488 and rhodamine-PE were excited using the 488 and 543 nm line of a HeNe laser, respectively. The fluorescence emission of Alexa Fluor 488 and LysoTracker green were recorded with photomultiplier tubes (Hamamatsu R6357) after spectral filtering with a NFT 490 nm beamsplitter followed by a 500-550 nm bandpass filter. Rhodamine-PE emission was analyzed using the Zeiss Meta System in a wavelength range of 586-704 nm. DAPI staining of nuclei was visualized by two-photon excitation fluorescence microscopy, using the same Zeiss LSM 510 system. Excitation at 780 nm was provided by a pulsed Ti:Sapphire laser (Chameleon<sup>™</sup>; Coherent, Santa Clara, CA, USA), and fluorescence emission was detected with a 395-465 nm bandpass filter. All experiments were combined in multitrack mode and acquired confocally.

## Results

The characteristics of cell-internalized paramagnetic, fluorescent liposomes were studied over a period of 5 days. The cellular location of the contrast agent was determined using CLSM, exploiting the fluorescent rhodamine-PE lipid present in the bilayer of the liposomes. The left column of Figure 1 shows confocal images of HUVEC grown on gelatin-coated coverslips, following 24-hr incubations with RGD- or NT-liposomes. CLSM revealed a cobblestone-like structure of the HUVEC, which is characteristic for healthy, confluent endothelial cells. This morphology was observed throughout the entire experiment, for both RGD- and NT-liposome treated cells. For incubations with RGD-liposomes, large rhodamine-PE positive vesicular structures with a diameter of 1-5  $\mu\text{m}$ , were observed throughout the cytoplasm. Incubation with NT-liposomes resulted predominantly in staining of the perinuclear region of the cell and fluorescent signal in this case originated from more sharply defined and smaller (*i.e.* 0.4-1.0  $\mu\text{m}$  diameter) spherical vesicles. No detectable association of liposomes with the cellular membrane was observed for both RGD- and NT-liposome incubated HUVEC. These CLSM data are in line with the previous study (Chapter 2), except that the higher degree of confluency of the cells resulted in sharper delineation of CD31 positive cell-cell junctions.

Following removal of the liposomes after 24 hr and continued incubation with fresh medium, over time distinct differences were observed in spatial distribution and intensity of fluorescent signal from HUVEC pre-incubated with RGD- or NT-liposomes. Up to 48 hr after initial loading of the HUVECs with RGD-liposomes, the rhodamine signal was located in sharply-defined vesicular structures present throughout the entire cytoplasm. For longer incubation times the vesicular structures became less sharply defined. Also a diffuse cytoplasmic rhodamine signal was observed after 48 hr of incubation, which intensified up to 120 hr of incubation. NT-liposomes showed a different behavior. After loading of the HUVECs, the rhodamine signal mainly originated from small vesicular structures in the perinuclear region of the cell. Over time the number of rhodamine PE-positive vesicles gradually decreased and very little fluorescence was observed at the 120 hr time point.

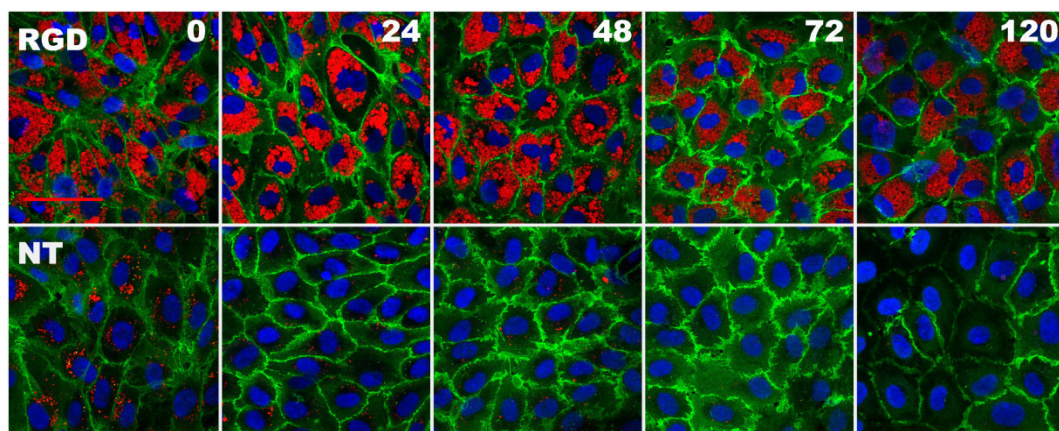


**Figure 1, CLSM images of HUVECs after loading of the cells with RGD-liposomes (RGD) or NT-liposomes (NT). The number shown in the top right corner represents the incubation time with fresh medium after the initial 24 hr loading with paramagnetic liposomes.**

FACS was used to measure the mean rhodamine PE fluorescence intensity (MFI) per cell (Figure 2A and B). MFI data were indicative of a 35-fold higher uptake of RGD-liposomes after 24 hr of incubation, compared to NT-liposomes. FACS revealed a 31 % reduction in MFI for RGD-liposome treated HUVEC over the first 24-hr incubation with liposome-free medium, after which an essentially stable level of cell-associated fluorescence was observed up to the final measurement at 120 hr (Figure 2A). HUVEC incubated with NT-liposomes showed a very different behavior (Figure 2B). At the 72 hr time point, the MFI was reduced by circa 85 % after which no further decrease occurred.

ICP-MS was used to quantify Gd levels in loosely packed pellets of HUVEC (Figure 2C and 2D), which were prepared for quantitative relaxometric MRI measurements. The initial 24-hr loading with RGD-liposomes resulted in a concentration of  $2.46 \pm 0.14$  mM Gd in the cell pellet (Figure 2C). Following 24 hr incubation with fresh medium, the cellular Gd level had reduced to  $1.96 \pm 0.03$  mM, while a further minor decrease to  $1.84 \pm 0.06$  mM was noted at the 120 hr time point. The latter value represents a 25 % drop in Gd levels over 120 hr. Pre-incubation with NT-liposomes resulted in an initial gadolinium concentration of  $0.20 \pm 0.01$  mM (Figure 2D), which decreased to a value of  $0.06 \pm 0.01$  mM after 120 hr of incubation with contrast agent free medium, corresponding to a 71 % reduction in cell-associated Gd. Most of the Gd loss from HUVEC incubated with NT-liposomes occurred in the first 24 hr.

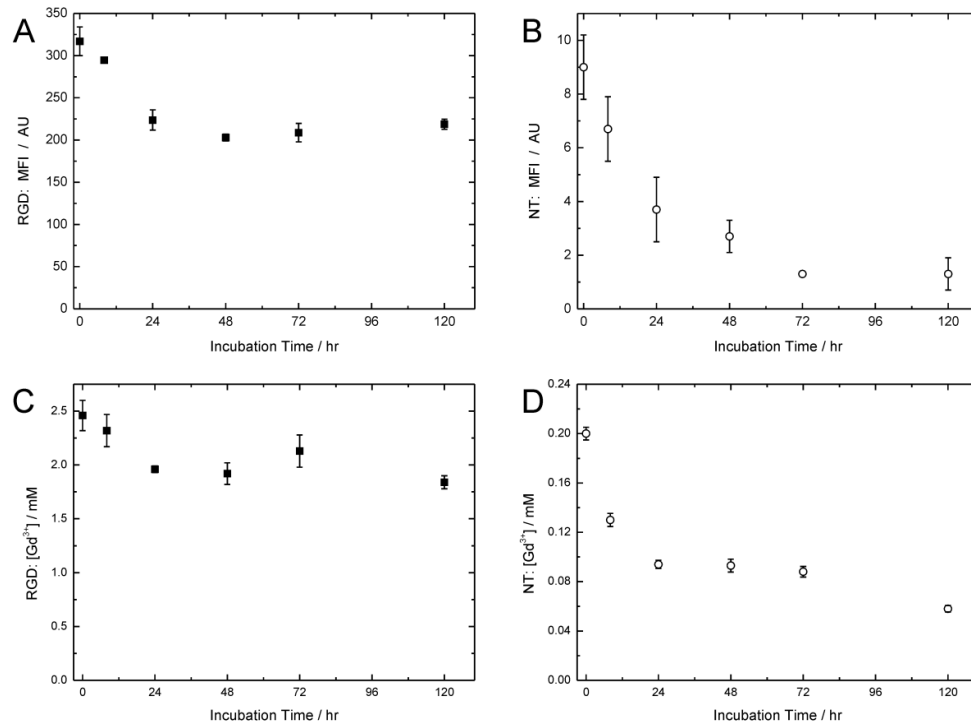


**Figure 2, Mean fluorescence intensity (MFI) per cell (A, B) and the cellular gadolinium concentration (C, D) as a function of incubation time for RGD-liposomes (solid squares) and NT-liposomes (open circles). MFI was normalized to the MFI of control cells. Note that the y-axis scales differ for RGD- and NT-liposomes. Data represent mean  $\pm$  SD (n=3)**

The results of quantitative  $T_1$  and  $T_2$  measurements on loosely-packed pellets of HUVEC are depicted in Figure 3 and 4. Figure 3 shows the relationship between the longitudinal relaxation rate  $R_1$ , as measured by MRI at 6.3 T, and the concentration of Gd, as quantified by ICP-MS. The  $R_1$  data are presented as a function of Gd levels (rather than incubation time) to enable a more straightforward estimation of the effective ionic relaxivity  $r_1$  (see Discussion). The  $R_1$  of HUVEC incubated with RGD-liposomes declined from an initial value of  $1.78 \pm 0.11 \text{ s}^{-1}$  to a final value of  $0.93 \pm 0.10 \text{ s}^{-1}$  after 120 hr. Over the same 120 hr period, the  $R_1$  of HUVEC pre-incubated for 24 hr with NT-liposomes dropped from  $1.59 \pm 0.10$  to  $0.74 \pm 0.04 \text{ s}^{-1}$  (Figure 3). It should be noted that the  $R_1$  of control HUVEC prior to incubation with paramagnetic liposomes was  $0.47 \pm 0.02 \text{ s}^{-1}$  at 6.3 T, as averaged from measurements of control HUVEC at each time point. These data imply that the increases in cellular  $R_1$ , originally brought about by incubations with RGD- and NT-liposomes, were reduced by 65 % and 76 %, respectively, at the 120 hr time point.

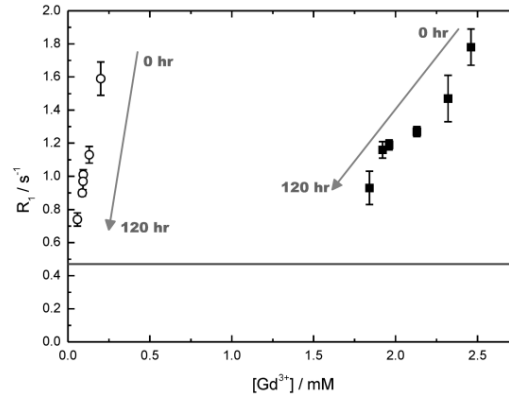


**Figure 3,  $R_1$  versus gadolinium concentration of loosely-packed pellets of HUVEC. Longitudinal relaxation rates ( $R_1$ ) were measured at 6.3 T. Solid squares: HUVEC pre-incubated with RGD-liposomes; open circles: HUVEC pre-incubated with NT-liposomes, in both cases followed by incubation with liposome-free medium. Data represent mean  $\pm$  SD ( $n=3$ ). The arrows indicate the prolongation of incubation times. The solid grey line is the  $R_1$  value measured for control HUVECs.**

Similar measurements on the influence of prolonged HUVEC incubations in liposome-free growth medium on the transverse relaxation rate  $R_2$  are shown in Figure 4.  $R_2$  values of HUVEC pre-loaded with RGD-liposomes were reduced from  $115.1 \pm 6.2 \text{ s}^{-1}$  to  $50.0 \pm 6.5 \text{ s}^{-1}$  over 120 hr. For the case of NT-liposomes, the transverse relaxation rates dropped from  $34.3 \pm 1.6 \text{ s}^{-1}$  to  $32.1 \pm 0.9 \text{ s}^{-1}$ , closely approaching the  $R_2$  of control HUVEC ( $30.4 \pm 1.4 \text{ s}^{-1}$ ). The data corresponds to  $R_2$  reductions of 77% and 57% compared to the original  $R_2$  enhancements for the case of RGD- and NT-liposomes, respectively.

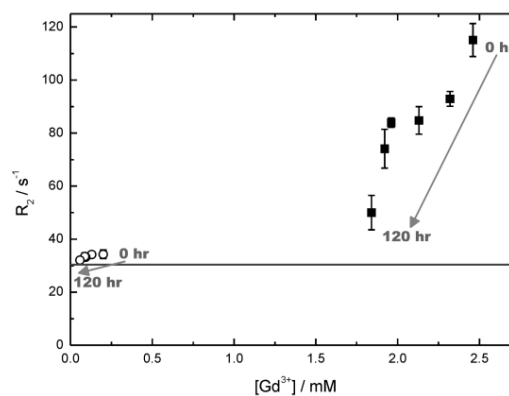


**Figure 4,  $R_2$  as a function of concentration of gadolinium in cell pellets for RGD-liposome (solid squares) and NT-liposome (open circles) incubated HUVECs. Data represent mean  $\pm$  SD ( $n=3$ ). The arrows indicate the prolongation of incubation times. The solid grey line is the  $R_2$  value measured for control HUVECs.**

## Discussion and Conclusion

The primary aim of the present study was to measure the relaxometric properties of cell-internalized targeted liposomal contrast agents over a period of 5 days. Relaxometry was supported by FACS and fluorescence microscopy, both of which made use of liposomal rhodamine-PE. In line with our earlier study (Chapter 2), RGD-conjugated liposomes were massively internalized by HUVEC. The absolute level of Gd incorporation was slightly lower as compared to previous experiments, which possibly is due to the high cell confluency. This was close to 100 %, compared to 80-90 % before and may have led to a more quiescent state of the HUVEC and, consequently, lower levels of  $\alpha_v\beta_3$ -integrin expression and lower rates of endocytosis. The non-targeted liposomes were taken up to low levels, similar to data reported in Chapter 2.

The key findings of the experiments with integrin-targeted RGD-liposomes are that over the 5-day follow-up period a moderate reduction in the levels of HUVEC-associated Gd (*i.e.* 25 %; Figure 2C) caused a strong decrease in cellular  $R_1$  enhancement (*i.e.* 65 %; Figure 3). The latter number was calculated by taking the  $R_1$  of non-liposome incubated HUVEC as a reference. From the RGD-liposome data in Figure 3, we estimated that the effective relaxivity  $r_1$  of the Gd pool, which was released from the cells over 120 hr, amounted to circa  $1.16 \pm 0.15 \text{ mM}^{-1}\text{s}^{-1}$ . This  $r_1$  estimation assumed a linear relationship between  $R_1$  and Gd concentration. The  $R^2$  of the linear fit was 0.93. A very different picture emerged, when applying a similar analysis to the NT-liposome data. Figure 2D demonstrates that 71 % of the Gd was released from the cells over 5 days in this case. Interestingly, the data in Figure 3 reveal that the original  $R_1$  increase compared to control HUVEC was reduced in a similar proportion, *i.e.* by 76 %, over the same time span. The effective relaxivity  $r_1$  of the released Gd pool was estimated to be circa  $5.85 \pm 0.32 \text{ mM}^{-1}\text{s}^{-1}$  in case of HUVEC pre-incubated with NT-liposomes (the  $R^2$  was 0.98). Similar estimations of the effective  $r_2$  of Gd lost from the cells over the 120 hr time period were applied to the  $R_2$  data depicted in Figure 4. Linear relationships between  $r_2$  and [Gd] were assumed to hold, in line with the above  $r_1$  analysis. Effective  $r_2$ 's of  $79.9 \pm 18.2$  and  $13.9 \pm 5.0 \text{ mM}^{-1}\text{s}^{-1}$  were estimated for RGD- and NT-liposome data, respectively ( $R^2$ 's were 0.82 and 0.72, respectively).

It is interesting to compare the above numbers on estimated effective relaxivities  $r_1$  and  $r_2$  for Gd released from the cells over the 5-day observation period to the intrinsic relaxivities of the paramagnetic liposomes that were used in this study. In agreement with our previous findings on the effective  $r_1$  relaxivities of paramagnetic liposomes internalized by HUVEC over a 24 hr period (Chapter 2), the effective  $r_1$  of Gd released from the RGD-liposome



treated cells in the present study was lower ( $1.2 \text{ mM}^{-1}\text{s}^{-1}$ ) than the intrinsic  $r_1$  of RGD-liposomes ( $2.1 \text{ mM}^{-1}\text{s}^{-1}$ ), while that of the Gd released from NT-liposome treated cells was considerably higher ( $5.9 \text{ mM}^{-1}\text{s}^{-1}$ ) than that of the NT-liposomes ( $2.3 \text{ mM}^{-1}\text{s}^{-1}$ ) in buffer at 6.3 T (Chapter 2). The opposite holds true for the comparison of the effective  $r_2$ 's of released Gd. For RGD-liposomes we found values of  $79.2 \text{ mM}^{-1}\text{s}^{-1}$ , compared to a value of  $17.3 \text{ mM}^{-1}\text{s}^{-1}$  for RGD-liposomes as prepared. The release pattern of NT-liposomes corresponded to an effective  $r_2$  of  $17.7 \text{ mM}^{-1}\text{s}^{-1}$ , compared to an intrinsic value of  $19.6 \text{ mM}^{-1}\text{s}^{-1}$ . Clearly, the interpretations of the present data are limited by the lack of insights in the molecular organization of the Gd-containing structures from which it was released and in which it remained associated with the cells. Nevertheless, when combining the relaxometry data with the fluorescence microscopy data, the following picture emerges. The high local levels of Gd that are concentrated in relatively large intracellular inclusions following 24-hr treatment with RGD-liposomes, inevitably cause a reduction in  $r_1$  and an elevation in  $r_2$  (Chapter 3). Not surprisingly, the initial release of Gd from the RGD-liposomes treated cells is also associated with a relatively mild reduction in  $R_1$  and a strong reduction in  $R_2$ . Using similar reasoning, the low level of delivery of NT-liposomes to relatively small cellular structures can explain the absence of any  $r_1$  quenching and  $r_2$  elevation effect. The reason for the supranormal effective  $r_1$  of cell-associated NT-liposomes, both during the loading and the release phase of our study remains to be clarified. This possibly has to do with a loss of structural integrity of the liposomes leading to an increased  $T_1$ -shortening contribution from Gd-lipid in the inner leaflet of the liposomal bilayer (see Chapter 2).

It is tempting to speculate on the relaxometric properties of the Gd remaining associated with the cells at long incubation times following loading with RGD-liposomes. Extrapolation of the  $R_1$  and  $R_2$  data in Figures 3 and 4 to the  $R_1$  and  $R_2$  values of control cell pellets ( $0.47$  and  $30.4 \text{ s}^{-1}$ , respectively) lead to estimated residual Gd concentrations in the cell pellets as high as  $1.4 \text{ mM}$  in both cases at which both the liposomal  $T_1$  and  $T_2$  shortening effects would be completely silenced. Obviously, the present data do not provide evidence that such extrapolation is justified, as the cells have not been monitored over a sufficiently long time period. However, our data do suggest that the appreciably high levels of Gd that still were associated with the cells at the 5-day time point both have a very low effective  $r_1$  and  $r_2$ .

Next we will consider the long-term fate of the Gd-chelate used in this study in the light of its thermodynamic and kinetic stability. The issue here is that both free  $\text{Gd}^{3+}$  and free chelate are toxic to cells. In addition, release of  $\text{Gd}^{3+}$ -ions from the chelate might lead to considerable changes in its relaxivity properties.

Gd-containing chelates preferably should both have a high thermodynamic and kinetic stability. Thermodynamic stability is an index of the intrinsic binding affinity of the  $\text{Gd}^{3+}$ -ion for the chelate, while kinetic stability is a measure of the true stability of the complex under more relevant conditions, such as the presence of competing metal ions in combination with phosphate and other anions (for recent comprehensive reviews see Refs. [11] and [12]). Macrocyclic chelates (such as Gd-DOTA) have a much higher thermodynamic and kinetic stability than the linear chelates (like Gd-DTPA). Among the clinically used linear chelates, Gd-DTPA-BMA (also known as Gadodiamide, or Omniscan) has the lowest thermodynamic and kinetic stability [12]. Gd-DTPA-BMA is particularly relevant as the molecular structure of its Gd-DTPA complex is very much alike that of the chelating moiety of the lipid-based Gd-DTPA species we used in the present study. Obviously, the physicochemical properties of the Gd-DTPA-BMA are otherwise very different from those of the lipidic Gd-compound. When dissolved in buffer containing  $\text{Zn}^{2+}$  and phosphate, the  $R_1$  of a suspension of liposomes containing Gd-DTPA-BSA was found to rapidly decrease [13]. This observation was explained to be due to the  $\text{Zn}^{2+}$ -induced release of  $\text{Gd}^{3+}$  from the chelate, followed by formation of  $\text{Gd}^{3+}$ -phosphate precipitates in which the paramagnetic ion can no longer exert its  $T_1$  shortening effect [14]. The above transmetalation in the presence of phosphate anions has also been proposed as a likely mechanism underlying nephrogenic systemic fibrosis (NSF), a severe disorder that is predominantly associated with the use of Gd-DTPA-BMA in patients with end-stage renal disease [12]. Severe renal disease is often accompanied by elevated serum levels of phosphate [15]. Thakral and Abraham [16] have recently studied skin biopsies of NSF patients and often found Gd to be associated with phosphate and calcium. Considering the above, it is plausible that (partial) release of  $\text{Gd}^{3+}$  from the DTPA chelate occurred in the intracellular compartments over a period of 5 days. Part of the endocytotic pathway involves compartments with a low pH around 4.7 [17], a condition known to promote  $\text{Gd}^{3+}$  release [18]. The reported  $r_1$  silencing of residual  $\text{Gd}^{3+}$  might be due to subsequent electrostatic interaction and precipitation with anions, such as phosphate. The origin of the  $r_2$  silencing that we also seem to observe is less obvious. It is feasible, however, that the Gd-containing structures reach such dimensions at some stage that they enter the static dephasing regime in terms of  $T_2$  relaxation. In this regime, the size of the relaxing structures greatly exceeds the diffusion path lengths of the water protons. In case of spin-echo based measurements of  $T_2$  (as we used here), this implies that the contrast agent does not contribute significantly to  $T_2$  relaxation, because of the refocusing effect of the  $180^\circ$  RF-pulse. In line with our observations, Anderson *et al.* [19] found that high-density endosomal labeling of mesenchymal stem cells with Gd-fullerenol, a high-relaxivity nanoparticle in which the  $\text{Gd}^{3+}$ -ion is

entrapped in a cage-like structure, also led to minor  $T_2$ - and  $T_2^*$ -shortening effects.

It is important to note that we have no indications of any toxicity of the paramagnetic Gd-DTPA-BSA agent, which was used in our study. However, no specific measurements were done to exclude any such effect. Furthermore, our studies also involved a relatively short time period. Modo and co-workers [8] have recently reported a chronic one-year *in vivo* follow-up of transplanted neural stem cells, labeled with a Gd-DTPA-based low-molecular weight bimodal MRI/fluorescent contrast agent. Note that Gd-DTPA is a linear chelate with intermediate thermodynamic and kinetic stability. Despite of the fact that there were no obvious signs of cell toxicity by the agent, the therapeutic efficacy of the Gd-labeled cells was negligible, whereas non-labeled stem cells led to a reduction of infarct size in a rat model of ischemic stroke. This points to a gradual degradation of the contrast agent inside the cells.

In conclusion, pre-labeling of cultured endothelial cells with paramagnetic liposomes, followed by incubation in liposome-free medium, led to dynamic changes in the effective  $T_1$  and  $T_2$  relaxivities of the remaining cell-associated contrast material. With time, the effective relaxivities decreased, which is possibly related with the release of Gd from the diamide-based chelate and gradual sequestration in a MR quiescent state. In order to reduce the risk of adverse effects induced by Gd release from the chelate, we have recently introduced a Gd-DOTA-based lipidic contrast agent that is immune to transmetallation under challenging *in vitro* conditions [13] and therefore also less likely to cause adverse effects when exposed to physiologically relevant conditions. Gd-DOTA has the highest stability of all clinically approved paramagnetic contrast agents.

**Acknowledgements**

The authors thank Dr. Jean-Marc Idée (Guerbet) for insightful discussions and critical reading of the manuscript.

## Literature

1. Mulder, W.J., G.J. Strijkers, G.A. van Tilborg, *et al.*, *NMR Biomed*, 2006. **19**(1): p. 142-164.
2. Mulder, W.J., G.J. Strijkers, G.A. van Tilborg, *et al.*, *Acc Chem Res*, 2009. **42**(7): p. 904-914.
3. Strijkers, G.J., W.J.M. Mulder, R.B. van Heeswijk, *et al.*, *Magnetic Resonance Materials in Physics, Biology and Medicine*, 2005. **18**(4): p. 186-192.
4. Rogers, W.J., C.H. Meyer, C.M. Kramer, *Nat Clin Pract Cardiovasc Med*, 2006. **3**(10): p. 554.
5. Shyu, W.C., C.P. Chen, S.Z. Lin, *et al.*, *Stroke*, 2007. **38**(2): p. 367-374.
6. Modo, M., K. Mellodew, D. Cash, *et al.*, *Neuroimage*, 2004. **21**(1): p. 311-317.
7. Brekke, C., S.C. Williams, J. Price, *et al.*, *Neuroimage*, 2007. **37**(3): p. 769-782.
8. Modo, M., J.S. Beech, T.J. Meade, *et al.*, *Neuroimage*, 2009. **47 Suppl 2**: p. T133-142.
9. Mulder, W.J., G.J. Strijkers, A.W. Griffioen, *et al.*, *Bioconjug Chem*, 2004. **15**(4): p. 799-806.
10. Rouser, G., S. Fkeischer, A. Yamamoto, *Lipids*, 1970. **5**(5): p. 494-496.
11. Idee, J.M., M. Port, C. Robic, *et al.*, *J Magn Reson Imaging*, 2009. **30**(6): p. 1249-1258.
12. Idee, J.M., M. Port, A. Dencausse, *et al.*, *Radiol Clin North Am*, 2009. **47**(5): p. 855-869, vii.
13. Hak, S., H.M. Sanders, P. Agrawal, *et al.*, *Eur J Pharm Biopharm*, 2009. **72**(2): p. 397-404.
14. Laurent, S., L.V. Elst, F. Copoix, *et al.*, *Invest Radiol*, 2001. **36**(2): p. 115-122.
15. Frenzel, T., P. Lengsfeld, H. Schirmer, *et al.*, *Invest Radiol*, 2008. **43**(12): p. 817-828.
16. Thakral, C., J.L. Abraham, *J Cutan Pathol*, 2009. **36**(12): p. 1244-1254.
17. Ohkuma, S., B. Poole, *Proc Natl Acad Sci U S A*, 1978. **75**(7): p. 3327-3331.
18. Wedeking, P., C.H. Sotak, J. Telser, *et al.*, *Magn Reson Imaging*, 1992. **10**(1): p. 97-108.
19. Anderson, S.A., K.K. Lee, J.A. Frank, *Invest Radiol*, 2006. **41**(3): p. 332-338.

## Chapter **5**

### **Influence of cell-internalization on relaxometric, optical and compositional properties of targeted paramagnetic quantum dot micelles**

**Based on:**

*Influence of cell-internalization on relaxometric, optical and compositional properties of targeted paramagnetic quantum dot micelles*

M.B. Kok, L.W.E. Starmans, H.M.H.F. Sanders, Y. Zhao, C. de Mello Donegá, A. Meijerink, W.J.M. Mulder, H. Gröll, G.J. Strijkers, K. Nicolay

In preparation

**Abstract**

Quantum dot micelles (pQDs) with a paramagnetic coating are promising nanoparticles for bimodal molecular imaging. Their bright fluorescence allows for optical detection, while their Gd-payload enables visualization with contrast-enhanced MRI. A popular approach in molecular MRI is the targeting of abundantly expressed cell surface receptors. Ligand-receptor binding often results in cell internalization of the targeted contrast agent. The interpretation of molecular imaging with pQDs therefore requires knowledge on the consequences of cellular internalization for their relaxometric, optical and compositional properties. To study these, Cd-containing core-shell-shell QDs were coated with a monolayer of lipids, comprising 50 mol% of a Gd-containing lipid, and incubated with endothelial cells (HUVECs) for up to 24 hr.  $\alpha_v\beta_3$ -integrin specific (RGD) and non-targeted (NT) pQDs were compared. pQDs uptake was monitored using fluorescence microscopy, FACS, ICP-MS, relaxometry and MRI. Cell-associated pQDs showed no concentration- or time-dependent changes in relaxivities and fluorescent properties, implying that the Gd and Cd uptake by HUVECs can be quantified using relaxometric and optical measurements, respectively. However, the Gd-to-Cd molar ratio in pellets of pQD-incubated cells was consistently higher than the Gd-to-Cd molar ratio of the pQDs as prepared. It is proposed that this increase in Gd-to-Cd molar ratio was due to non-specific lipid-transfer between the pQDs and the cellular membranes. These findings show that in case of contrast agents that are (partially) formed by non-covalent interactions, biological environments may complicate the imaging read-out of the contrast agent due to a (partial) loss of co-localization of the different imaging labels.

## Introduction

Molecular imaging shows great potential for *in vivo* visualization of the molecular events related to diseases, such as atherosclerosis and cancer [1]. This information could be used to characterize and diagnose disease, as well as to follow the molecular responses in pathological tissues after treatment. Both MRI and optical imaging have several attractive features which have driven the development of targeted molecular imaging probes for these modalities. MRI has the ability to produce high-resolution images with enormous anatomical detail. Paramagnetic Gd-based contrast agents, which generate signal enhancement on T<sub>1</sub>-weighted sequences, are the predominant clinically used class of MRI contrast agents [2] and are also of great interest for molecular MR imaging purposes. The main drawback of molecular MR imaging is the intrinsic low sensitivity of MRI for the detection of contrast agent, especially since most molecular markers are only expressed in relatively low levels [3]. To solve this issue, amplification strategies for Gd-based molecular MRI are required. A suitable amplification step is the use of nanoparticles with a high payload of Gd, for example using targeted paramagnetic lipid-based colloidal aggregates such as liposomes, micelles and micro-emulsions [4, 5].

An exciting class of bimodal, high Gd-payload lipid-based MRI and optical contrast agents is the paramagnetic quantum dot micelles (pQDs) [6, 7]. These nanoparticles consist of a highly fluorescent quantum dot core with a pegylated and paramagnetic lipid coating which makes the pQDs water soluble and detectable by MRI, fluorescence microscopy and other optical imaging methods. Quantum dots (QDs) are semiconductor nanocrystals, with diameters of approximately 2-10 nm, and possess superb optical properties [8, 9]. In comparison with fluorescent dyes and proteins, QDs are about 10-100 times brighter, 100-1000 times more resistant against photobleaching and display narrower emission spectra [10]. In addition, the QD emission wavelengths can be tuned from the ultraviolet to the mid-infrared [11, 12]. These optical properties can be exploited for *ex vivo* validation and *in vivo* intra-vital microscopy [7]. In addition, near infrared QDs can also be applied for *in vivo* optical imaging [7, 13, 14]. Another exciting feature of QDs for molecular imaging purposes is the ability to use QDs with different emission wavelengths simultaneously, which enables the imaging of several molecular targets at the same time. pQDs are promising nanoparticles for bimodal molecular imaging purposes, as their excellent optical properties allow for example *in vivo* whole-body hotspot imaging in small animal models, while the high Gd-payload allows for high-resolution contrast-enhanced MRI [7].



In molecular imaging experiments, contrast agents are frequently incubated with cultured cells or injected intravenously in living organisms. These biological environments may change the properties of the contrast agent. For instance, the low molecular-weight MRI contrast agent Vasovist™ has been designed to bind *in vivo* to serum albumin and this increases the relaxivity and blood-circulation life-time of the contrast agent tremendously [15, 16]. For the analysis of molecular imaging experiments using bimodal contrast agents, it is important to know whether both imaging labels still colocalize after introducing the contrast agent into a biological environment. pQDs have a QD-core as fluorescent label, whereas the MR-label is situated in the lipid coating, which is associated with the QD-core via non-covalent, hydrophobic interactions. It is not unlikely that the hydrophobic interactions which keep the MR-labeled lipids around the QD-core are seriously challenged by other sorts of molecules or interactions *in vivo* and *in vitro*, which could affect the level of co-localization between the fluorescent- and MR-labels. Furthermore, contrast agents are frequently equipped with ligands, which specifically bind to a certain receptor for molecular imaging purposes. The interaction between the ligand and membrane-receptor frequently results in cellular internalization of the contrast agent, with receptor mediated endocytosis being the most likely route for this process [17]. During receptor mediated endocytosis, most of the targeted contrast agent becomes entrapped in endosomal vesicles within the cell. Previously, several research groups have reported that this entrapment of Gd-based contrast agent into endosomes strongly decreases the effective longitudinal relaxivity, which may hamper the detectability of the contrast agent using T<sub>1</sub>-weighted MRI (Chapter 2 and refs. [18-20]). Moreover, the optical properties of pQDs may also change due to cellular-internalization, as for instance lysosomal degradation may diminish the optical properties of the fluorescent QD-cores.

In order to exploit pQDs for receptor imaging purposes, it is therefore important to study the influence of cellular internalization on the relaxometric, optical and compositional properties of paramagnetic quantum dots. To this aim, pQDs with a size of approximately 46 nm were targeted towards the  $\alpha_v\beta_3$ -integrin by conjugating a cyclic RGD-peptide to the lipid monolayer. The  $\alpha_v\beta_3$ -integrin membrane-receptor is a frequently used target for molecular imaging of angiogenesis, as this receptor is significantly up-regulated on activated tumor endothelium and on certain invasive tumor cells, but not on quiescent endothelium and in normal tissues [21]. pQDs without the cyclic RGD-peptide served as control system for nonspecific uptake. HUVECs were used as an *in vitro* model system that abundantly expresses  $\alpha_v\beta_3$ -integrin [22]. Inductively coupled plasma mass spectrometry (ICP-MS) was used to determine the

gadolinium (Gd) and cadmium (Cd) content in HUVECs.  $T_1$ - and  $T_2$ -measurements were performed to determine the longitudinal and transversal relaxivity of cell-internalized CA and fluorescence-activated cell sorting (FACS) measurements were carried out to assess the fluorescent intensity per cell. Confocal laser scanning microscopy (CLSM) was performed to determine the cellular location of the CA.

## Materials and methods

### Materials

Gd-diethylenetriaminepentaacetic acid-bis(stearylamide) (Gd-DTPA-BSA) was purchased from Gateway Chemical Technology (St. Louis, MO, USA). 1,2-distearoyl-*sn*-glycero-3-phosphoethanolamine-N-[methoxy(polyethyleneglycol)-2000] (PEG<sub>2000</sub>-DSPE) was acquired from Lipoid GmbH (Ludwigshafen, Germany) and 1,2-diastearoyl-*sn*-glycero-3-phosphoethanolamine-N-[maleimide(polyethyleneglycol)-2000] (Mal-PEG<sub>2000</sub>-DSPE) was obtained from Avanti Polar Lipids (Alabaster, AL, USA). Human umbilical vein derived endothelial cells (HUVECs) and endothelial growth medium-2 (EGM-2) were obtained from Lonza Bioscience (Basel, Switzerland). Monoclonal mouse anti-human CD31 antibody was purchased from Dako (Glostrup, Denmark). Alexa Fluor 488 conjugated goat anti-mouse secondary antibody and DAPI (4',6-diamidino-2-phenylidole-dihydrochloride) were purchased from Invitrogen (Eugene, OR, USA). Sulphur (99.999%) and selenium powder were obtained from Alfa Aesar (Karlsruhe, Germany). Acetone (p.a), chloroform (p.a), cadmium oxide (>99%) and zinc oxide (>99%) were purchased from Merck (Darmstadt, Germany). Cyclic RGD, c(RGDf(-S-acetylthioacetyl)K), was synthesized by Ansynth Service BV (Roosendaal, The Netherlands). All other chemicals were obtained from Sigma (St. Louis, MO, USA).

### Synthesis of core-shell-shell quantum dots (CSS-QDs)

CdSe (core) QDs were synthesized using an organometallic synthesis route, as described by de Mello Donegá *et al.* [23]. The CdSe QDs were coated with 7 monolayers of inorganic shells (2xCdS, 3x Cd<sub>0.5</sub>Zn<sub>0.5</sub>S, 2x ZnS) by a SILAR procedure [24]. In short: the shell growth was performed by adding precalculated amounts of a 0.1 M precursor (Cd oleate, CdZn oleate, and Zn oleate) to the CdSe (core) QDs dispersion in a mixture of octadecene (ODE) and octadecylamine (ODA) at 235 °C. Each monolayer was allowed to grow for at least 20 min. The core-shell-shell CSS-QDs were purified two times by precipitation in a chloroform/acetone mixture followed by redispersion in chloroform obtaining a concentration of 1.7 nmol CSS-QDs cores per mL.

### Lipid coating of the core-shell-shell quantum dots (CSS-QDs)

Methanol was added to the CSS-QDs in order to reach a chloroform/methanol 20/1 (v/v) dispersion and subsequently Gd-DTPA-BSA, PEG<sub>2000</sub>-DSPE and Mal-PEG<sub>2000</sub>-DSPE were added in a molar ratio of 0.5/0.35/0.15. A 25-fold excess of lipids required to entirely cover the surface of all CSS-QDs with a lipid monolayer was used. This suspension was added dropwise to stirred, deionized water at 80 °C. Upon evaporation of the organic solvents, the inorganic CSS-QDs were encapsulated in the core of phospholipid micelles, creating

paramagnetic quantum dot micelles (pQDs). Half of the obtained suspension was modified with a cyclic RGD-peptide (100 mg/mmol total lipid) to target the  $\alpha_v\beta_3$  integrin. The cyclic RGD was deacetylated at room temperature for 1 hr using a hydroxylamine containing buffer and subsequently coupled to the distal end of Mal-PEG<sub>2000</sub>-DSPE overnight at 4 °C. Next, the phospholipid micelles without nanocrystals were removed by ultracentrifugation, exploiting the high density of the QD cores using a modified Havel's ultracentrifugation separation method [25]. In short, the QD-dispersion was put on top of a 1.27 g/mL KBr solution, which was gently deposited on top of an 1.37 g/mL KBr solution. Next, this three-layer solution was ultracentrifuged at 100,000 x g at room temperature for 1 hr using an Optima™ L-90K ultracentrifuge equipped with a type 70.1 TI rotor (Beckman Coulter, Fullerton, CA, USA). After ultracentrifugation, the top-layer containing the lipidic micelles without a nanocrystal core was carefully aspirated and discarded. Next, the second layer containing the pQDs was extracted gently while preventing the redispersion of the formed pellet. Subsequently, the extracted pQDs were prepared for *in vitro* application by changing the buffer to HEPES buffered saline (HBS) (10 mM HEPES, 137 mM NaCl, pH 7.4) using PD10 desalting columns (GE Healthcare, Fairfield, CT).

#### Characterization of paramagnetic quantum dot micelles (pQDs)

Cryogenic transmission electron microscopy (cryo-TEM) was executed to estimate the mean size of the crystalline quantum dot core and to study the monodispersity of the pQDs and the presence of other lipidic structures, using a FEI Tecnai 20, type Sphera TEM instrument operating at 200 kV with a Gatan cryoholder at approximately -170 °C. Sample vitrification was carried out using an automated vitrification robot (FEI Vitrobot Mark III). The mean size of the crystalline QD core was calculated using ImageJ software (NIH, Bethesda, MD, USA). The hydrodynamic size of the pQDs in HBS was determined with dynamic light scattering (DLS) on a Zetasizer Nano-S (Malvern, UK) using intensity-weighted particle size distribution. Fluorescence emission and excitation spectra of the pQDs in HBS (pH 7.4) placed in a quartz cuvette were recorded on a Lambda 900 spectrophotometer (Perkin Elmer, Waltham, MA) with a scan speed of 50 nm/min. For the pQDs-excitation spectra, an emission wavelength of 625 nm was used as read-out with both an excitation and emission slit of 4 nm, whereas the pQDs were excited at 400 nm to assess the emission spectra with both an excitation and emission slit of 5 nm. Both the longitudinal and transverse relaxivity ( $\text{mM}^{-1}\text{s}^{-1}$ ) were determined at room temperature and 6.3 T by fitting  $R_1$  ( $1/T_1$ ) and  $R_2$  ( $1/T_2$ ) values as function of the gadolinium concentration of the pQDs in HBS, using the least squares method. The  $R_1$  and  $R_2$  were measured as described below in the section on magnetic

resonance imaging of cell pellets. The gadolinium and cadmium concentrations were determined using ICP-MS (Philips Research, Eindhoven, The Netherlands).

#### Cell culture

HUVECs were used in all experiments. Cells were stored in liquid nitrogen upon arrival. Before use, the cells were swiftly thawed and divided over two T75 TCPS flasks (Thermo Fisher Scientific, MA). HUVECs were cultured in a humidified incubator at 37 °C with 5% CO<sub>2</sub> and the EGM-2 medium was replaced every 2-3 days. HUVECs were subcultured at 80-90% confluency according to procedures provided by Lonza Bioscience (Basel, Switzerland).

#### Experimental setup

The pQD-HUVEC incubation experiments were performed on cells grown on both gelatin-coated coverslips placed in 6-well plates and in gelatin-coated T75 TCPS culture flasks. HUVECS of passage 3 were used for all experiments at 80-90% confluency and all measurements were carried out in triplicate for each incubation time and both types of pQDs. To initiate the incubation experiment, medium was substituted by either RGD-pQD or NT-pQD containing medium at a concentration of 0.35 µmol total lipid per mL medium. 4.5 mL of pQD containing medium was added to the T75 gelatin-coated TCPS flasks, and 1.5 mL medium was added to the gelatin-coated coverslips. The incubation times with pQD containing medium varied between 0 and 24 hr. Following incubation, the medium was removed from the HUVECs and 50 µL of the medium was taken for ICP-MS analysis to determine the cadmium and gadolinium content of the medium. Next, HUVECs were washed three times with 5 mL HBS to remove nonadherent pQDs and subsequently the cells grown on coverslips were fixed using 4% PFA in phosphate buffered saline (PBS) (pH 7.4) for 15 min at room temperature. Cells in culture flasks were detached using 2 mL 0.2% trypsin 1 mM EDTA (Lonza Bioscience, Switzerland) per flask and following detachment, the trypsin was neutralized using 4 mL of trypsin neutralizing solution (Lonza Bioscience, Switzerland). Cells were spun down at 220 g for 5 min, the supernatant was removed and subsequently the cell pellet was resuspended in 250 µL of 4% PFA in PBS (pH 7.4) and transferred to a 300 µL Eppendorf cup. Next, the cells were gently spun down at 20 g for 5 min to create a loosely-packed cell pellet.

Before spinning down the cells, a minute fraction of the cells was taken for FACS analysis in order to measure the quantum dot fluorescence per cell using a FACSCanto II (BD, Franklin Lakes, NJ) with a 405 nm excitation laser and a 502 nm long pass filter. To visualize the pQDs in the cell pellet, photographs were taken under 366 nm UV light illumination using a 2 x 8 Watt 366 nm

UV Lamp (CAMAG, Muttenz, Switzerland) and a digital camera (Cannon Power Shot A710SI). The cell pellets were stored in the dark at 4 °C.

#### Magnetic resonance imaging of cell pellets

The  $T_1$  and  $T_2$  relaxation times and the volume of the pellets were measured at room temperature using a 6.3 T horizontal bore animal MR scanner (Bruker, Ettlingen, Germany). A 3 cm diameter send-and-receive quadrature-driven bird-cage coil (Rapid Biomedical, Rimpar, Germany) was utilized to measure longitudinal and transverse relaxation times. The loosely-packed cell pellet containing Eppendorf cups were placed in a custom made holder for 4 cups that was filled with water to facilitate shimming.  $T_1$  was measured using an inversion recovery segmented fast low-angle shot (FLASH) sequence with an echo time (TE) of 1.5 ms, a repetition time (TR) of 3.0 ms, a flip angle of 15° and an inversion time ranging from 67.5 to 4807.5 ms in 80 steps. Overall repetition time was 20 s. The field of view (FOV) was 3 x 2.18 cm<sup>2</sup>, using a matrix size of 128 x 128, a slice thickness of 0.75 mm and 2 averages.  $T_2$  was measured utilizing a multi-slice multi-echo sequence with TE ranging between 9 and 288 ms in 32 steps and a TR of 1000 ms. FOV was 3 x 2.18 cm<sup>2</sup>, slice thickness was 0.75 mm using a matrix size of 128 x 128. Number of averages was 4.  $T_1$ - and  $T_2$ -maps were calculated from the images using Mathematica (Wolfram Research Inc, Champaign, IL).  $T_1$  and  $T_2$  were calculated from mean values within a region of interest (ROI) in the pellets.  $T_1$ -weighted images were measured using a multi-slice spin-echo sequence with TE = 10.3 ms and TR = 500 ms. FOV was 3 x 3 cm<sup>2</sup>, slice thickness was 0.75 mm using a matrix size of 256 x 192. Number of averages was 1. The volume of the cell pellet was determined for each sample separately with a 0.7 cm diameter solenoid coil using a three-dimensional FLASH sequence with TE = 3.2, TR either 10 or 15 ms and a flip angle of 30°. FOV was 1.6 x 1.6 x 1.6 cm<sup>3</sup>, matrix size was 128 x 128 x 128. Number of averages was 1. Pellet volume was determined by manually setting threshold values to select voxels within the pellet. The remaining voxels were multiplied by the voxel volume to obtain the total volume of the pellet. The concentration of gadolinium and cadmium in each cell pellet was determined by dividing the gadolinium and cadmium content as determined by ICP-MS by the pellet volume.

#### Immunofluorescence microscopy

The coverslips with fixed pQDs-incubated HUVECs were stained at room temperature using a mouse anti-human CD31 antibody to visualize the cellular membrane. The cells were rinsed for 5 min with PBS and subsequently incubated for 60 min with primary mouse anti-human CD31 antibody in a 1:40 dilution in PBS. Next, the cells were washed 3 x 5 min with PBS followed by

30 min of incubation with a secondary Alexa Fluor 488 goat anti-mouse IgG antibody (1:200 dilution in PBS). Then the cells were washed 3 x 5 min with PBS and the cell nuclei were stained for 5 min with DAPI. Subsequently the cells were rinsed 3 x 5 min with PBS and mounted on a microscopy slide using Mowiol Mounting Medium.

Confocal fluorescence images were recorded at room temperature on a Zeiss LSM 510 META system using a Plan-Apochromat<sup>®</sup> 63X/1.4 NA oil-immersion objective and photomultiplier tubes (Hamamatsu R6357). All experiments were combined in multitrack mode and acquired confocally. The crystalline quantum dot core and Alexa Fluor 488 were excited using the 458 and 488 nm line of a HeNe laser, respectively. The emission of the quantum dots was analyzed using the Zeiss Meta system in a wavelength range of 619-672 nm, after spectral filtering with an NFT 545 nm beamsplitter. The Alexa Fluor 488 emission was recorded after spectral filtering with an NFT 490-nm beamsplitter followed by a 500-550 nm band pass filter. DAPI staining of nuclei was visualized by two-photon excitation fluorescence microscopy on the same Zeiss LSM 510 system. Excitation at 780 nm was achieved by using a pulsed Ti:Sapphire laser (Chameleon<sup>™</sup>; Coherent, Santa Clara, CA) and fluorescence emission was detected with a 395-465 nm band pass filter.

## Results and Discussion

### Paramagnetic quantum dot micelle characterization

To study the consequences of cell-internalization on the relaxometric, optical and compositional properties of paramagnetic quantum dot micelles (pQDs), highly luminescent CdSe/CdS/Cd<sub>0.5</sub>Zn<sub>0.5</sub>S/Zns core-shell-shell (CSS) QDs were synthesized. Coating of hydrophobic CSS-QDs with pegylated and paramagnetic lipids resulted in highly fluorescent pQDs. Half of these pQDs were prepared for targeting towards  $\alpha_v\beta_3$ -integrin by coupling of cyclic RGD-peptides, while the rest of the pQD preparation was used as a non-targeted control. In the remainder of this study, we refer to paramagnetic quantum dot micelles that were conjugated to RGD to target the  $\alpha_v\beta_3$ -integrin as RGD-pQDs. Non-targeted pQDs without a targeting ligand will be referred to as NT-pQDs.

The hydrodynamic diameter of the pQDs in HEPES buffered saline (HBS) at pH 7.4 was determined using dynamic light scattering (DLS). Figure 1A shows the size distribution obtained from an intensity-weighted analysis of the time correlation function measured with DLS. One dominant peak corresponding to a diameter of 46 nm was seen for both types of pQDs. Minor peaks at larger particle sizes were indicative of a small fraction of aggregates. Cryo-TEM was performed to resolve the crystalline core size of the pQDs and to confirm the monodispersity of the QD-cores. High-resolution cryo-TEM images showed that most of the pQDs contained one quantum dot core, whereas only a minute fraction of the nanoparticles was organized as aggregates containing several CSS-QD cores (Figure 1B). No other lipidic structures, such as liposomes and micelles, were observed. The diameters of the crystalline CSS-QD cores, as deduced from cryo-TEM, were  $7 \pm 2$  nm for both RGD- and NT-pQDs. Figure 1C displays a typical example of the absorption and emission spectra of the pQDs dispersed in HBS (pH 7.4). A broad absorption spectrum that is characteristic for QDs and a narrow emission spectrum with a maximum at 625 nm, were observed. ICP-MS was used to determine the Gd and Cd content of the pQDs as prepared. Figure 1C shows that pQDs could be excited effectively within a broad wavelength range. ICP-MS was used to determine the Gd and Cd content of the pQDs as prepared. The Gd/Cd molar ratio was  $0.36 \pm 0.01$  and  $0.38 \pm 0.01$  for the RGD- and NT-pQDs, respectively. Longitudinal and transverse relaxivity of the pQDs in HBS pH 7.4 were determined at 6.3 T and room temperature. Measurements showed  $r_1 = 5.2 \pm 0.1 \text{ mM}^{-1}\text{s}^{-1}$  and  $5.7 \pm 0.3 \text{ mM}^{-1}\text{s}^{-1}$ , and  $r_2 = 26.1 \pm 0.9 \text{ mM}^{-1}\text{s}^{-1}$  and  $32.4 \pm 2.0 \text{ mM}^{-1}\text{s}^{-1}$  for RGD- and NT-pQDs, respectively.



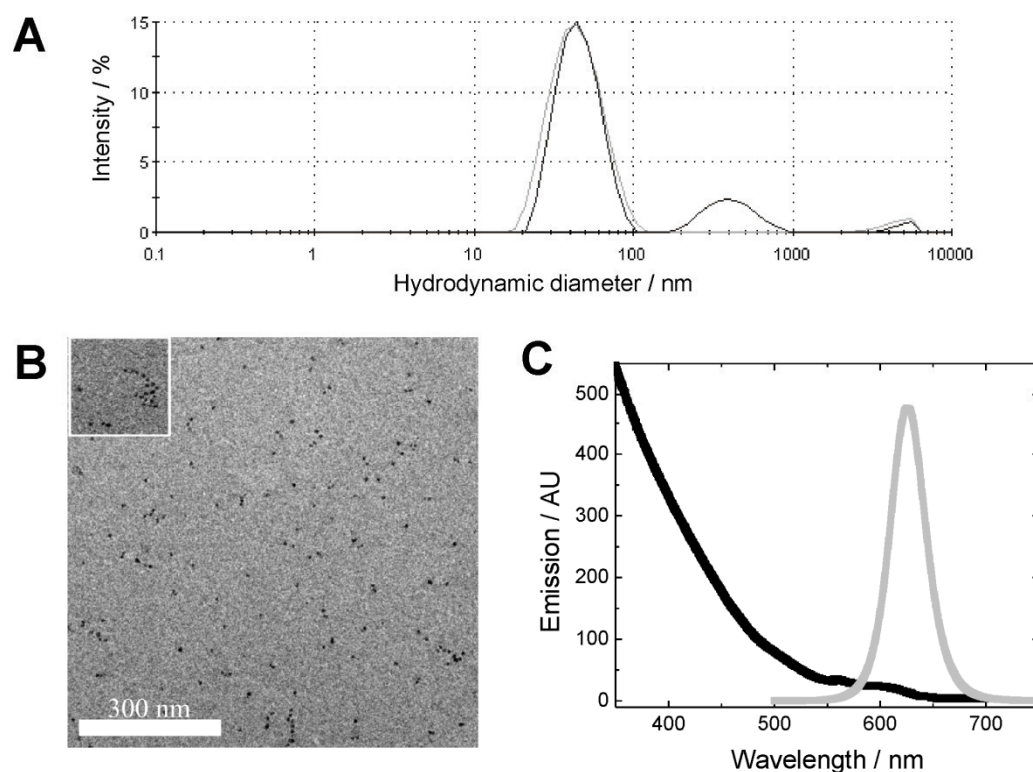


**Figure 1, Characterization of the pQDs preparations. (A) Intensity-weighted DLS-spectrum of RGD-pQDs (gray) and NT-pQDs (black). (B) Typical cryo-TEM image of RGD-pQDs at 19,000x magnification. The crystalline CSS-QD cores of the pQDs are visualized as black dots. Occasionally, aggregates were observed and a typical example of such an aggregate is shown within the inset (upper left corner). (C) Excitation (black) and emission spectra (gray) of the RGD-pQDs dispersed in HBS.**

#### Incubation of paramagnetic quantum dot micelles with HUVECs

CLSM was performed to study the internalization of fluorescent crystalline QD-cores by endothelial cells. For this purpose, HUVECs were grown on gelatin-coated coverslips and incubated with either RGD- or NT-pQDs up to 24 hr. During incubation, morphology of the cells was tracked using a bright-field microscope. The morphology of HUVECs changed from a smooth-globular towards a star-shaped structure, especially for the RGD-pQDs incubated cells in case of long incubation times (16-24 hr). This could indicate that incubation with the pQDs caused a mild toxic effect. However, no obvious increase in cell death was observed. After incubation, the medium containing the non cell-associated pQDs was removed. Subsequently, the cells were washed three times and fixed with 4% paraformaldehyde (PFA). Next, the cells were stained for the CD31 membrane-receptor to visualize the HUVECs and the cell nuclei were stained using DAPI. Figure 2 shows confocal images of HUVECs incubated with either

RGD- or NT-pQDs. Both RGD- and NT-pQDs accumulated mainly in the perinuclear region in spherical 0.5-2  $\mu\text{m}$  diameter vesicles. The amount of pQD-fluorescence increased with increasing incubation time during the initial 16 hr. Furthermore, the RGD-pQDs clearly showed more intense fluorescence signal than NT-pQDs in HUVECs after 16 hr of HUVEC incubation. However, after 16 hr the fluorescence intensity decreased again for the RGD-pQDs in the CLSM-images.

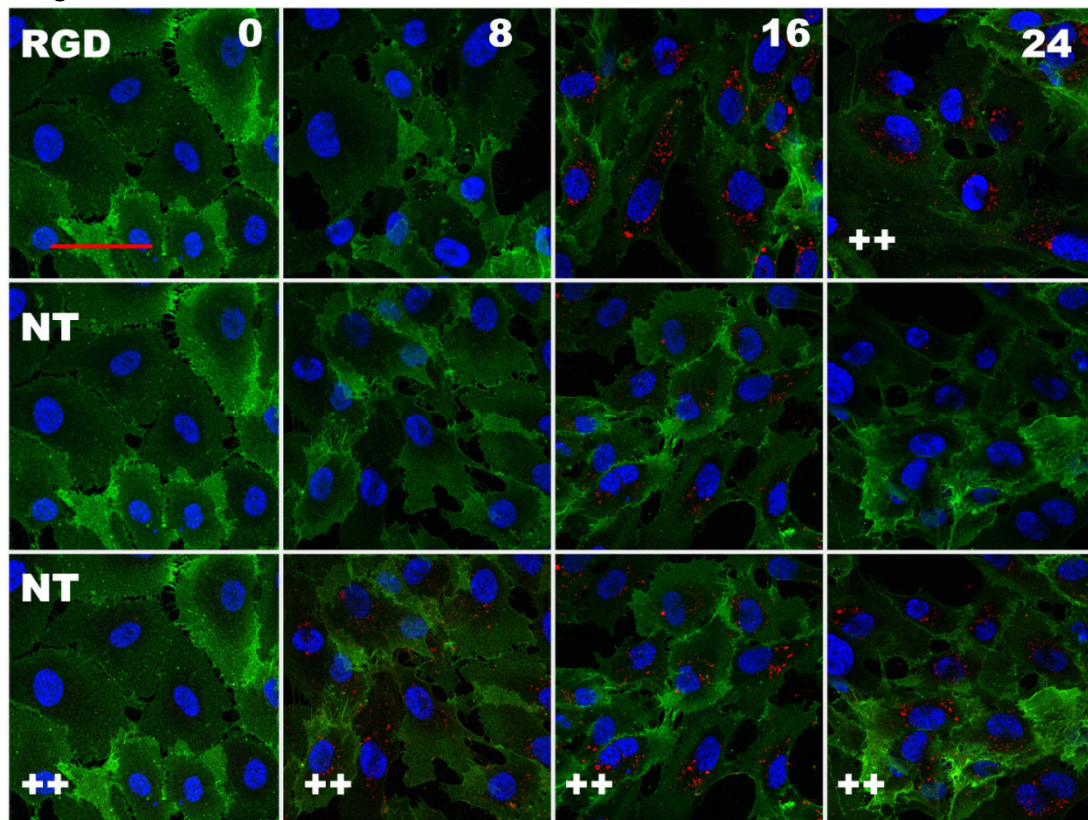


**Figure 2: CLSM images of HUVECs incubated with RGD-pQDs (RGD) and NT-pQDs (NT). Blue = DAPI; red = QD-fluorescence; green = CD31. Red scale bar = 50  $\mu\text{m}$ . The number shown in the top right corner of each column is the incubation time in hr. Note that the laser intensity for capturing the images labeled with ++ in the bottom left corner was increased in comparison to the other images.**

In order to study the properties of cell-internalized pQDs, HUVECs were cultured in TCPS cell-culture flasks and incubated either with RGD- or NT-pQDs up to 24 hr. The morphology of HUVECs changed slightly towards a more star-shaped structure during incubation, but this change was less pronounced than for the HUVECs cultured on coverslips for CLSM-analysis. Again, no obvious increase in cell death was observed. The difference in morphological changes between HUVECs cultured in culture flasks and glass coverslips could have been caused

by the small difference in coating to which the cells adhere in these two situations. After incubation, the medium containing the non-cell associated pQDs was removed and a sample of the medium was taken for ICP-MS analysis to determine the concentration of Gd and Cd in the medium. This information was used to detect potential compositional changes of non cell-associated pQDs in the medium. Subsequently the cells were washed three times, trypsinized, fixed and pelleted. Before pelleting the HUVECs, a minor fraction of the fixed cell suspension was taken for FACS analysis.

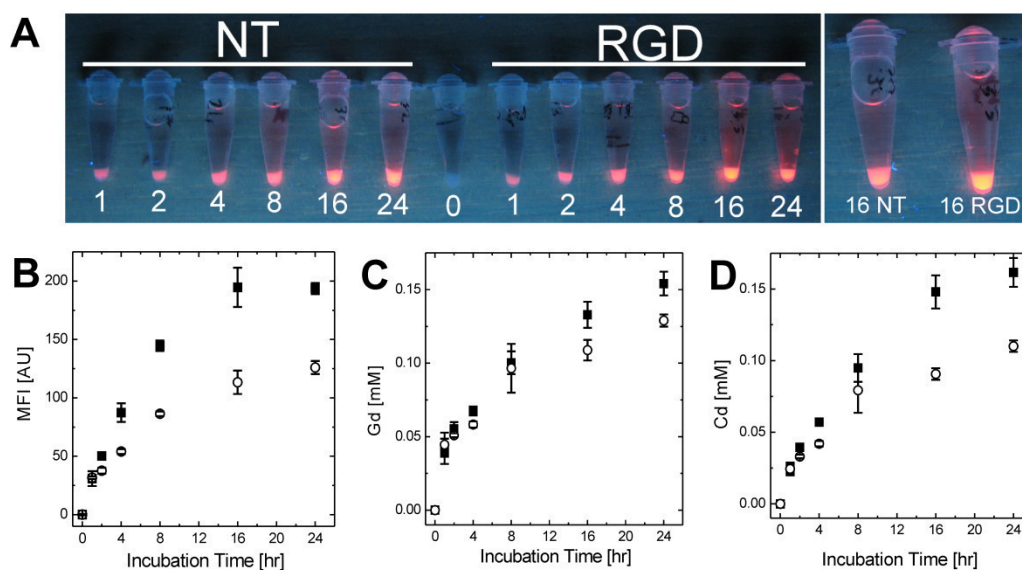


**Figure 3: Time-course of pQD-uptake by HUVECs. (A) Photograph of pellets containing cells incubated with NT-pQDs (left, 1-24 hr of incubation), RGD-pQDs (right, 1-24 hr of incubation) and control cells (middle, 0 hr of incubation) under 366 nm UV-illumination. The top right inset shows pellets of cells incubated with NT-pQDs (left) or RGD-pQDs (right) for 16 hr. (B-D) Mean fluorescence intensity per cell (B), gadolinium (C) and cadmium (D) concentrations within the cell pellets as a function of incubation time for RGD-pQDs (solid squares) and NT-pQDs (open circles). Data represent mean  $\pm$  SD (n=3).**

The uptake of the pQDs by HUVECs was qualitatively evaluated by illuminating the cell pellets with 366 nm UV-light. Figure 3A shows a photograph of the cell pellets, which, except for the non-incubated control cells, were fluorescent upon UV illumination. Longer incubation times led to a higher fluorescent signal. Furthermore, the inset on the right side of Figure 3A, illustrates that pellets with RGD-pQD incubated cells were more fluorescent than the pellets containing NT-pQDs incubated HUVECs. The uptake of the contrast agent was quantitatively assessed using FACS and ICP-MS. FACS was used to measure the pQD-fluorescence per cell and ICP-MS was performed to determine the gadolinium and cadmium content of the pelleted HUVECs. Figure 3B displays the mean

fluorescence intensity (MFI) of the pQDs per cell as a function of incubation time. A higher uptake for the RGD-pQDs was found in comparison with the NT-pQDs throughout the entire incubation experiment. A steep increase in fluorescence intensity was found during the first 8 hr for both RGD- and NT-pQDs. After 8 hr, the amount of contrast agent uptake by HUVECs leveled off. The mean gadolinium and cadmium concentrations in the cell pellets as a function of incubation time are depicted in Figure 3C and Figure 3D, respectively. A higher uptake of both gadolinium and cadmium was found for the RGD-pQDs in comparison with the NT-pQDs. Similar to the MFI, the uptake of gadolinium and cadmium appeared to level off with increasing incubation time. The difference in cadmium uptake between RGD- and NT-pQDs was more pronounced than the difference in gadolinium uptake between the two types of pQDs. After 24 hr incubation, the concentration of gadolinium in the pellets containing RGD-pQDs was 0.16 mM, whereas the concentration of gadolinium was 0.13 mM for the NT-pQDs containing cell pellets. For cadmium, the pellets containing RGD-pQDs had a concentration of 0.16 mM whereas the cadmium concentration for the cell pellets incubated with NT-pQDs was 0.11 mM. Thus, functionalization of the pQDs with the cyclic RGD-peptide led to a 20% increase in gadolinium concentration and to almost a 50% increase in cadmium concentration in HUVECs after 24 hr of incubation. Interestingly, the RGD-pQDs had also approximately a 50% higher mean fluorescent intensity per HUVEC in comparison to the NT-pQDs, as shown by FACS-analysis (Figure 3B).

The observation from the CLSM-images that the RGD-pQDs fluorescence intensity decreased after more than 16 hr of incubation was not in consensus with the FACS and Cd-content analysis, as these measurements neither showed a decrease in mean fluorescence intensity nor a decrease in cadmium concentration in cell pellets containing HUVECs incubated with RGD-pQDs for more than 16 hr. It is important to note that the HUVECs used for CLSM showed a more pronounced change in morphology during the incubation experiment than the HUVECs used for FACS-analysis and cadmium-content determination. This difference could have affected particle uptake and retention characteristics.

#### *Influence of cell-internalization on compositional properties of pQDs*

An interesting observation from the incubation-experiment was that functionalizing the pQDs with RGD led to a disparity in increase between the gadolinium and cadmium concentrations in the cell pellets. In order to provide more information about this observation, the gadolinium versus cadmium (Gd/Cd) molar ratio of the RGD- or NT-pQDs incubated HUVECs is plotted against the incubation time in Figure 4. Furthermore, also the Gd/Cd molar ratio of the medium at each incubation time point is depicted in Figure 4. The straight

line in Figure 4 represents the Gd/Cd molar ratio of the pQDs as prepared, which was 0.37. The Gd/Cd molar ratio in the medium was constant and equaled the value of the pQDs as prepared. The Gd/Cd molar ratio in the pellets with pQD-incubated HUVECs, however, was significantly higher, in particular at early time points. After 1 hr of incubation, the Gd/Cd molar ratio amounted to  $1.61 \pm 0.09$  and  $1.83 \pm 0.05$  for the RGD- and NT-pQDs incubated HUVECs, respectively. This was approximately five-fold higher than the Gd/Cd molar ratio of the pQDs as prepared. Subsequently, the Gd/Cd molar ratio of the RGD- and NT-pQDs incubated HUVECs gradually dropped towards a value of  $1.06 \pm 0.04$  and  $1.22 \pm 0.03$  for HUVECs incubated for 8 hr with RGD- and NT-pQDs, respectively. After the initial 8 hr, the Gd/Cd molar ratio stabilized at values of  $0.95 \pm 0.01$  and  $1.17 \pm 0.05$  for HUVECs incubated for 24 hr with RGD- and NT-pQDs, respectively. One possible explanation for this remarkable finding is that upon exposing the HUVECs to the pQDs, not only pQDs were internalized by HUVECs, but also non-specific lipid-transfer between the pQD-lipid coating and the cellular membrane occurred which consequently led to an increased Gd/Cd molar ratio of the HUVECs. The high initial values for the Gd/Cd ratio at short incubation times, which corresponded to low levels of cell-associated Gd and Cd (Figure 3C and 3D, respectively), suggest that immediately after exposing the HUVECs to the pQDs, a burst of lipid-transfer occurred. Subsequently, the Gd/Cd molar ratio dropped gradually to its equilibrium value, which remained significantly different from the value for the pQDs as prepared. Assuming the above lipid transfer mechanism to hold true, these findings suggest that during incubation two processes took place: (i) non-specific lipid-transfer and (ii) cell-internalization of pQDs. An important observation is that the Gd/Cd molar ratio of the RGD-pQDs incubated HUVECs was consistently lower than the Gd/Cd molar ratio of NT-pQDs incubated HUVECs throughout the entire incubation experiment. This suggests that the cellular internalization process of pQDs was relatively more pronounced than non-specific lipid-transfer for RGD-pQDs in comparison to the NT-pQDs incubated HUVECs. A plausible explanation would be that functionalizing the pQDs with the RGD-peptide increased the level of pQD cellular-internalization, thus lowering the relative contribution of non-specific lipid-transfer for RGD-pQDs in comparison to the NT-pQDs. It should be noted that these explanations are speculative and further experiments are required to gain a better understanding of the processes involved.

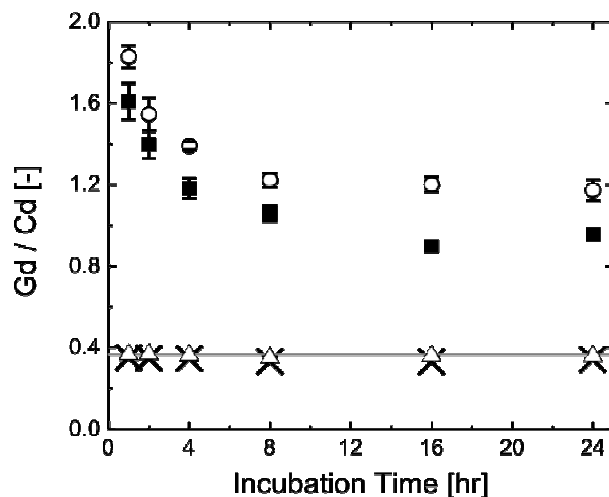


**Figure 4:** The molar ratio of cell-associated Gd and Cd versus the incubation time for HUVECs incubated with either RGD-pQDs (solid squares) or NT-pQDs (open circles) and for RGD-pQDs and NT-pQDs in the growth medium (black crosses and open triangles, respectively). The solid line represents the Gd/Cd molar ratio in HBS for both RGD- and NT-pQDs as prepared. Data represent mean  $\pm$  SD ( $n=3$ ).

### Relaxometry

The  $R_1$  and  $R_2$  relaxation rates of pelleted HUVECs were determined with MRI at 6.3 T at room temperature as function of the incubation time. Figure 5A shows the relationship between the longitudinal relaxation rate  $R_1$  and the incubation time, illustrating that the  $R_1$  increased from  $0.46 \pm 0.01 \text{ s}^{-1}$  for untreated cells to approximately  $1.02 \pm 0.04 \text{ s}^{-1}$  and  $0.97 \pm 0.01 \text{ s}^{-1}$  for HUVECs incubated for 24 hr with RGD- and NT-pQDs, respectively. Most of the  $R_1$  increase for both RGD- and NT-pQDs incubated HUVECs occurred in the first few hr: from the pre-incubation value of  $0.46 \pm 0.01 \text{ s}^{-1}$  to approximately  $0.87 \pm 0.03 \text{ s}^{-1}$  and  $0.81 \pm 0.06 \text{ s}^{-1}$  after 4 hr of RGD- and NT-pQD incubation, respectively. After these initial 4 hr of incubation, the rate of  $R_1$  increase leveled off, as the  $R_1$  increased only from  $0.8 \text{ s}^{-1}$  to approximately  $1.0 \text{ s}^{-1}$  after 24 hr for both RGD- and NT-pQDs containing cells. Although the RGD-pQDs incubated cells appeared to have higher  $R_1$  values than the NT-pQDs containing HUVECs for time points exceeding two hr of incubation, the difference was not significant for most incubation time points. The relationship between the transverse relaxation rate  $R_2$  and the incubation time is shown in Figure 5B.  $R_2$  increased from a pre-incubation value of  $31.5 \pm 0.4 \text{ s}^{-1}$  to approximately  $35.4 \pm 0.6 \text{ s}^{-1}$  and

$34.7 \pm 1.2 \text{ s}^{-1}$  for both RGD- and NT-pQDs incubated cells, respectively. It is hard to distinguish between RGD- and NT-pQDs on the basis of the transverse relaxation rate, as both RGD- and NT-pQDs showed similar values throughout the incubation-time range. The small differences in relaxation rates between pellets of HUVECs after incubation with the two types of pQDs are further illustrated by Figure 5C. Figure 5C shows typical  $T_1$ -weighted images of cell pellets not incubated with pQDs (left), and cell pellets incubated for 4 hr (middle) and 16 hr (right) with either NT-pQDs (middle) or RGD-pQDs (right). The pellet not incubated with pQDs was essentially iso-intense with medium above, whereas the pellets incubated either with NT- or RGD-pQDs were easily distinguishable from the medium as a consequence of the reduced cellular  $T_1$  caused by the pQDs. Higher signal intensity was observed for the pellets incubated with pQDs for 16 hr in comparison to the cell pellets incubated with pQDs for 4 hr. However, it was difficult to differentiate the NT- and RGD-pQDs incubated pellets, even after 16 hr of incubation, in agreement with the very similar  $R_1$  (Figure 5A) and  $R_2$  (Figure 5B) of the cell pellets.

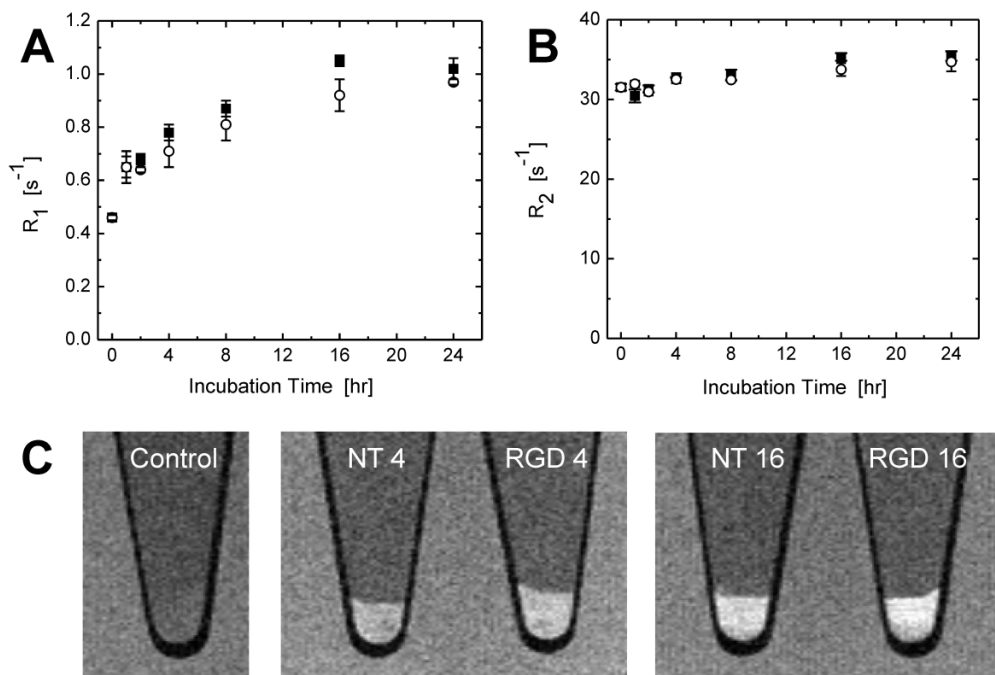


**Figure 5, Relaxometric and MRI measurements on pellets containing pQD-incubated HUVECs.  $R_1$  (A) and  $R_2$  (B) as function of time for HUVECs incubated with RGD-pQDs (solid squares) or NT-pQDs (open circles). Data represent mean  $\pm$  SD ( $n=3$ ). (C) Typical examples of  $T_1$ -weighted images of cell pellets of HUVECs not incubated with pQDs (Control), after 4 hr (middle) or 16 hr (right) of incubation with NT-pQDs (NT) or RGD-pQDs (RGD).**



*Influence of cell-internalization on relaxometric and optical properties of pQDs*

The efficacy of an MRI contrast agent is usually expressed as the relaxivity ( $r_1$  or  $r_2$ ) in  $\text{mM}^{-1}\text{s}^{-1}$ , which is the slope of the relaxation rate ( $R_1$  or  $R_2$ , respectively) as function of the contrast agent's concentration. In order to examine the effect of cell-internalization on the relaxometric efficacy of pQDs, the relaxation rates  $R_1$  and  $R_2$  of pellets of HUVECs incubated with either RGD- or NT-pQDs were plotted versus the cell-associated gadolinium concentrations (Figure 6A and 6B, respectively). The slope of the  $R_1$  versus the gadolinium concentration was determined using the least squares method and resulted in a cellular longitudinal relaxivity ( $r_1$ ) of  $4.2 \pm 0.1 \text{ mM}^{-1}\text{s}^{-1}$  and  $4.0 \pm 0.1 \text{ mM}^{-1}\text{s}^{-1}$  for RGD- and NT-pQDs incubated HUVECs, respectively. These cellular longitudinal relaxivities were lower than the longitudinal relaxivities found for pQDs in HBS ( $r_1 = 5.2 \pm 0.1 \text{ mM}^{-1}\text{s}^{-1}$  and  $5.7 \pm 0.3 \text{ mM}^{-1}\text{s}^{-1}$  for RGD- and NT-pQDs, respectively). The decrease in longitudinal relaxivity could stem from cellular internalization. The observed linear relationship between the  $R_1$  and the Gd-concentration suggests that no Gd-concentration or time-dependent changes were present in the longitudinal relaxivity of pQDs within this Gd-concentration range. Furthermore, RGD- and NT-pQDs displayed similar cellular longitudinal relaxivities, which was also the case for the RGD- and NT-pQDs in HBS. This is significantly different from the findings described in Chapter 2 using RGD-targeted paramagnetic liposomes (RGD-liposomes) and non-targeted paramagnetic liposomes (NT-liposomes) in an identical experimental setup. Within a similar Gd-concentration range as obtained with the present pQD-incubation experiment, the longitudinal relaxivity of the RGD-liposomes was reduced by a factor 2 in comparison to the NT-liposomes. To illustrate this pronounced difference in the longitudinal relaxivity between HUVEC-associated pQDs and liposomes, the  $R_1$  versus the Gd-concentration of RGD- and NT-liposomes from the Chapter 2 data were also plotted in Figure 6A. Both RGD- and NT-liposomes displayed a linear relationship between  $R_1$  and Gd-concentration within this Gd-concentration range. A linear fit was made using the least squares method, yielding an  $R^2$  of 0.98 and 0.95 and a longitudinal relaxivity of  $1.7 \pm 0.1 \text{ mM}^{-1}\text{s}^{-1}$  and  $3.8 \pm 0.3 \text{ mM}^{-1}\text{s}^{-1}$  for RGD- and NT-liposomes, respectively. In Chapter 2, it was hypothesized that this dissimilarity in longitudinal relaxivity was caused by the difference in size of the vesicular structures entrapping the cell-internalized liposomes. It was postulated that the difference in size between the liposome-containing vesicles was caused by different cellular uptake mechanisms, with RGD-liposomes presumably being taken up via caveolae-mediated endocytosis [26]. The RGD-pQDs did not exhibit this longitudinal quenching by a factor 2 in comparison to the NT-pQDs, which may suggest that the size of the vesicles containing the internalized pQDs was similar for RGD- and NT-pQDs. This indication is in consensus with the obtained



CLSM images of pQD-incubated HUVECs (Figure 2), which displayed no obvious size difference between pQD-positive structures in RGD- and NT-pQD incubated HUVECs.

The transverse relaxation rate versus gadolinium concentration within the cell pellets is plotted in Figure 6B. A linear fit was made for both RGD- and NT-pQD incubated HUVECs, using the least squares method. The corresponding  $R^2$  values of the linear fits were 0.81 and 0.71 for RGD- and NT-pQDs, respectively. The low  $R^2$  values are likely caused by the small differences in  $R_2$  between datapoints and the relatively large standard deviations of the data points. An alternative explanation could be that the  $T_2$ -relaxation regime changes during incubation, yielding a non-linear relationship between the  $R_2$  and the gadolinium concentration. Such a change in  $T_2$ -relaxation regime could for example be induced by clustering of particles, which is not an unlikely scenario for cell-internalized contrast agent. In view of the relatively poor linear correlation, the transversal relaxivity  $r_2$  was not calculated. It is clear, however, that in this Gd-concentration regime, there were only modest changes in  $R_2$ . This made differentiation between RGD- and NT-pQDs on the basis of  $R_2$  data very difficult, irrespective of whether the  $R_2$  is a linear function of the Gd-concentration.

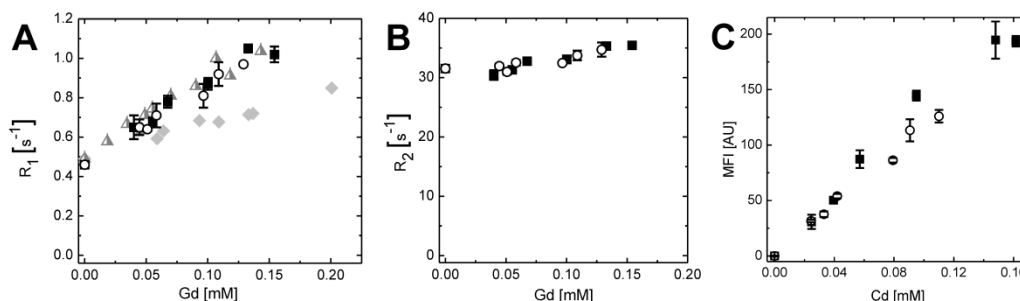


**Figure 6: Relaxometric (A,B) and optical properties (C) of cell-internalized pQDs as function of Gd (A,B) and Cd (C) concentration in the cell pellets. (A)  $R_1$  versus the gadolinium concentration of HUVECs incubated with RGD-pQDs (solid squares) or NT-pQDs (open circles). The solid diamonds and half-open triangles represent previous data from HUVECs incubated with RGD-liposomes and NT-liposomes, respectively (Chapter 2). For clarity, error bars were omitted for the liposome data. Error bars for the liposome data were in same order of magnitude as for the pQD data. (B)  $R_2$  versus the gadolinium concentration of HUVECs incubated with RGD-pQDs or NT-pQDs. (C) mean fluorescence intensity per cell (MFI) versus the cadmium concentration in HUVEC cell pellets, following incubation with either RGD-pQDs or NT-pQDs. Data represent mean  $\pm$  SD ( $n=3$ ).**

The optical properties of the cell-internalized pQDs were probed by determining the mean fluorescence intensity (MFI) per cell. The mean fluorescent intensity versus the cadmium concentration in the cell pellets was plotted in Figure 6C.

An essentially linear relationship between MFI per cell and cadmium content in cell pellets was found for both RGD- and NT-pQDs using the least squares method, which yielded an  $R^2 > 0.98$  for both types of agents. These findings suggest that there were no concentration- or time-dependent alterations in the fluorescent properties of cell-internalized pQDs, which makes it possible to assess the pQDs uptake using fluorescent imaging. Furthermore it demonstrated that pQDs fluorescent properties were stable even after uptake by cells. The relationship between MFI per cell and cadmium concentration was similar for RGD- and NT-pQDs, indicating that both types of internalized pQDs behaved similarly with respect to mean fluorescent intensity per quantum dot core.

The fact that RGD- and NT-pQDs did not show any concentration and time-dependent change in both the longitudinal relaxivity and fluorescent intensity upon cellular internalization makes it possible to quantify *in vitro* the cellular uptake for both the RGD- and NT-pQDs by exploiting their paramagnetic and optical properties. Furthermore, RGD- and NT-pQDs possessed similar cell-associated longitudinal relaxivities and cellular fluorescence intensities per internalized quantum dot core, enabling the use of relaxometric and optical measurements to quantify the effect of RGD-targeting on the uptake of pQDs in HUVECs. This is especially useful for *in vivo* molecular imaging applications, as targeted nanoparticles are often compared to their non-targeted counterparts to assess their ability to generate specific contrast.

The increased Gd/Cd molar ratio of both RGD- and NT-pQDs incubated HUVECs (Figure 4), however, may complicate relaxometric quantification of the cellular-internalization of pQDs, as the overshoot in Gd-content in the cells may result in an overestimation of the amount of internalized pQDs. Furthermore, the increased Gd/Cd molar ratio for NT-pQDs in comparison to the RGD-pQDs incubated HUVECs (Figure 4) hampers the relaxometric differentiation between RGD- and NT-pQDs incubated HUVECs. This compromises the ability of relaxometric measurements to correctly quantify the effect of RGD-targeting on the cellular uptake of pQDs *in vitro* and *in vivo*. In order to allow for correct quantification of cellular uptake of pQDs by relaxometry, it would be advantageous to stabilize the lipid-coating of the pQDs to prevent lipid-transfer from the pQD coating to the cell membrane, as we regard lipid-transfer the most plausible cause of the change in Gd/Cd molar ratio in the pellets containing pQD-incubated HUVECs. Several methods are available to stabilize the lipid coating, including the use of block-copolymers that can be tuned to form micelles or polymersomes with a very low critical micelle concentration [27, 28]. The same polymers may also be used to coat the surface of quantum dots [29]. A different approach is to introduce crosslinks in the monolayer

covering the surface to stabilize the nanoparticles as was performed for micelles [30, 31]. Furthermore, the quantum dots used in this thesis were capped with octadecylamine. Instead of capping the quantum dots with a hydrophobic compound, a compound can be introduced that is either water soluble or can be chemically converted to be water soluble [32, 33]. Since quantum dots are extremely prone to oxidation, the latter option seems most suitable. Another option would be to employ lipids containing one or more unsaturated carbon-carbon bonds in their fatty acyl chain for the lipid coating of the pQDs. Utilization of unsaturated lipids leads to a lower gel-to-liquid crystalline phase-transition temperature, which is hypothesized to stabilize the lipid coating of the pQDs, thereby reducing the rate of lipid-transfer.

In addition to hampering the relaxometric differentiation between both types of pQDs, the proposed lipid-transfer from the pQDs to the cells may have also induced a mild toxic effect, which could explain the change in cell-morphology during incubation. However, no obvious increase in cell death or rounding up and detaching of cells was observed for the HUVECs during pQD-incubation with both types of pQDs.

The findings in this study regarding the proposed lipid-exchange show that for contrast agents that are (partially) prepared by the use of non-covalent interactions, a biological environment is able to change the composition of the contrast agents and thus able to corrupt the imaging read-out. This is particularly important to recognize when using bimodal contrast agents where both types of imaging labels are incorporated via non-covalent interactions, as the obtained information from such a bimodal contrast agent may become ambiguous due to reduced co-localization of the two types of imaging labels in biological environments. It is important to stress that, although all the collected data support our proposed hypothesis of non-specific lipid-transfer from the pQD-lipid coating towards cellular membranes, this hypothesis lacks independent experimental evidence. Future incubation experiments including an appropriate fluorescent-dye attached to lipids situated in the pQD-coating could provide a means to test this hypothesis, as this would allow for the visualization using CLSM of both the QD-core and the lipids (initially) situated in the coating of the pQDs.

## **Conclusions**

We described the successful preparation of pQDs displaying high monodispersity and excellent optical properties. *In vitro* targeting of pQDs with the RGD-peptide was accomplished, as the conjugation of RGD to the pQDs led to a higher uptake for pQDs in HUVECs. This study showed that cell internalization influenced the relaxometric and compositional properties of the pQDs. Internalized RGD- and NT-pQDs showed lower relaxivities in comparison to the pQD-relaxivity in HBS, whereas the Gd/Cd molar ratio in pellets containing pQD-incubated HUVECs was significantly higher than the Gd/Cd molar ratio of the pQDs as prepared, hampering the assessment of pQD-uptake by cells using relaxometric measurements. It is proposed that the increase in Gd/Cd molar ratio was due to non-specific lipid-transfer between the pQDs and the cellular membranes. However, it was still possible to accurately assess the Gd and Cd uptake by HUVECs using relaxometric or optical measurements, as pQDs showed no concentration or time-dependent change in fluorescence intensities or relaxivities upon cell uptake. Furthermore, it was shown that the RGD-pQDs did not display a difference in either relaxivity or fluorescent intensity in comparison to their non-targeted counterparts upon internalization in HUVECs, enabling the use of relaxometric and optical measurements to quantify the effect of RGD-targeting on the Gd and Cd uptake in HUVECs.

## Literature

1. Weissleder, R., U. Mahmood, *Radiology*, 2001. **219**(2): p. 316-333.
2. Lee, K.T., Sagel, S.S., Stanley, R.J., Heiken, J.P., *Computed body tomography with MRI correlation*. 4 ed. Vol. 1. 2005. 2050.
3. Nunn, A.D., K.E. Linder, M.F. Tweedle, *Q J Nucl Med*, 1997. **41**(2): p. 155-162.
4. Mulder, W.J., G.J. Strijkers, G.A. van Tilborg, *et al.*, *NMR Biomed*, 2006. **19**(1): p. 142-164.
5. Aime, S., D.D. Castelli, S.G. Crich, *et al.*, *Accounts of Chemical Research*, 2009. **42**(7): p. 822-831.
6. Mulder, W.J., R. Koole, R.J. Brandwijk, *et al.*, *Nano Lett*, 2006. **6**(1): p. 1-6.
7. Mulder, W., K. Castermans, J. van Beijnum, *et al.*, *Angiogenesis*, 2009. **12**(1): p. 17-24.
8. Xing, Y., J. Rao, *Cancer Biomark*, 2008. **4**(6): p. 307-319.
9. Bailey, R.E., A.M. Smith, S. Nie, *Physica E: Low-dimensional Systems and Nanostructures*, 2004. **25**(1): p. 1.
10. Smith, A.M., H. Duan, A.M. Mohs, *et al.*, *Adv Drug Deliv Rev*, 2008. **60**(11): p. 1226-1240.
11. Zhong, X., Y. Feng, W. Knoll, *et al.*, *J Am Chem Soc*, 2003. **125**(44): p. 13559-13563.
12. Pietryga, J.M., R.D. Schaller, D. Werder, *et al.*, *J Am Chem Soc*, 2004. **126**(38): p. 11752-11753.
13. Xie, R., K. Chen, X. Chen, *et al.*, *Nano Research*, 2008. **1**(6): p. 457.
14. Cai, W., D.W. Shin, K. Chen, *et al.*, *Nano Lett*, 2006. **6**(4): p. 669-676.
15. Lauffer, R.B., D.J. Parmelee, S.U. Dunham, *et al.*, *Radiology*, 1998. **207**(2): p. 529-538.
16. Caravan, P., J.J. Ellison, T.J. McMurry, *et al.*, *Chemical Reviews*, 1999. **99**(9): p. 2293-2352.
17. Aime, S., A. Barge, C. Cabella, *et al.*, *Curr Pharm Biotechnol*, 2004. **5**(6): p. 509-518.
18. Terreno, E., S.G. Crich, S. Belfiore, *et al.*, *Magnetic Resonance in Medicine*, 2006. **55**(3): p. 491-497.
19. Geninatti, C., C. Cabella, A. Barge, *et al.*, *Journal of Medicinal Chemistry*, 2006. **49**(16): p. 4926-4936.
20. Brekke, C., S.C. Morgan, A.S. Lowe, *et al.*, *NMR in Biomedicine*, 2007. **20**(2): p. 77-89.
21. Jin, H., J. Varner, *Br J Cancer*, 2004. **90**(3): p. 561-565.
22. Brooks, P.C., R.A. Clark, D.A. Cheresch, *Science*, 1994. **264**(5158): p. 569-571.
23. de Mello Donega, C., M. Bode, A. Meijerink, *Physical Review B (Condensed Matter and Materials Physics)*, 2006. **74**(8): p. 085320-085329.
24. Koole, R., M.M. van Schooneveld, J. Hilhorst, *et al.*, *Chemistry of Materials*, 2008. **20**(7): p. 2503.
25. Havel, R.J., H.A. Eder, J.H. Bragdon, *J Clin Invest*, 1955. **34**(9): p. 1345-1353.
26. Caswell, P.T., J.C. Norman, *Traffic*, 2006. **7**(1): p. 14-21.
27. Jones, M., J. Leroux, *Eur J Pharm Biopharm*, 1999. **48**(2): p. 101-111.
28. Kwon, G.S., T. Okano, *Pharm Res*, 1999. **16**(5): p. 597-600.
29. Nasongkla, N., E. Bey, J. Ren, *et al.*, *Nano Lett*, 2006. **6**(11): p. 2427-2430.
30. Shuai, X., T. Merdan, A.K. Schaper, *et al.*, *Bioconjug Chem*, 2004. **15**(3): p. 441-448.
31. Weaver, J.V., Y. Tang, S. Liu, *et al.*, *Angew Chem Int Ed Engl*, 2004. **43**(11): p. 1389-1392.
32. Di Marco, M., C. Sadun, M. Port, *et al.*, *Int J Nanomedicine*, 2007. **2**(4): p. 609-622.
33. Portet, D., B. Denizot, E. Rump, *et al.*, *J Colloid Interface Sci*, 2001. **238**(1): p. 37-42.

## Chapter **6**

### **Quantitative $^1\text{H}$ MRI, $^{19}\text{F}$ MRI, and $^{19}\text{F}$ MRS of cell-internalized perfluorocarbon paramagnetic nanoparticles**

**Based on:**

*Quantitative  $^1\text{H}$  MRI,  $^{19}\text{F}$  MRI, and  $^{19}\text{F}$  MRS of cell-internalized perfluorocarbon paramagnetic nanoparticles*

M.B. Kok, A. de Vries, D. Abdurrachim, J.J. Prompers, H. Gruell, K. Nicolay, G. J. Strijkers

Submitted

**Abstract:**

*In vivo* molecular imaging with targeted MRI contrast agents requires sensitive methods to quantify local concentrations of contrast agent, enabling not only imaging-based recognition of pathological biomarkers but also detection of changes in expression levels as a consequence of disease development, therapeutic interventions or recurrence of disease. In recent years, targeted paramagnetic perfluorocarbon emulsions have been frequently applied in this context, permitting high-resolution  $^1\text{H}$  MRI combined with quantitative  $^{19}\text{F}$  MR imaging or spectroscopy, under the assumption that the fluorine signal is not altered by the local tissue and cellular environment. In this *in vitro* study we have investigated the MR-based quantification potential of a lipid-based paramagnetic perfluorocarbon emulsion conjugated with RGD-peptide as to target the cell-internalizing  $\alpha_v\beta_3$ -integrin expressed on endothelial cells, using a combination of  $^1\text{H}$  MRI,  $^{19}\text{F}$  MRI and  $^{19}\text{F}$  MRS. The cells took up the targeted emulsion to a higher extent than non-targeted emulsion. The targeted emulsion was internalized into large 1 to 7  $\mu\text{m}$  diameter vesicles in the perinuclear region, whereas non-targeted emulsion ended up in 1 to 4  $\mu\text{m}$  diameter vesicles, which were more evenly distributed in the cytoplasm. Association of the targeted emulsion with the cells resulted in a concentration-dependent proton  $R_1$  with different values for targeted and control nanoparticles, prohibiting unambiguous quantification of local contrast agent concentration. Upon cellular association, the fluorine  $R_1$  remained constant with concentration, while the fluorine  $R_2$  increased with concentration. Even though the fluorine  $R_2$  was not constant, the  $^{19}\text{F}$  MRI and  $^{19}\text{F}$  MRS signals were linear and quantifiable as function of nanoparticle concentration.

## Introduction

In recent years, numerous targeted MR contrast agents have been developed that can be employed for the molecular detection and characterization of diseases such as cancer [1], atherosclerosis [2] and myocardial infarction [3]. Association of MRI contrast agents with a specific target generally is detected by an increase in  $^1\text{H}$  MRI signal intensity, on  $T_1$ -weighted scans for paramagnetic contrast agents, or a decrease on  $T_2/T_2^*$ -weighted scans for superparamagnetic contrast agents. Since several mechanisms such as compartmentalization, internalization, and processing of the contrast agent by cells after binding, may influence the relaxivity of the contrast agent, it is not straightforward to quantify contrast agent concentration from the changes in  $^1\text{H}$  MRI signal intensity, or from  $T_1$ - or  $T_2$ -values. Previously we have studied the internalization of  $\alpha_v\beta_3$ -targeted (RGD) and non-targeted (NT) paramagnetic liposomes by human umbilical vein derived endothelial cells (HUVECs) and its effect on both the longitudinal and transverse relaxivity (Chapter 2 and 3). We have shown that internalization of the targeted contrast agent lowered the longitudinal relaxivity in a concentration dependent manner, thereby severely complicating quantification. Quantification of the contrast agent concentration, however, could prove essential for successful application in the areas of cell tracking [4-8], MRI monitored drug delivery [9, 10] and molecular MRI [1-3].

A class of contrast agents that offers great potential for quantification are the fluorine ( $^{19}\text{F}$ ) based contrast agents. In contrast with the Gd-based agents, for which changes in signal intensity in  $^1\text{H}$  MRI originate from water protons in close proximity to the paramagnetic center,  $^{19}\text{F}$ -based contrast agent can directly be detected by  $^{19}\text{F}$  MRI or MRS. A variety of  $^{19}\text{F}$ -containing contrast agents have been introduced previously including micelles [11], liposomes [12] and emulsions [13]. By combining  $^1\text{H}$  with  $^{19}\text{F}$  imaging, the  $^{19}\text{F}$  MR signal can be placed into anatomical context. Additionally, Gd-based contrast-enhanced  $^1\text{H}$  imaging could enable initial high-resolution detection of contrast agent accumulation, followed by quantification using  $^{19}\text{F}$  MRS or  $^{19}\text{F}$  MRI. Although a considerable number of studies have utilized  $^{19}\text{F}$  imaging and  $^{19}\text{F}$  MRS of fluorine-containing nanoparticles *in vitro* [14, 15] and *in vivo* [16-23], thus far only a limited number of papers have addressed the consequences of cellular association on the  $^{19}\text{F}$  signals [16, 24, 25]. For reliable *in vivo* quantification, however, it is necessary to know whether cellular binding and internalization influence the relaxometric properties and the linearity of the MR signals with fluorine concentration.

In this *in vitro* study we therefore have examined the quantification potential and the changes in relaxometric properties of a lipid-based paramagnetic



perfluorocarbon emulsion upon internalization by human endothelial cells. A paramagnetic perfluorocarbon emulsion was used containing amphiphilic  $Gd^{3+}$ -chelates for detection by  $^1H$  MRI, a perfluoro-15-crown-5-ether (PFCE) core for  $^{19}F$  MRI and MRS and fluorescent lipids to follow cellular uptake using confocal laser scanning microscopy. The emulsion was cell internalized by targeting of the  $\alpha_v\beta_3$ -integrin receptor expressed on the endothelial cells using a cyclic RGD-peptide ligand. Emulsion without the cyclic RGD-peptide served as a control system for non-specific binding and uptake. The association of contrast agents with the cells was monitored using several techniques including  $^1H$  MRI,  $^{19}F$  MRI,  $^{19}F$  MRS, fluorescent activated cell sorting (FACS), confocal laser scanning microscopy (CLSM) and inductively coupled plasma atomic emission spectrometry (ICP-AES).

## Methods

### Materials

1,2-Distearoyl-*sn*-glycero-3-phosphocholine (DSPC), cholesterol, 1,2-distearoyl-*sn*-glycero-3-phosphoethanolamine-N-[methoxy(polyethyleneglycol)-2000] (PEG<sub>2000</sub>-DSPE), 1,2-distearoyl-*sn*-glycero-3-phosphpethanolamine-N-[maleimide(polyethyleneglycol)-2000] (Mal-PEG<sub>2000</sub>-DSPE) and 1,2-dipalmitoyl-*sn*-3-phosphoethanolamine-N-[lissamine rhodamine B sulfonyl] (rhodamine-PE) were obtained from Avanti Polar Lipids (Alabaster, AL, USA). 1,2-distearoyl-*sn*-glycero-3-phosphpethanolamine-[tetraazacyclododecanetetraacetic acid] (Gd-DOTA-DSPE) were synthesized by SyMO-Chem (Eindhoven, the Netherlands) [26]. Endothelial Growth Medium-2 (EGM-2) and human umbilical vein derived endothelial cells (HUVECs) were ordered with Lonza Bioscience (Switzerland). Monoclonal mouse anti-human CD31 antibody was obtained from Dakocytomation (Glostrup, Denmark). Alexa Fluor 488 conjugated goat anti-mouse secondary antibody was from Molecular Probes Europe BV (Leiden, the Netherlands). The cyclic RGD-peptide (c(RGDf(-S-acetylthioacetyl)K)) was synthesized by Ansynth Service BV (Roosendaal, the Netherlands). All other chemicals were obtained from Sigma (St. Louis, MO, USA) and were of analytical grade or the best grade available.

### Emulsion preparation and characterization

Emulsions were prepared from perfluoro-15-crown-5-ether (PFCE), Gd-DOTA-DSPE, DSPC, cholesterol, PEG<sub>2000</sub>-DSPE and Mal-PEG<sub>2000</sub>-DSPE at a molar ratio of 0.75/1.10/1/0.075/0.075. In detail, 600 μmol total lipids were dissolved in 8 mL 1:5 methanol:chloroform mixture. As a fluorescent marker, 0.1 mole percent of rhodamine-PE was added. A lipid film was created by evaporating the chloroform/methanol mixture using a Rotavapor R200 (Buchi, Flawil, Switzerland). The lipid film was hydrated at 70 °C using a mixture of 4.5 g PFCE and 15 mL THAM buffer, containing 0.0252% w/v trishydroxymethyl aminomethane (THAM) and 8.9 g/l NaCl (pH 7.4). The crude emulsion was homogenized for 30 s using an Ultra-Turrax T8 (IKA-Werke, Staufen, Germany) and subsequently processed for 3 min in a high-pressure microfluidizer (M-110S, Microfluidics, Newton, MA, USA) at 1500 bar, which was preheated to 60 °C. The final emulsion was cooled down in an ice bath. After preparation of the emulsion suspension, half of the suspension was modified with a cyclic RGD-peptide (6 μg/μmol total lipid) to target the α<sub>v</sub>β<sub>3</sub>-integrin. The cyclic RGD-peptide was deacetylated and coupled to the distal end of Mal-PEG<sub>2000</sub>-DSPE overnight at room temperature. Lipid concentration was measured by phosphate determination according to Rouser *et al.* [27]. Size and size-distribution of the emulsions were determined with dynamic light scattering (DLS) (Zetasizer Nano, Malvern, UK) at 25 °C. Longitudinal and transverse relaxivity were

determined at 6.3 T and room temperature by linear fits of  $R_1$  ( $\equiv 1/T_1$ ) and  $R_2$  ( $\equiv 1/T_2$ ) values as a function of the gadolinium concentration as determined using inductively coupled plasma atomic emission spectroscopy (ICP-AES). Fluorine content of the emulsion was determined using ion chromatography. The concentration of nanoparticles (NP) was calculated using an estimated  $2.25 \times 10^4$  Gd-containing lipids per nanoparticle. This value was obtained by dividing the surface area of an emulsion with a diameter of 175 nm by the surface area of a single lipid present in a monolayer (42.5 Å) and taking into account a 1 to 9 ratio of gadolinium-containing lipids to total lipids. Emulsion was stored for 30 days at room temperature before use in the incubation experiments. In this paper we refer to emulsion conjugated with RGD-peptide as RGD-emulsion. Non-targeted emulsion, which was not conjugated with a targeting ligand, is referred to as NT-emulsion.

#### Incubations of HUVEC with emulsions

Human umbilical vein derived endothelial cells (HUVECs) were used for all the experiments. Cells were stored in liquid nitrogen upon arrival. Before use, the cells were quickly thawed in a water bath ( $T = 37^\circ\text{C}$ ) and divided over 2 gelatin coated T75 TCPS flasks (VWR, West Chester, PA, USA). Cells were cultured in a humidified incubator at  $37^\circ\text{C}$  with 5%  $\text{CO}_2$ . The EGM-2 medium was replaced every 2 to 3 days. Cells of passage 3 or 4 were used for all experiments at 80 to 90% confluency. Incubations were carried out on both gelatin-coated coverslips, for CLSM analysis, and in gelatin-coated T75 TCPS culture flasks, for MRI, FACS and ICP-AES analyses. All measurements were done in triplicate for both types of emulsions and each incubation time. At the start of the experiment, medium was replaced by either RGD-emulsion or NT-emulsion containing medium at a concentration of  $1\ \mu\text{mol}$  total lipid per mL medium. Four mL of emulsion-containing medium was added to the T75 gelatin-coated TCPS flasks and 0.5 mL of medium was added to the gelatin-coated coverslips. The incubation time with emulsion containing medium was varied between 0 and 24 hr. After the incubation, cells were washed three times with 5 mL prewarmed ( $37^\circ\text{C}$ ) HEPES-buffered saline solution to remove non-adherent emulsions. After these washing steps, the cells grown on coverslips were fixed using 4% PFA for 15 min at room temperature, 3 times washed with PBS and subsequently stored in the dark at  $4^\circ\text{C}$ . Cells in culture flasks were detached using 2 mL 0.25% w/v trypsin, 1 mM EDTA·4Na (Lonza Bioscience, Switzerland). The trypsin solution was neutralized using 4 mL trypsin neutralizing solution (Lonza Bioscience, Basel, Switzerland). Cells were spun down at 220 g and the supernatant was removed and the cell pellet was resuspended in 250  $\mu\text{L}$  4% paraformaldehyde solution in PBS and transferred to a 300  $\mu\text{L}$  Eppendorf cup. A loosely-packed cell

pellet was formed by centrifugation at 20 g for 5 min. The cell pellets were stored at room temperature in the dark.

#### Confocal laser scanning microscopy

After fixation, the coverslips with HUVECs incubated with emulsion were stained using a mouse anti-human CD31 antibody to visualize the cell membrane. The cells were rinsed for 5 min with PBS followed by 60 min of incubation with the primary mouse anti-human CD31 antibody (1:40 dilution). Subsequently the cells were washed  $3 \times 5$  min with PBS followed by 30 min of incubation with a secondary Alexa Fluor 488 goat anti-mouse IgG antibody (1:200 dilution). The cells were washed  $3 \times 5$  min with PBS and the nuclei were stained for 5 min with DAPI. After staining of the nuclei, the cells were rinsed  $3 \times 5$  min with PBS and subsequently mounted on a microscopy slide using Mowiol mounting medium.

Confocal fluorescence images were recorded at room temperature on a Zeiss LSM 510 META system using a Plan-Apochromat<sup>®</sup> 63 $\times$ /1.4 NA oil-immersion objective. Alexa Fluor 488 and rhodamine-PE were excited using the 488 and 543 nm lines of a HeNe laser, respectively. The fluorescence emission of Alexa Fluor 488 was recorded with photomultiplier tubes (Hamamatsu R6357) after spectral filtering with a NFT 490 nm beamsplitter followed by a 500 to 550 nm bandpass filter. Rhodamine-PE emission was analyzed using the Zeiss Meta System in a wavelength range of 586 to 704 nm. DAPI staining of nuclei was visualized by two-photon excitation fluorescence microscopy performed on the same Zeiss LSM 510 system. Excitation at 780 nm was provided by a pulsed Ti:Sapphire laser (Chameleon<sup>™</sup>; Coherent, Santa Clara, CA, USA), and fluorescence emission was detected with a 395 to 465 nm bandpass filter. All experiments were combined in multitrack mode and acquired confocally.

#### Magnetic resonance imaging and spectroscopy

In this paper we refer to relaxometric properties for proton with subscript H and for fluorine with subscript F.  $R_{1,H}$  and  $R_{2,H}$  relaxation rates and the volumes of the cell pellets were measured using a 6.3 T horizontal bore animal MR scanner (Bruker BioSpec, Ettlingen, Germany). All measurements were carried out at room temperature.  $^1\text{H}$  longitudinal and transverse relaxation rates were measured in a 3-cm-diameter send and receive quadrature-driven birdcage coil (Rapid Biomedical, Rimpfing, Germany). The Eppendorf tubes containing the loosely-packed cell pellets were placed in a custom made holder (4 tubes at a time), which was filled with HEPES buffered saline solution to facilitate shimming.  $R_{1,H}$  was measured using a fast inversion recovery segmented FLASH sequence with an echo time (TE) of 1.5 ms, a repetition time (TR) of 3.0 ms, a flip angle of  $15^\circ$ , and an inversion time (TI) ranging from 67 ms to 4800 ms in

80 steps. Overall repetition time was 20 s. Field of view (FOV) =  $3 \times 2.18 \text{ cm}^2$ , matrix size =  $128 \times 128$ , slice thickness = 0.75 mm and NSA = 2.  $R_{2,H}$  was measured using a multi-slice multi-echo sequence with TE ranging between 9 and 288 ms in 32 steps and TR = 1000 ms, FOV =  $3 \times 2.2 \text{ cm}^2$ , slice thickness = 0.75 mm, matrix size =  $128 \times 128$ , and NSA = 4. From the images  $R_{1,H}$ - and  $R_{2,H}$ -maps were calculated using Mathematica (Wolfram Research Inc, Champaign, IL, USA).  $R_{1,H}$  and  $R_{2,H}$  of the cell pellets are reported as the mean  $\pm$  SD of a selected region-of-interest (ROI) within the pellet. The volume of the cell pellet was determined for each sample separately in a 0.7-cm-diameter solenoid coil using a 3D FLASH sequence with TE = 3.2 ms, TR = 25 ms, flip angle =  $30^\circ$ , FOV =  $1.6 \times 1.6 \times 1.6 \text{ cm}^3$ , matrix size =  $128 \times 128 \times 128$  and NSA = 1. A threshold value was determined manually to select the voxels inside the pellet, which were multiplied by the voxel volume to obtain the total volume of the pellet. The concentration of gadolinium in each cell pellet was determined by dividing the gadolinium content by the pellet volume.

$^1\text{H}$  MRI,  $^{19}\text{F}$  MRI and  $^{19}\text{F}$  MRS were performed using a homebuilt 5-mm-diameter solenoid coil, which was tuned to the  $^1\text{H}$  and  $^{19}\text{F}$  resonance frequencies.  $^1\text{H}$  MRI was performed using a FLASH sequence with TE = 3.2 ms, TR = 100 ms, flip angle =  $20^\circ$ , FOV =  $2.0 \times 2.0 \text{ cm}^2$ , matrix size =  $128 \times 128$ , slice thickness = 2 mm and NSA = 128. Total acquisition time was approximately 10 min.  $^{19}\text{F}$  MRI was done using a FLASH sequence with TE = 2.7 ms, TR = 100 ms, flip angle =  $40^\circ$ , FOV =  $2.0 \times 2.0 \text{ cm}^2$ , matrix size =  $128 \times 128$ , slice thickness = 2 mm and NSA = 128. As for  $^1\text{H}$  MRI, the total acquisition time was approximately 10 min. Average signal intensity was determined in a selected ROI within the pellet.  $^{19}\text{F}$  MR spectra were obtained by using a spectroscopic spin echo sequence with TE = 2.5 ms, TR = 5000 ms, adiabatic  $90^\circ$  and  $180^\circ$  pulses and 2 dummy shots. A small sphere containing trifluoroacetic acid (TFA) was used as a reference for  $^{19}\text{F}$  MRS. Number of averages was 8 for HUVECs incubated with RGD-emulsion and number of averages was 64 for HUVECs incubated with NT-emulsion.  $R_{2,F}$  was determined using the same spectroscopic spin echo sequence by varying the TE from 2.5 to 100 ms in 11 steps.  $R_{1,F}$  was determined by varying TR from 220 to 5000 ms in 11 steps. The peak intensity and area were determined with the TOPSPIN 1.5 software (Bruker Biospin) and corrected for  $R_{2,F}$ .

#### MR detection threshold analysis

Detection thresholds, expressed as the concentration of contrast agent, were determined for  $^1\text{H}$  MRI and  $^{19}\text{F}$  MRI in a circular region of interest (ROI) situated in the cell pellet and for  $^{19}\text{F}$  MRS from peak area of the whole pellet. For  $^1\text{H}$  MRI,

contrast to noise ratios (CNR) were determined by subtracting the signal to noise ratio (SNR) of  $T_1$ -weighted images from pellets of non-incubated HUVECs from those of cells incubated with contrast agent. Since non-incubated HUVEC do not contain fluorine,  $^{19}\text{F}$  MRI and  $^{19}\text{F}$  MRS CNR values were defined with respect to background noise levels (CNR = SNR). Detection thresholds were estimated by determining the minimal contrast agent concentration required to cause a significant change in contrast (CNR > 5), taking into account the standard deviation of measurements using a student's t-test.

## Results

Dynamic light scattering (DLS) revealed an average diameter of approximately 170 nm for both the RGD-conjugated (RGD-emulsion) and non-targeted (NT-emulsion) nanoparticles. After preparation, typical lipid concentrations of about 25 mM in the final emulsion suspension were obtained. To study the effect of Ostwald ripening, a molecular diffusion phenomenon that results in a gradual growth of the larger particles at the expense of smaller ones, repeated DLS measurements were performed over a period of 80 days (Figure 1A). After 80 days, a small increase of about 10 nm in average particle diameter was observed. The polydispersity index (PDI) was found to be 0.10 for both emulsion types at all time points. Figures 1B and C show cryo-TEM images of the RGD- and NT-emulsions, respectively. The cryo-TEM images revealed spherical particles with a dark core, typical for PFCE-filled emulsions. The suspension contained essentially no liposomes. Proton longitudinal and transverse relaxivity at 6.3 T and room temperature were  $r_{1,H} = 7.4 \pm 0.1 \text{ mM}^{-1}\text{s}^{-1}$ ,  $r_{1,H} = 8.0 \pm 0.2 \text{ mM}^{-1}\text{s}^{-1}$ , and  $r_{2,H} = 36.8 \pm 0.3 \text{ mM}^{-1}\text{s}^{-1}$ ,  $r_{2,H} = 41.3 \pm 0.2 \text{ mM}^{-1}\text{s}^{-1}$  for RGD- and NT-emulsions, respectively.

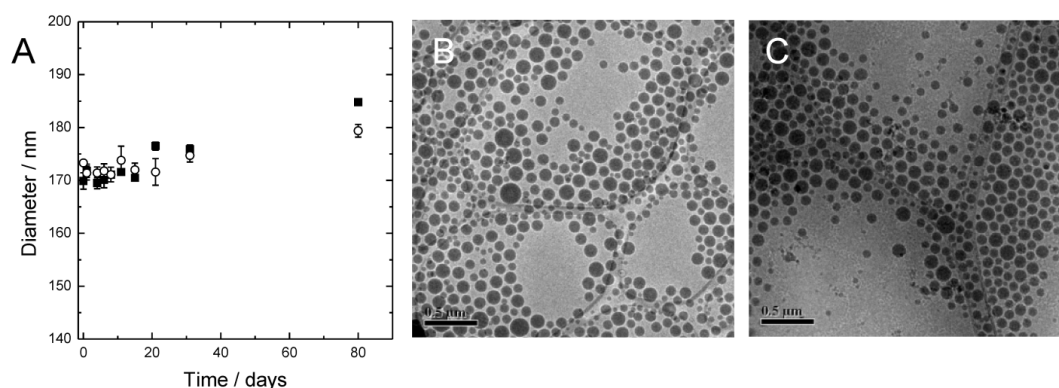


**Figure 1, Nanoparticle characterization. (A) Nanoparticle diameter of RGD-emulsion (solid squares) and NT-emulsion (open circles) as function of time after preparation (mean  $\pm$  SD). (right) Cryo-TEM of (B) RGD-emulsion and (C) NT-emulsion. The scale bar equals 0.5  $\mu\text{m}$ .**

After incubation of the cells with emulsion, the intracellular localization of the contrast agent was visualized by CLSM by exploiting the rhodamine-PE present in the lipid layer surrounding the hydrophobic PFCE core. Figure 2 shows confocal images of HUVECs incubated with either RGD- or NT-emulsions. The brighter rhodamine-PE fluorescence indicated that the RGD-emulsion was taken up to a higher extent than the NT-emulsion. The fluorescent signal of internalized RGD-emulsion was mainly located in vesicular structures in the perinuclear region. The diameter of these vesicular structures increased from around 1-5  $\mu\text{m}$  after 1 hr of incubation to between 4-7  $\mu\text{m}$  after 8 hr of 120

incubation. After 8 hr of incubation with RGD-emulsion, fluorescence was additionally observed throughout the entire cytoplasm. Incubation with NT-emulsion resulted in fluorescent vesicular structures located throughout the entire cytoplasm. The diameter of these fluorescent structures increased from about 1-2  $\mu\text{m}$  after 1 hr of incubation to about 3-4  $\mu\text{m}$  after 8 hr of incubation. Only minor association of the emulsion with the cellular membrane was observed for incubations with both RGD- and NT-emulsion. For incubation times longer than 3 hr the cells appeared smaller than at the beginning and after 24 hr some dead cells were observed in the medium, suggesting a mild toxic effect.

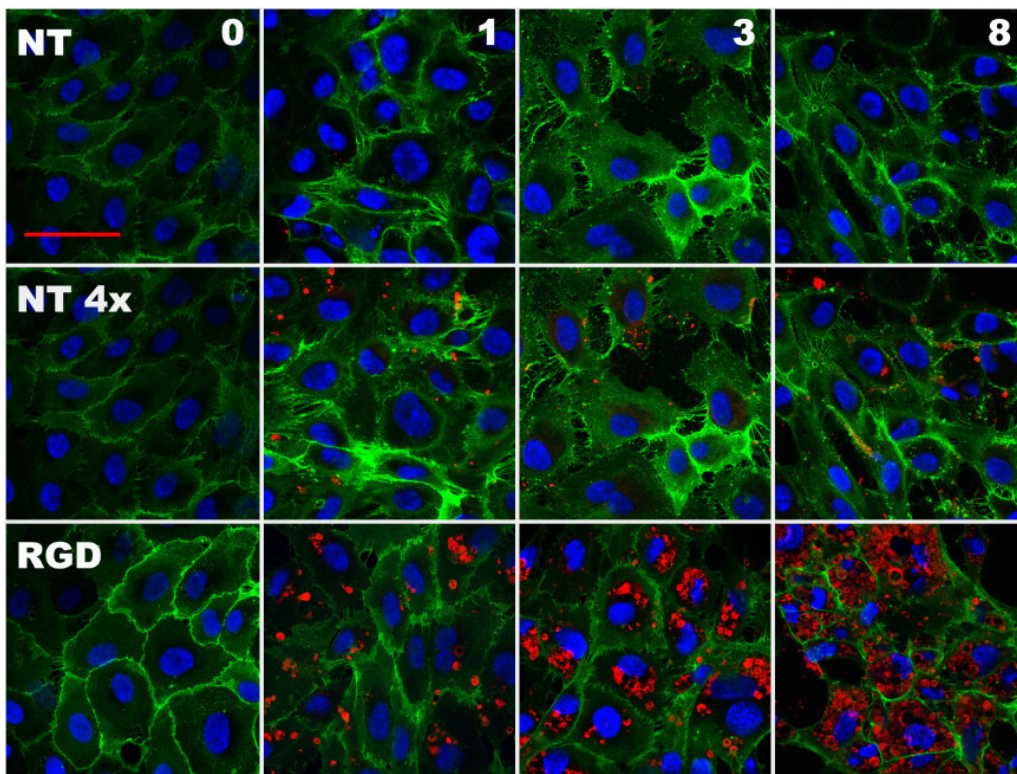


**Figure 2, CLSM images of HUVECs incubated with RGD-emulsion (RGD) or NT-emulsion (NT), with green = CD31, red = rhodamine, blue = DAPI. The red scale bar equals 50  $\mu\text{m}$ . The numbers in the top right corners are the incubation times in hours. The laser intensity used to obtain the images labeled NT 4x (middle row) was fourfold higher than the intensity used to obtain the other images (bottom and top rows).**

Uptake of emulsions was quantified using a combination of techniques, *i.e.* FACS analysis, absolute gadolinium content determinations as well as  $^{19}\text{F}$  MRS. Targeting the  $\alpha_v\beta_3$ -integrin by RGD-peptide resulted in higher uptake of emulsion. Figure 3A shows the mean fluorescence intensity (MFI) of rhodamine-PE per cell from FACS analysis as a function of incubation time,



which revealed that the MFI of cells with RGD-emulsion was at least a factor 4 higher than that of cells with NT-emulsion. For pellets of HUVECs incubated with RGD-emulsion, the absolute concentration of gadolinium increased from 0.10 mM after 0.5 hr to 0.39 mM after 8 hr of incubation (Figure 3B). Uptake of NT-emulsion was much lower, with gadolinium concentration varying from 0.02 mM after 0.5 hr to 0.06 mM after 8 hr of incubation. In Figure 3C, the  $^{19}\text{F}$  MRS PFCE peak area is plotted as a function of incubation time. Peak area for HUVECs incubated with RGD-emulsion was at least six fold higher than with NT-emulsion for all incubation times.

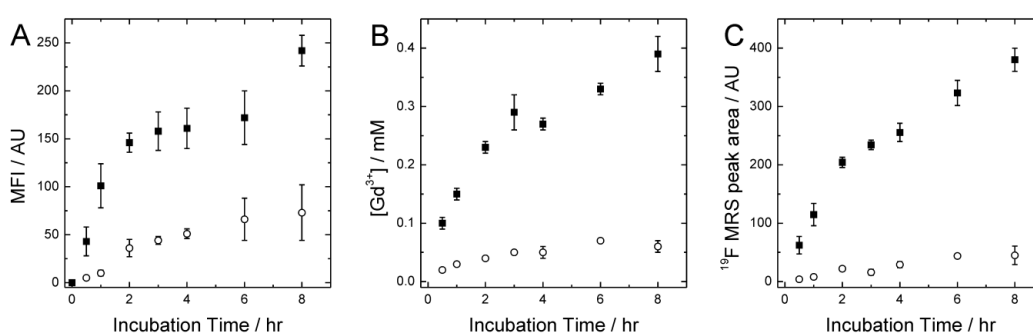


**Figure 3, Nanoparticle uptake assessed by FACS, quantitative Gd determinations and  $^{19}\text{F}$  MRS as function of incubation time for RGD-emulsion (solid squares) and NT-emulsion (open circles). (A) Mean fluorescence intensity per cell (MFI). (B) Gadolinium concentration. (C)  $^{19}\text{F}$  MRS peak area. Data are mean  $\pm$  SD (n=3).**

RGD- and NT-emulsion displayed different proton longitudinal and transversal relaxivities in the cell pellets. Figure 4A shows  $R_{1,H}$  of the pellets as a function of the gadolinium concentration. For HUVECs incubated with RGD-emulsion, the  $R_{1,H}$  increased from a pre-incubation value of  $0.49 \text{ s}^{-1}$  to  $0.87 \text{ s}^{-1}$  after 8 hr of incubation. For HUVECs incubated with NT-emulsion,  $R_{1,H}$  increased from  $0.49 \text{ s}^{-1}$  to  $0.65 \text{ s}^{-1}$  with a steeper slope than was the case for incubations with RGD-emulsion. The longitudinal relaxivity ( $r_{1,H}$ ) was determined by linear fittings of  $R_{1,H}$  versus the concentration of gadolinium, using the least squared method, resulting in  $r_{1,H} = 1.1 \pm 0.1 \text{ mM}^{-1}\text{s}^{-1}$  and  $2.6 \pm 0.4 \text{ mM}^{-1}\text{s}^{-1}$  for cells incubated with RGD- and NT-emulsion, respectively. Transverse relaxation rates ( $R_{2,H}$ ) versus the concentration of gadolinium are plotted in Figure 4B. For HUVECs incubated with RGD-emulsion  $R_{2,H}$  ranged from  $28.3 \text{ s}^{-1}$  for non-incubated cells to  $37.4 \text{ s}^{-1}$  for 8 hr incubated cells. Incubation of HUVECs with NT-emulsion did not result in a significant change in  $R_{2,H}$ . The transverse relaxivity ( $r_{2,H}$ ) was determined by linear fitting of the  $R_{2,H}$  as a function of the concentration of gadolinium, which resulted in  $r_{2,H} = 31 \pm 4 \text{ mM}^{-1}\text{s}^{-1}$  for the RGD-emulsion. Scatter in the data prevented accurate determination of the proton transverse relaxivity of HUVECs incubated with NT-emulsion.

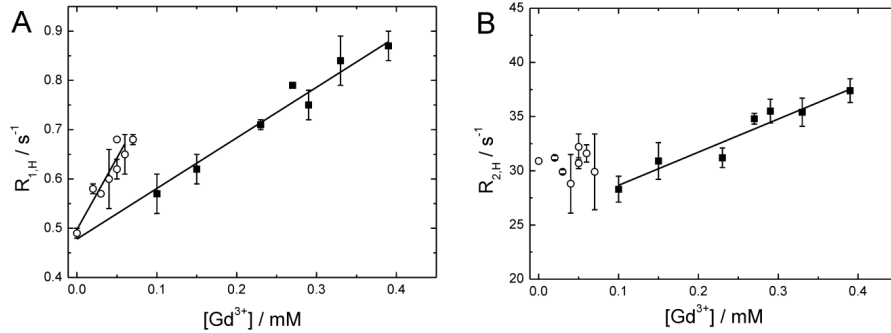


**Figure 4, Proton relaxation rates as function of gadolinium concentration in the cell pellets, for RGD-emulsion (solid squares) and NT-emulsion (open circles). (A) Longitudinal proton relaxation rate  $R_{1,H}$ . Solid lines are linear fits to the experimental data resulting in  $r_{1,H} = 1.1 \pm 0.1 \text{ mM}^{-1}\text{s}^{-1}$  and  $r_{1,H} = 2.6 \pm 0.4 \text{ mM}^{-1}\text{s}^{-1}$  for incubations with RGD- and NT-emulsions, respectively. (B) Transversal proton relaxation rate  $R_{2,H}$ . The solid line is a linear fit to the experimental data resulting in  $r_{2,H} = 31.1 \pm 3.9 \text{ mM}^{-1}\text{s}^{-1}$  for RGD-emulsion incubated HUVECs. Data are mean  $\pm$  SD ( $n=3$ ).**

The emulsions exhibited different behavior for the fluorine longitudinal and transversal relaxation rates in the cell pellets. Figure 5A shows the fluorine longitudinal relaxation rate  $R_{1,F}$  as a function of nanoparticle concentration in the cell pellet.  $R_{1,F}$  was essentially constant with nanoparticle concentration and equaled the fluorine longitudinal relaxation rate observed for both RGD- and NT-emulsion in aqueous solution (solid line:  $R_{1,F} = 1.23 \pm 0.5 \text{ s}^{-1}$ ). In sharp contrast, the fluorine transversal relaxation rate in the cell pellets (Figure 5B) was significantly lower than in aqueous solution (solid line:  $R_{2,F} = 74 \pm 1 \text{ s}^{-1}$ ) and  $R_{2,F}$  increased with increasing nanoparticle concentration.

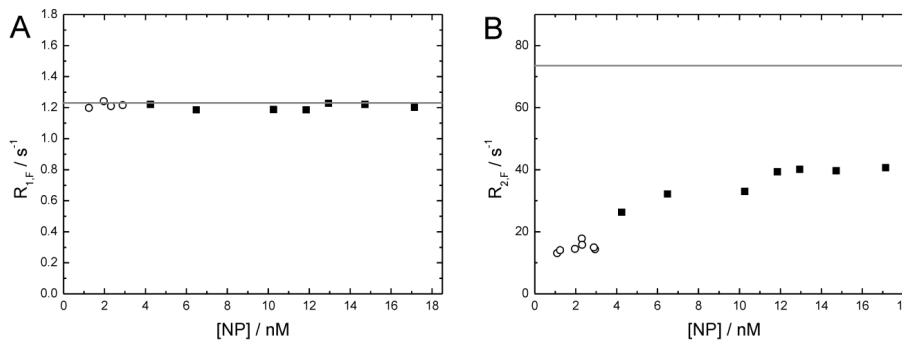


**Figure 5, Fluorine relaxation rates as function of nanoparticle concentrations in the cell pellets, for RGD-emulsion (solid squares) and NT-emulsion (open circles). (A) Longitudinal fluorine relaxation rate  $R_{1,F}$ . (B) Transversal fluorine relaxation rate  $R_{2,F}$ . The solid lines are  $R_{1,F}$  and  $R_{2,F}$  measured for RGD- and NT-emulsions in aqueous solution.**

In order to gain some insight in the structural integrity of the emulsion upon exposure to and internalization in the endothelial cells, the Gd to  $^{19}\text{F}$  ratio (nmol/ $\mu\text{mol}$ ) was evaluated as a function of the estimated nanoparticle concentration in the cell pellets (Figure 6). Particularly for low concentrations of NT-emulsion, the Gd to  $^{19}\text{F}$  ratio was not constant and was significantly higher than the ratio in the starting material (solid line:  $\text{Gd}/^{19}\text{F} = 0.24 \pm 0.01$ ).

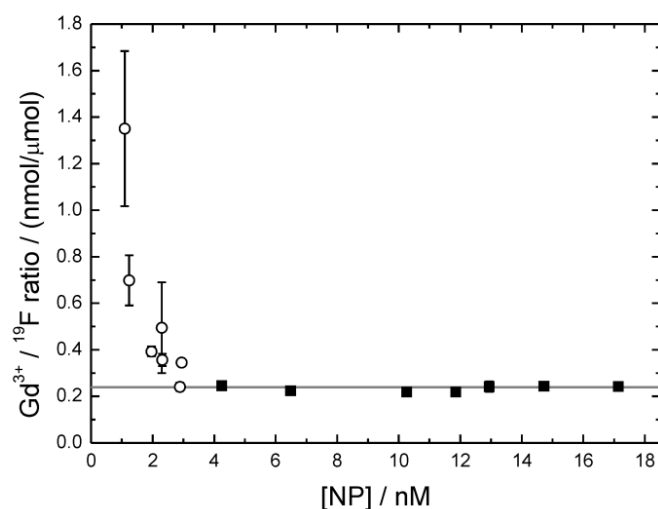


**Figure 6, Gadolinium to fluorine ratio (nmol/ $\mu\text{mol}$ ) as a function of the nanoparticle concentration in the cell pellets for RGD-emulsion (solid squares) and NT-emulsion (open circles). The solid line is the gadolinium to fluorine ratio measured for RGD- and NT-emulsions in aqueous solution. Data are mean  $\pm$  SD ( $n=3$ ).**

Linearity of the  $^1\text{H}$  MRI and  $^{19}\text{F}$  MRI CNR, as well as the normalized  $^{19}\text{F}$  MRS peak areas with nanoparticle concentration in the cell pellets, which is a premise for absolute quantification, is addressed in Figure 7. The  $^1\text{H}$  MRI CNRs for both RGD- and NT-emulsions (Figure 7A) were fairly linear with nanoparticle concentration ( $R^2 = 0.96$  and  $R^2 = 0.75$ , respectively). However, NT- and RGD-emulsion displayed a different slope, due to different intracellular relaxivity, complicating the distinction between non-targeted and targeted uptake. The  $^1\text{H}$  MRI detection thresholds were 10.2 and 2.2 nM nanoparticles, or 0.23 and 0.05 mM Gd, for RGD- and NT-emulsions, respectively. The  $^{19}\text{F}$  MRI CNR for the RGD-emulsion (Figure 7B) was quite linear with nanoparticle concentration ( $R^2 = 0.97$ ) in the measured nanoparticle concentration range. For the NT-emulsion the  $^{19}\text{F}$  MRI CNR remained below 5 throughout the experiment, however, and therefore could not be determined reliably. The  $^{19}\text{F}$  MRI detection threshold for RGD-emulsion was 2.1 nM nanoparticles or

200 mM  $^{19}\text{F}$ . The  $^{19}\text{F}$  MRS peak area (Figure 7C), normalized to the pellet volume and corrected for differences in  $R_{2,F}$ , was highly linear with nanoparticle concentration ( $R^2 = 0.99$ ; data for RGD- and NT-emulsions fitted together). The  $^{19}\text{F}$  MRS detection threshold was 0.3 nM nanoparticles or 27 mM  $^{19}\text{F}$ .

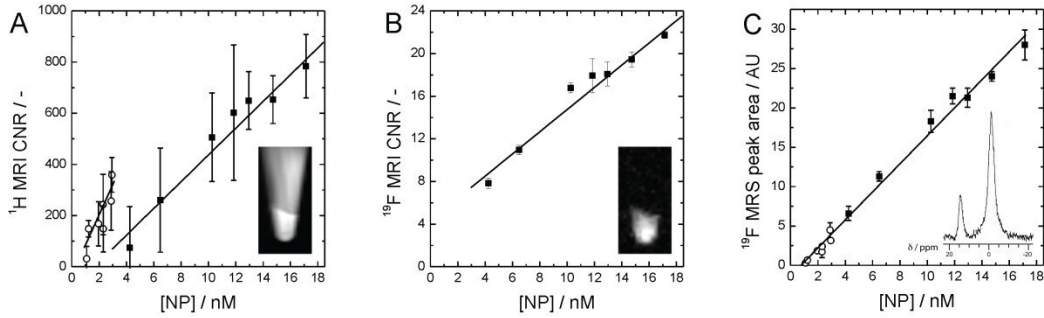


**Figure 7, Quantitative proton and fluorine MRI and MRS readouts as function of nanoparticle concentrations in the cell pellets for RGD-emulsion (solid squares) and NT-emulsion (open circles). (A)  $^1\text{H}$  MRI CNR. The inset is a  $T_1$ -weighted  $^1\text{H}$  MR image of an Eppendorf tube containing a cell pellet with RGD-emulsion. (B)  $^{19}\text{F}$  MRI CNR. The inset is a  $^{19}\text{F}$  MR image of an Eppendorf tube containing a cell pellet with RGD-emulsion. (C)  $^{19}\text{F}$  MRS peak area, normalized to the pellet volume. The inset shows  $^{19}\text{F}$  spectrum with (left) reference TFA peak and (right) perfluoro-15-crown-5-ether peak. Solid lines are linear fits to the data. Data are mean  $\pm$  SD ( $n=3$ ).**

### Discussion and Conclusions

In this study we set out to investigate the consequences of cellular internalization on the relaxometric properties and MR quantification potential of a fluorine-containing emulsion. A model system was used, consisting of an *in vitro* culture of human endothelial cells. Cellular internalization was achieved by targeting the cell-internalizing  $\alpha_v\beta_3$ -integrin receptor with cyclic RGD-peptide. Several readouts ascertained efficient targeting of the RGD-emulsion, in agreement with previous *in vivo* findings [28-30].

As anticipated, quantification using proton MRI proved complex. Although the  $^1\text{H}$  MRI CNR for RGD- and NT-emulsions was essentially linear with nanoparticle concentrations, the slopes were different for the two emulsion types, hindering unambiguous concentration quantification. The reason for these different slopes, as a consequence of different longitudinal relaxivities, can be found in the intracellular confinement of the cell-internalized emulsion. NT-emulsion ended up in small 3-4  $\mu\text{m}$  diameter intracellular vesicles, whereas RGD-emulsion in larger 4-8  $\mu\text{m}$  diameter vesicles. The lower surface to volume ratio of the larger vesicles is associated with a lower water exchange rate across the vesicle membrane, leading to a lower effective relaxivity – an effect coined relaxivity quenching, observed previously for cyclic RGD-conjugated liposomes as well in Chapter 2 and 3.

For the fluorine MRI and MRS signals water exchange rates obviously play no role and therefore quantification, *i.e.* linearity with fluorine concentration, is generally considered straightforward. However, intracellular confinement could still be of importance, when this leads to changes in the fluorine longitudinal and transversal relaxation rates as a result of altered diffusional and translational dynamics or cellular processing and breakdown of the emulsion. Interestingly, we observed that the fluorine longitudinal relaxation rate was not influenced by cellular internalization, whereas the transversal relaxation rate was consistently lower in the cells and concentration dependent. The mechanism responsible for the observed changes in  $R_{2,F}$  is not completely clear, though it seems related to the presence of Gd-DOTA-DSPE lipid in the emulsion membrane, as changing  $R_{2,F}$  with varying Gd-lipid content in the emulsion membrane was observed previously [31]. One could consider a scenario in which the Gd-DOTA-DSPE lipids become separated from the fluorine core by lipid exchange with the cell membrane upon exposure to and internalization into the cells. The emulsion, stripped of Gd-DOTA-DSPE, would exhibit significantly lower transversal relaxation rates because of reduced magnetic susceptibility induced  $T_2$  shortening, which would be of less influence on the longitudinal relaxation rate, particularly at high magnetic field strength (6.3 T). Indeed, the varying Gd to

$^{19}\text{F}$  ratio observed for emulsions in the cells is a strong indicator for the existence of such lipid exchange between cell and emulsion. The Gd to  $^{19}\text{F}$  ratio deviated from the value found for emulsion in aqueous solution mostly in the low Gd concentration range (Figure 6), which suggests that this was caused by transfer of Gd-DOTA-DSPE from emulsion to the cells upon initial exposure to the cell culture, rather than originating from differences in Gd and  $^{19}\text{F}$  cellular excretion rates.

In this paper, the MR quantification potential of nanoparticle concentration was addressed using proton and fluorine MRI as well as fluorine MRS. For  $^1\text{H}$  MRI and  $^{19}\text{F}$  MRI a gradient-spoiled FLASH sequence was used. Although the choice for this sequence was rather arbitrary, both  $^1\text{H}$  MRI and  $^{19}\text{F}$  MRI were performed with near identical acquisition parameters and the excitation flip angle of the FLASH acquisition was optimized as to yield the best possible SNR per unit time, allowing for a fair comparison of the CNRs. The CNR for  $^1\text{H}$  MRI was highest, although it suffered from a high standard deviation, which was a consequence of variations in baseline SNR between different incubation runs ( $n = 3$ ).  $^{19}\text{F}$  MRI has a clear advantage here, since baseline  $^{19}\text{F}$  signal is absent.  $^1\text{H}$  MRI CNR versus nanoparticle concentration resulted in different linear slopes for RGD- and NT-emulsions, prohibiting unambiguous quantification of nanoparticle concentration. Nevertheless, the high CNR and low detection threshold enable high-resolution *in vivo* imaging of nanoparticle distributions in an anatomical context as has been demonstrated in various previous studies [32, 33].  $^{19}\text{F}$  MRI yielded linear CNR with nanoparticle concentration, which demonstrates that fluorine imaging is quantitative even in the situation when nanoparticles are internalized into cells and exposed to the rather hostile environment of the endosomal vesicles. Changes in the  $^{19}\text{F}$  transversal relaxation rates upon internalization should be considered by using an appropriate  $T_2$ -insensitive sequence. The  $^{19}\text{F}$  MRS normalized peak area was linear with nanoparticle concentration after correction for differences in  $R_{2,F}$ , with similar slopes for RGD- and NT-emulsions and the detection threshold was lowest. For absolute quantification of nanoparticle concentration the  $^{19}\text{F}$  MRS approach is therefore most suitable.

In conclusion, we have investigated the changes in proton and fluorine MR relaxometric properties of paramagnetic perfluorocarbon emulsions internalized in human endothelial cells and potential consequences for the MR-based quantification potential of local nanoparticle concentration. For the investigated nanoparticle concentration range (up to approximately 17 nM), proton longitudinal relaxation rates and MRI CNRs were linear with nanoparticle concentration, however different for non-targeted and targeted emulsion types.

Upon internalization into the endothelial cells the fluorine longitudinal relaxation rates were found to remain constant, but the fluorine transversal relaxation rate was lower than for emulsion in aqueous solution and increased with increasing nanoparticle concentration. Nevertheless, by using a suitable  $T_2$ -insensitive MRI sequence or corrections for differences in fluorine transversal relaxation rates, the fluorine signals were observed to be linear with concentration in the pellets allowing for absolute quantification of nanoparticle concentration.

## Literature

1. Weissleder, R., *Science*, 2006. **312**(5777): p. 1168-1171.
2. Sanz, J., Z.A. Fayad, *Nature*, 2008. **451**(7181): p. 953-957.
3. Jaffer, F.A., D.E. Sosnovik, M. Nahrendorf, *et al.*, *J Mol Cell Cardiol*, 2006. **41**(6): p. 921-933.
4. Modo, M., K. Mellodew, D. Cash, *et al.*, *Neuroimage*, 2004. **21**(1): p. 311-317.
5. Shyu, W.C., C.P. Chen, S.Z. Lin, *et al.*, *Stroke*, 2007. **38**(2): p. 367-374.
6. Kustermann, E., W. Roell, M. Breitbach, *et al.*, *NMR Biomed*, 2005. **18**(6): p. 362-370.
7. Yeh, T.C., W. Zhang, S.T. Ildstad, *et al.*, *Magn Reson Med*, 1995. **33**(2): p. 200-208.
8. Brekke, C., S.C. Williams, J. Price, *et al.*, *Neuroimage*, 2007. **37**(3): p. 769-782.
9. Nasongkla, N., E. Bey, J. Ren, *et al.*, *Nano Lett*, 2006. **6**(11): p. 2427-2430.
10. Viglianti, B.L., A.M. Ponce, C.R. Michelich, *et al.*, *Magn Reson Med*, 2006. **56**(5): p. 1011-1018.
11. Du, W., Z. Xu, A.M. Nystrom, *et al.*, *Bioconj Chem*, 2008. **19**(12): p. 2492-2498.
12. Langereis, S., J. Keupp, J.L. van Velthoven, *et al.*, *J Am Chem Soc*, 2009. **131**(4): p. 1380-1381.
13. Partlow, K.C., G.M. Lanza, S.A. Wickline, *Biomaterials*, 2008. **29**(23): p. 3367-3375.
14. Morawski, A.M., P.M. Winter, K.C. Crowder, *et al.*, *Magn Reson Med*, 2004. **51**(3): p. 480-486.
15. Morawski, A.M., P.M. Winter, X. Yu, *et al.*, *Magn Reson Med*, 2004. **52**(6): p. 1255-1262.
16. Kimura, A., M. Narazaki, Y. Kanazawa, *et al.*, *Magn Reson Imaging*, 2004. **22**(6): p. 855-860.
17. Srinivas, M., P.A. Morel, L.A. Ernst, *et al.*, *Magn Reson Med*, 2007. **58**(4): p. 725-734.
18. Fogel, U., Z. Ding, H. Hardung, *et al.*, *Circulation*, 2008. **118**(2): p. 140-148.
19. Srinivas, M., M.S. Turner, J.M. Janjic, *et al.*, *Magn Reson Med*, 2009. **62**(3): p. 747-753.
20. Ruiz-Cabello, J., P. Walczak, D.A. Kedziorek, *et al.*, *Magn Reson Med*, 2008. **60**(6): p. 1506-1511.
21. Ahrens, E.T., R. Flores, H. Xu, *et al.*, *Nat Biotechnol*, 2005. **23**(8): p. 983-987.
22. Partlow, K.C., J. Chen, J.A. Brant, *et al.*, *FASEB J*, 2007. **21**(8): p. 1647-1654.
23. Janjic, J.M., M. Srinivas, D.K. Kadayakkara, *et al.*, *J Am Chem Soc*, 2008. **130**(9): p. 2832-2841.
24. Janjic, J.M., E.T. Ahrens, *Wiley Interdiscip Rev Nanomed Nanobiotechnol*, 2009. **1**(5): p. 492-501.
25. Venkataramani, D., Chen, J., Neubauer, A.M., Crowder, Brant, J., Lanza, G.M., Wickline, S.A., *Proc. Intl. Soc. Mag. Reson. Med.*, 2006. **14**: p. 1890.
26. Hak, S., H.M. Sanders, P. Agrawal, *et al.*, *Eur J Pharm Biopharm*, 2009. **72**(2): p. 397-404.
27. Rouser, G., S. Fkeischer, A. Yamamoto, *Lipids*, 1970. **5**(5): p. 494-496.
28. Mulder, W.J., G.J. Strijkers, J.W. Habets, *et al.*, *Faseb J*, 2005. **19**(14): p. 2008-2010.
29. Schmieder, A.H., S.D. Caruthers, H. Zhang, *et al.*, *FASEB J*, 2008. **22**(12): p. 4179-4189.
30. Winter, P.M., S.D. Caruthers, A. Kassner, *et al.*, *Cancer Res*, 2003. **63**(18): p. 5838-5843.
31. Neubauer, A.M., J. Myerson, S.D. Caruthers, *et al.*, *Magn Reson Med*, 2008. **60**(5): p. 1066-1072.
32. Mulder, W.J., K. Castermans, J.R. van Beijnum, *et al.*, *Angiogenesis*, 2009. **12**(1): p. 17-24.
33. Pan, D., G.M. Lanza, S.A. Wickline, *et al.*, *Eur J Radiol*, 2009. **70**(2): p. 274-285.





## Chapter **7**

### **A multimodal liposome for combined SPECT, MR and fluorescence imaging**

**Based on:**

*A multimodal liposome for combined SPECT, MR and fluorescence imaging*

M.B. Kok, A. de Vries, H.M.H.F. Sanders, G. J. Strijkers, H. Gröll and K. Nicolay

In preparation

### **Abstract**

A new and exciting development in the field of medical imaging is the development of hybrid scanners, in which two modalities are combined in a single setup for simultaneous dual-modality imaging. In the late '90s, the combination of positron emission tomography (PET) and computed tomography (CT) was introduced into the clinic in which the high sensitivity of PET was combined with the high resolution anatomical overlay provided by CT. The design of such PET/CT instruments, however, involves two separate back-to-back devices, in which the patient table is moved from one scanner to the other. Presently, truly integrated systems are being developed that combine either PET or SPECT (single photon emission computed tomography) with magnetic resonance imaging (MRI). This approach allows imaging and quantification using the high sensitivity of the nuclear techniques and the exploitation of the high spatial resolution and enormous versatility of MRI. Dual modality imaging would greatly benefit from the development of multimodal probes that can be detected by both techniques. Here we report on the development of a multimodal contrast agent for combined SPECT/MRI imaging. The liposomal contrast agent contains an  $^{111}\text{In}$  label for SPECT and gadolinium-chelates for MRI contrast, creating a platform for simultaneous quantification (based on SPECT) and precise spatial localization (based on MRI) using a single probe. To explore the utility of the liposomal probe, incubations were done with human umbilical vein derived endothelial cells (HUVECs) and cell samples were analyzed using MRI, SPECT/CT,  $\gamma$ -counting, confocal laser scanning microscopy (CLSM) and inductively coupled plasma mass spectrometry (ICP-MS). It was found that the radiolabel allowed accurate quantification of cell-internalized probe using  $\gamma$ -counting.

## Introduction

Molecular imaging can be defined as the *in vivo* characterization and measurement of biologic processes at the cellular and molecular level. To aid in our understanding of these often complex processes, many different imaging modalities are available such as positron emission tomography (PET), single photon emission computed tomography (SPECT), magnetic resonance imaging (MRI), optical imaging, computed tomography (CT) and ultrasound (US). Each modality has its advantages and disadvantages [1]. MRI, for instance is the modality of choice when it comes to high resolution anatomical images (typically 0.1-0.5 mm for clinical scanners), with high soft tissue contrast. However, MRI has a low sensitivity to contrast agents (sub-mM range). PET, on the other hand, has an extremely high sensitivity (pM range) but its resolution is poor (typical 2-10 mm). Unfortunately, no imaging modality is able to provide a high spatial resolution in combination with high sensitivity and large field-of-view.

The solution to this problem is dual modality imaging, in which the strengths of two imaging modalities are united within one device [2]. One such example is PET/CT that was introduced in the clinic in the late '90s [3], and in which the high sensitivity of PET is combined with a high resolution anatomical overlay provided by CT. Recently, also PET-MRI has come to the attention due to its combination of high sensitivity (PET) with high spatial resolution and enormous versatility (MRI) [4, 5]. MRI is favored over CT since it can provide images with a high spatial resolution without exposure to radiation, as well as functional information such as diffusion, magnetic resonance spectroscopy (MRS) and functional MRI (fMRI). In addition, PET-MRI is able to acquire its images simultaneously instead of sequential as is the case with PET-CT. As a result, registration errors are minimized and acquisition time for PET-MRI is decreased [2]. The introduction of PET-MRI however is still under development due to difficulties with design of magnetic field-insensitive PET detectors within the magnet of the MRI system. SPECT-MRI has similar advantages as PET-MRI. However, SPECT isotopes have longer decay times compared to PET isotopes and are therefore more favorable in studies where a long pharmaceutical preparation is needed, or when the *in vivo* accumulation in the target tissue takes more time, as is the case for antibody targeting which can take up to several days. Dual modality imaging will greatly benefit from the use of dual modality imaging probes that can be visualized by both techniques. Probes for nuclear techniques in combination with optical imaging have been investigated by Schipper *et al.* [6], who developed <sup>67</sup>Cu-labeled quantum dots and Yang *et al.* who demonstrated the use of near-infrared fluorescent, <sup>111</sup>Indium-labeled polymeric micelles [7]. Furthermore, Lijowski *et al.* [8] developed an emulsion targeted to the  $\alpha_v\beta_3$ -integrin that was labeled with both an MR label and a

SPECT label. An initial injection with radiolabeled contrast agent allowed SPECT/CT imaging. However, an additional higher dose of MR labeled contrast agent was needed to obtain contrast enhancement on MR images. The most developed dual modality imaging concept is however the combination of MRI with optical imaging. Relatively small molecules have been synthesized as dual-modality probes, such as a Gd-DO3A covalently linked to fluorescein [9] or a small peptide chain functionalized with DTPA and the organic dye Oregon Green 488 [10]. Nanoparticles such as liposomes [11], quantum dots [12], superparamagnetic iron oxide nanoparticles [13], or zeolite nanoparticles [14] also offer the opportunity to combine several imaging modalities.

Previously, we have shown that quantification of the receptor-mediated uptake of paramagnetic gadolinium-containing nanoparticles, using  $^1\text{H}$  MRI is very challenging since internalization dramatically influences the efficacy of the MR contrast agent (Chapter 2 and 3). Here we report on the development of a multimodal contrast agent by combining SPECT with MRI using an  $^{111}\text{In}$  labeled gadolinium based MR liposomal contrast agent, that creates a platform allowing simultaneous quantification (based on SPECT) and precise spatial localization (based on MRI) using a single probe. To validate whether quantification and imaging is feasible, the contrast agent was incubated with human umbilical vein derived endothelial cells (HUVECs). Cell samples were analyzed using MRI, SPECT/CT,  $\gamma$ -counting, confocal laser scanning microscopy (CLSM) and inductively coupled plasma mass spectrometry (ICP-MS).

## Methods

### Materials

1,2-Distearoyl-*sn*-glycero-3-phosphocholine (DSPC), cholesterol, 1,2-distearoyl-*sn*-glycero-3-phosphoethanolamine-N-[methoxy(polyethyleneglycol)-2000] (PEG<sub>2000</sub>-DSPE), 1,2-distearoyl-*sn*-glycero-3-phosphoethanolamine-N-[maleimide(polyethyleneglycol)-2000] (Mal-PEG<sub>2000</sub>-DSPE) and 1,2-dipalmitoyl-*sn*-3-phosphoethanolamine-N-[lissamine rhodamine B sulfonyl] (rhodamine-PE) were obtained from Avanti Polar Lipids (Alabaster, AL, USA). 1,2-distearoyl-*sn*-glycero-3-phosphoethanolamine-[tetraazacyclododecane tetraacetic acid] (Gd-DOTA-DSPE) and DOTA-DSPE were purchased from SyMO-Chem (Eindhoven, The Netherlands). Endothelial Growth Medium-2 (EGM-2) and human umbilical vein derived endothelial cells (HUVECs) were ordered with Lonza Bioscience (Switzerland). Monoclonal mouse anti-human CD31 antibody was obtained from Dakocytomation (Glostrup, Denmark). Alexa Fluor 488 conjugated goat anti-mouse secondary antibody was from Molecular Probes Europe BV (Leiden, The Netherlands). Cyclic RGD, c(RGDf(-S-acetylthioacetyl)K) was synthesized by Ansynth Service BV (Roosendaal, The Netherlands). All other chemicals were obtained from Sigma (St. Louis, MO, USA) and were of analytical grade or the best grade available.

### Liposome preparation and characterization

200 nm-diameter liposomes containing Gd-DOTA-DSPE, DOTA-DSPE, DSPC, cholesterol, PEG<sub>2000</sub>-DSPE and Mal-PEG<sub>2000</sub>-DSPE at a molar ratio of 0.72/0.03/1.10/1/0.075/0.075 were produced by lipid film hydration and extrusion according to Mulder *et al.* [15]. In short, the lipids were dissolved in a 1:5 methanol:chloroform mixture. As a fluorescent marker, 0.1 mole percent of rhodamine-PE was added. A lipid film was created by evaporating the methanol/chloroform mixture using a Rotavapor R200 (Buchi, Flawil, Switzerland). The lipid film was hydrated at 67 °C using a HEPES buffered saline solution (HBS), containing 20 mM HEPES and 135 mM NaCl (pH 6.7). The lipid suspension was extruded at 67 °C, twice through a single 200 nm polycarbonate membrane (Whatman, Kent, UK) and 6 times through a double 200 nm polycarbonate membrane. After extrusion, half of the liposome suspension was modified with a cyclic RGD-peptide (6 µg/µmol total lipid) to target the  $\alpha_v\beta_3$ -integrin. The cyclic RGD-peptide was deacetylated and coupled to the distal end of Mal-PEG<sub>2000</sub>-DSPE. After incubation overnight, at 4 °C, both batches of liposomes were centrifuged at 310,000 g for 45 min. Centrifugation was needed, in case of RGD-liposomes, to remove unconjugated RGD-peptide. The pellets were resuspended in HBS, pH 7.4. Lipid concentration was measured by phosphate determination according to Rouser *et al.* [16]. Size and polydispersity index (PDI) of the liposomes were determined with dynamic light

scattering (DLS) (Zetasizer Nano, Malvern, UK). Both the longitudinal and transverse relaxivity were determined at 6.3 T (20°C) by fitting  $R_1$  ( $1/T_1$ ) and  $R_2$  ( $1/T_2$ ) values as a function of the gadolinium concentration of the liposome suspension as determined using inductively coupled plasma atomic mass spectroscopy (ICP-MS) by Philips Research (Eindhoven, The Netherlands), using the least squares method. In the remainder of this paper we refer to liposomes that were conjugated with RGD as RGD-liposomes. Non-targeted liposomes that were not conjugated with a targeting ligand will be referred to as NT-liposomes.

#### <sup>111</sup>Indium Labeling

RGD-liposomes and NT-liposomes were labeled with <sup>111</sup>Indium (Perkin Elmer, Boston, Ma, USA). In detail, 100  $\mu$ L ammonium acetate buffer (2M NH<sub>4</sub>OAc, pH 4.5) was added to a 2.6 mL liposomal solution together with 25  $\mu$ L of <sup>111</sup>Indium (25 MBq) and the pH was adjusted to 5.0. The sample was stirred at 50 °C for 90 min. Free DTPA (10  $\mu$ L, 10 mM) was added to the reaction mixture for 15 min to scavenge free radionuclides. Labeling efficiency was checked on silica TLC using 200 mM EDTA as mobile phase and analyzed using a Phosphor Imager (FLA-7000, Fujifilm, Tokyo, Japan). Radiochemical purities obtained were > 95% for the RGD-liposomes as well as the NT-liposomes.

#### Cell Culture:

Human umbilical vein derived endothelial cells (HUVECs) were used for all the experiments. Cells were stored in liquid nitrogen upon arrival. Before use, the cells were quickly thawed in a water bath (T= 37 °C) and divided over 2 gelatin coated T75 TCPS flasks (VWR, West Chester, PA, USA). Cells were cultured in a humidified incubator at 37 °C with 5% CO<sub>2</sub>. The EGM-2 medium was replaced every 2-3 days. Cells were subcultured at 80-90% confluency according to procedures provided by Lonza Bioscience (Switzerland).

#### Experimental Setup

Cells of passage 3 or 4 were used for all experiments at 80-90% confluency. Incubation was carried out on both gelatin-coated coverslips, for CLSM analysis, and in gelatin-coated T75 TCPS culture flasks, for MRI, FACS and ICP-MS analysis. Samples for CLSM were incubated with liposomes that were not labeled with <sup>111</sup>Indium. All measurements were done in triplicate for both types of liposomes and each incubation time. To start the experiment, medium was replaced by either RGD-liposome or NT-liposome containing medium at a concentration of 1.2  $\mu$ mol total lipid per mL. 4 mL of liposome containing medium was added to the T75 gelatin-coated TCPS flasks and 0.5 mL of medium was added to the gelatin-coated coverslips. The incubation time with liposomes containing medium was varied between 0 and 8 hr. After incubation,

the cells were washed three times with 5 mL prewarmed (37 °C) HEPES-buffered saline solution to remove non-adherent liposomes. After these washing steps, the cells grown on coverslips were fixed using 4% PFA for 15 min at room temperature. Cells in culture flasks were detached using 2 mL 0.25% trypsin 1 mM EDTA·4Na (Lonza Bioscience, Switzerland). The trypsin solution was neutralized using 4 mL trypsin neutralizing solution (Lonza Bioscience, Basel, Switzerland). Cells were spun down at 220 g and the supernatant was removed. The cell pellet was resuspended in 200  $\mu$ L 4% paraformaldehyde solution in PBS and transferred to a 300  $\mu$ L Eppendorf cup. A loosely-packed cell pellet was formed by centrifugation at 10 g for 5 min. The cell pellets were stored at room temperature in the dark.

#### Magnetic Resonance Imaging

The  $T_1$  and  $T_2$  relaxation times and the volume of the pellets were measured using a 6.3 T horizontal bore animal MR scanner (Bruker, Ettlingen, Germany). Samples were measured approximately 2 months after initial labeling. After this period the radioactivity was reduced to safe levels for handling. All measurements were carried out at room temperature. Longitudinal and transverse relaxation times were measured in a 3 cm diameter send and receive quadrature-driven birdcage coil (Rapid Biomedical, Würzburg, Germany). The Eppendorf tubes containing the loosely-packed cell pellets were placed in a custom made holder (4 tubes at a time) that was filled with HEPES buffered saline solution to facilitate shimming.  $T_1$  was measured using a fast inversion recovery segmented FLASH sequence with an echo time (TE) of 1.5 ms, a repetition time (TR) of 3.0 ms, a flip angle of 15°, and an inversion time (TI) ranging from 67 ms to 4800 ms in 80 steps. Overall repetition time was 20 s. Field of view (FOV) was 3x2.18 cm<sup>2</sup>, using a matrix size of 128x128, a slice thickness of 0.75 mm and 2 averages.  $T_2$  was measured using a multi-slice multi-echo sequence with TE ranging between 9 and 288 ms in 32 steps and a TR of 1000 ms. FOV was 3x2.2 cm<sup>2</sup>, slice thickness was 0.75 mm using a matrix size of 128x128. Number of averages was 4. From the images a  $T_1$ - and  $T_2$ -map were calculated using Mathematica (Wolfram Research Inc, Champaign, IL, USA).  $T_1$  and  $T_2$  of the different cell pellets were determined by selecting a region-of-interest within the pellet.  $T_1$ -weighted images were measured using a multi-slice spin-echo sequence with TE = 10.3 ms and TR = 500 ms. FOV was 3x2.18 cm<sup>2</sup>, slice thickness was 0.75 mm using a matrix size of 256x192. Number of averages was 1. The volume of the cell pellet was determined for each sample separately in a 0.7 cm diameter solenoid coil using a 3D FLASH sequence with TE = 3.2 ms, TR = 25 ms and a flip angle of 30°. FOV was 1.6x1.6x1.6 cm<sup>3</sup>, matrix size was 128x128x128. Number of averages was 1. A threshold value was determined manually to select the voxels inside the pellet,



which were multiplied by the voxel volume to obtain the total volume of the pellet. The concentration of gadolinium in each cell pellet was determined by dividing the gadolinium content by the pellet volume.

#### SPECT Imaging

Cell pellets were measured using the Bioscan nanoSPECT/CT system (Washington, USA). For the helical SPECT scan 48 projections were obtained with 960 seconds/projection using 20% windows centered at 171 keV and a 15% window centered at 245 keV. Subsequently, a helical CT scan was made for overlay using 45 keV, 177  $\mu$ A, 2000 ms, 360 projections, and a pitch of 1. After reconstruction voxel sizes were obtained of 1.2 mm<sup>3</sup> (SPECT) and 0.5 mm<sup>3</sup> (CT). Quantitative data on cellular uptake of <sup>111</sup>Indium was measured using a  $\gamma$ -counting wizard (Wizard 1480 3" Wallac counter, Perkin Elmer, Groningen, The Netherlands)

#### Confocal Laser Scanning Microscopy

After fixation, the coverslips with HUVECs incubated with liposomes were stained using a mouse anti-human CD31 antibody to visualize the cellular membrane. The cells were rinsed for 5 min with PBS followed by 60 min of incubation with the primary mouse anti-human CD31 antibody (1:40 dilution). Subsequently the cells were washed 3x 5 min with PBS followed by 30 min of incubation with a secondary Alexa Fluor 488 goat anti-mouse IgG antibody (1:200 dilution). The cells were washed 3x 5 min with PBS and the nuclei were stained for 5 min with DAPI. After staining of the nuclei the cells were rinsed 3x 5 min with PBS and subsequently mounted on a microscopy slide using Mowiol mounting medium. Confocal fluorescence images were recorded at room temperature on a Zeiss LSM 510 META system using a Plan-Apochromat<sup>®</sup> 63x/1.4 NA oil-immersion objective. Alexa Fluor 488 and rhodamine-PE were excited using the 488 and 543 nm line of a HeNe laser, respectively. The fluorescence emission of Alexa Fluor 488 was recorded with photomultiplier tubes (Hamamatsu R6357) after spectral filtering with a NFT 490 nm beamsplitter followed by a 500-550 nm bandpass filter. Rhodamine-PE emission was analyzed using the Zeiss Meta System in a wavelength range of 586-704 nm. DAPI staining of nuclei was visualized by two-photon excitation fluorescence microscopy performed on the same Zeiss LSM 510 system. Excitation at 780 nm was provided by a pulsed Ti:Sapphire laser (Chameleon<sup>™</sup>; Coherent, Santa Clara, CA, USA), and fluorescence emission was detected with a 395-465 nm bandpass filter. All experiments were combined in multitrack mode and acquired confocally.

## Results

### *Liposome characteristics*

To study the quantification potential of a dual modality SPECT/MRI contrast agent, liposomes were prepared that contained both an MR label and an empty chelate that could be used for labeling with  $^{111}\text{In}$ . After centrifugation, typical lipid concentrations of approximately 50 mM in the final liposome suspension were obtained. DLS showed a single peak in intensity mode with a z-average of 182 nm and 178 nm for RGD- and NT- liposomes, respectively. A poly dispersity index (PDI) of 0.18 for RGD-liposomes and 0.16 for NT-liposomes was found. High resolution cryo-TEM images (Figure 1) revealed spherical unilamellar vesicles, typical for liposomes. Besides spherical unilamellar structures also a few disk shaped micelles and multilamellar liposomes were observed. Longitudinal and transverse relaxivities, as indices of MRI contrast efficacy were determined at 6.3T and 20°C. Measurements showed  $r_1 = 2.7 \pm 0.1 \text{ mM}^{-1}\text{s}^{-1}$  and  $3.4 \pm 0.1 \text{ mM}^{-1}\text{s}^{-1}$ , and  $r_2 = 16.2 \pm 0.1 \text{ mM}^{-1}\text{s}^{-1}$  and  $16.1 \pm 0.1 \text{ mM}^{-1}\text{s}^{-1}$ , for RGD- and NT-liposomes, respectively. After labeling with  $^{111}\text{In}$  for SPECT and  $\gamma$ -counting, radiochemical purities were > 95% for the RGD-liposomes as well as the NT-liposomes.

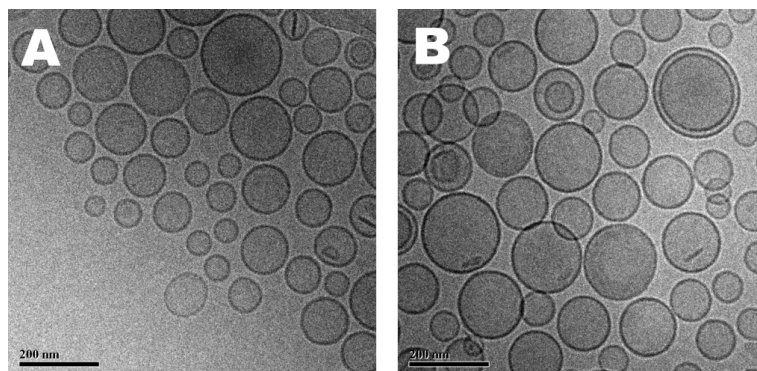


**Figure 1, Cryo-TEM images of (A) RGD-liposomes and (B) NT-liposomes. Bar = 200 nm.**

Association of the contrast agent with cultured HUVECs was investigated using ICP-MS,  $\gamma$ -counting, MRI and SPECT. Figure 2A shows the gadolinium concentration in cell pellets of HUVECs incubated with paramagnetic liposomes as a function of incubation time. A higher uptake of RGD-liposomes was found compared to NT-liposomes. For HUVECs incubated with RGD-liposomes, an increase in gadolinium content was observed up to 8 hr of incubation. In pellets of HUVECs incubated with RGD-liposomes, the concentration of gadolinium increased from 0.03 mM after 1 hr of incubation to 0.10 mM after 24 hr. For incubations with NT-liposomes, the gadolinium concentration was 0.02 mM after 1 hr of incubation. Thereafter, the concentration of gadolinium varied from 0.02

mM to 0.05 mM. The highest concentration of gadolinium was found after 7 hr of incubation. The uptake of NT-liposomes was approximately two times lower than that of RGD-liposomes.

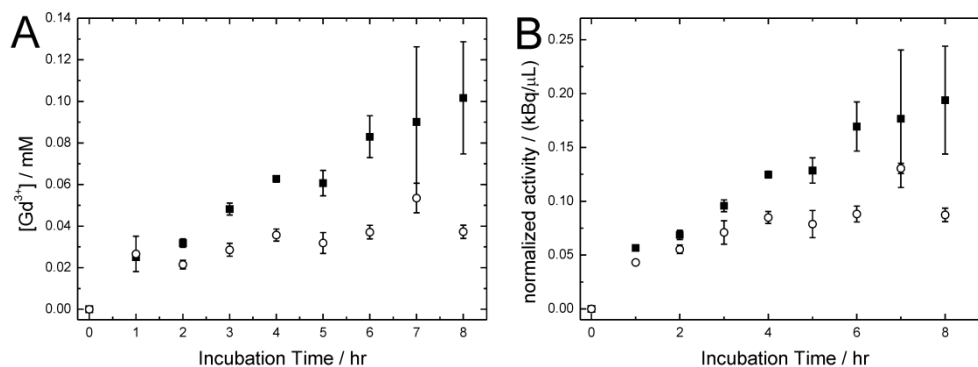


**Figure 2, Uptake of contrast agent. The concentration of gadolinium as measured by ICP-MS (A) and <sup>111</sup>Indium activity as measured by  $\gamma$ -counting normalized to pellet volume (B) as a function of time for HUVECs incubated with RGD-liposomes (solid squares) or NT-liposomes (open circles). Data represent mean  $\pm$  SD (n=3).**

The uptake of liposomes was also monitored using  $\gamma$ -counting.  $\gamma$ -counting was used, since the cell-pellets were too small for allowing quantification with SPECT imaging.  $\gamma$ -counting data was normalized to pellet volume and showed maximal uptakes of 0.19 and 0.13 kBq· $\mu$ L<sup>-1</sup> for HUVECs incubated with RGD- or NT-liposomes, respectively. The uptake of RGD-liposomes as measured by  $\gamma$ -counting was approximately two times higher than the uptake of NT-liposomes over the entire incubation experiment. Figure 3 shows overlaid SPECT/CT, SPECT and MRI images of pellets containing control HUVECs that were not incubated with contrast agent (left three panels), HUVECs that were incubated for 24 hr with NT-liposomes (middle three panels) or RGD-liposomes (right three panels). SPECT images show no signal for control HUVECs. A low SPECT signal was observed for HUVECs incubated with NT-liposomes for 24 hr. A bright signal was obtained for HUVECs incubated with RGD-liposomes. The merged SPECT/CT image nicely demonstrates that the nuclear signal originated from the bottom of the Eppendorf cup, where the cell pellet is located. T<sub>1</sub>-weighted MR images show that the pellet containing control HUVECs is essentially iso-intense with the medium above, whereas pellets containing NT- or RGD-incubated HUVECs can easily be distinguished as a consequence of the reduced T<sub>1</sub>. Incubation with RGD-liposomes led to higher MRI signal intensity of the cell pellet than incubations with NT-liposomes.

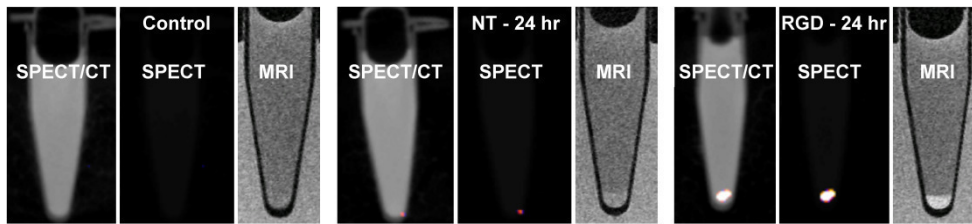


**Figure 3, Combined SPECT/CT, SPECT and  $T_1$ -weighed MRI images of pellets of control HUVECs without contrast agent (left panels), pellets of HUVECs incubated for 24 hr with NT-liposomes (middle panels) and RGD-liposomes (right panels). The pellets are situated at the bottom of the Eppendorf cups.**

The cellular location of the liposomal contrast agent was determined using confocal laser scanning microscopy (CLSM), by exploiting the rhodamine-PE present in the bilayer of the liposomes. Figure 4 shows confocal images of HUVECs grown on gelatin coated coverslips. Both RGD- and NT-liposomes accumulated in the perinuclear region. However, clear differences in uptake between RGD- and NT-liposomes were observed. Up to 8 hr of incubation, both the RGD- and NT-liposomes were mainly found in sharply delineated spherical 0.4-1.0  $\mu\text{m}$  diameter structures. For HUVECs incubated with RGD-liposomes, also larger structures with a diameter of 1-2  $\mu\text{m}$  were seen. No detectable association of liposomes with the cellular membrane was observed for both RGD- and NT-liposome incubated HUVECs.

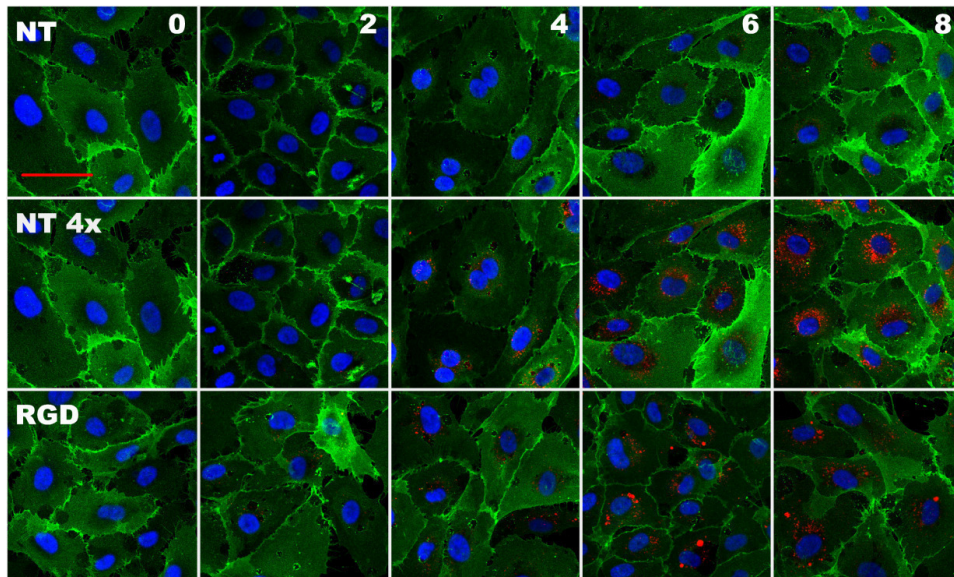


**Figure 4 CLSM images of HUVECs incubated with RGD-liposomes (RGD) or NT-liposomes (NT). Blue = DAPI, red = rhodamine, green = CD31, red bar = 50  $\mu\text{m}$ . The number shown in the top right corner of each column refers to the incubation time in hours. Note that the laser intensity used to obtain NT 4x images (middle row) was fourfold higher than the intensity used to obtain the other images (bottom and top row).**

To assess the consequences of cellular association for the relaxometric properties of the paramagnetic contrast agent the longitudinal ( $R_1$ ) (Figure 5A) and the transverse ( $R_2$ ) relaxation rates (Figure 5B) were measured in loosely-packed cell pellets. For the incubation with RGD-liposomes  $R_1$  increased from a pre-incubation value of  $0.47 \text{ s}^{-1}$  to  $0.67 \text{ s}^{-1}$ . For incubations with NT-liposomes, an increase of  $R_1$  from  $0.47 \text{ s}^{-1}$  to  $0.59 \text{ s}^{-1}$  was observed. Longitudinal relaxation rates for HUVECs incubated with RGD-liposomes were only slightly higher than  $R_1$  relaxation rates for HUVECs incubated with NT-liposomes. Assuming a linear relationship between relaxation rate and concentration, the longitudinal relaxivity ( $r_1$ ) was estimated to be  $1.5 \pm 0.4$  and  $2.2 \pm 0.2 \text{ mM}^{-1}\text{s}^{-1}$  for HUVECs incubated with RGD- and NT-liposomes, respectively. No significant differences were observed between the  $R_2$ -values for HUVECs incubated with RGD- or NT-liposomes (Figure 5B). Incubation led to an increase in transverse relaxation rate from the pre-incubation value of  $28.2 \text{ s}^{-1}$  to  $30.0 \text{ s}^{-1}$  and  $31.8 \text{ s}^{-1}$  for RGD- and NT-liposomes, respectively. Assuming a linear fit, the transverse relaxivity ( $r_2$ ) was determined for HUVECs incubated with RGD-liposomes, yielding a value of  $36.0 \pm 6.3 \text{ mM}^{-1}\text{s}^{-1}$ . Scatter in the data prevented accurate determination of the proton transverse relaxivity of HUVECs incubated with NT-liposomes.

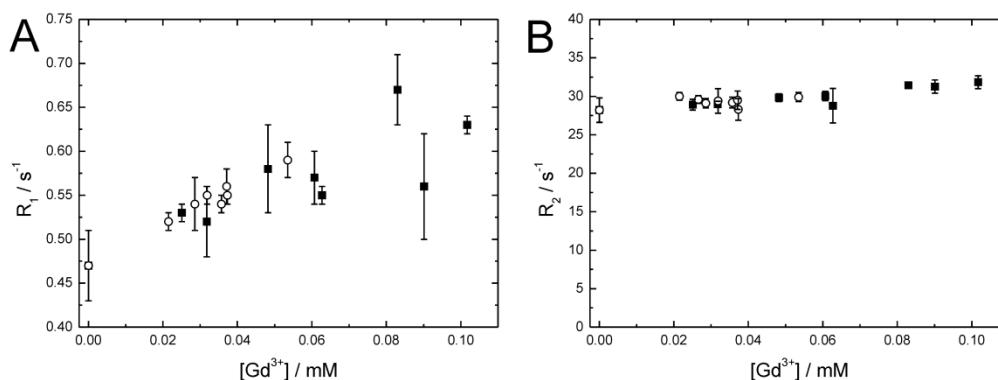


**Figure 5,  $^1\text{H}$  relaxometry measurements for pellets of HUVECs incubated with RGD-liposomes (solid squares) or NT-liposomes (open circles).  $R_1$  (A) and  $R_2$  (B) as a function of the concentration of gadolinium. Data represent mean  $\pm$  SD ( $n=3$ )**

To validate whether radiolabeling of the multimodal contrast agent enabled its quantification, the uptake of contrast agent was calculated based on  $\gamma$ -counting data. The gadolinium concentration was calculated by measuring the activity of a standard containing a known amount of  $^{111}\text{Indium}$  labeled Gd-based liposomes. Figure 6 shows the calculated gadolinium content as a function of the gadolinium content as determined by ICP-MS. An excellent agreement was found: a linear fit yielded a slope of  $1.01 \pm 0.01$  and an intercept of

$4.4 \pm 0.7$  nmol ( $R^2 = 0.99$ ), indicating a slight overestimation of the gadolinium content based on  $\gamma$ -counting.

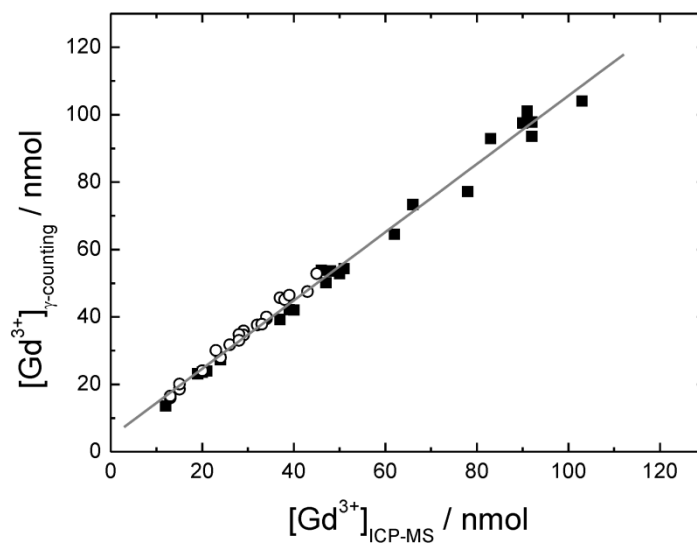


**Figure 6, Gadolinium content as calculated from  $\gamma$ -counting as a function of the gadolinium concentration determined by ICP-MS for HUVECs incubated with RGD-liposomes (solid squares) or NT-liposomes (open circles). Solid line is a linear fit to all experimental data resulting in  $Gd^{3+}_{\gamma-counting} = 1.01 \cdot Gd^{3+}_{ICP-MS} + 4.4$ ,  $R^2 = 0.99$ .**

### Discussion and Conclusions

In this paper we have presented a novel liposome formulation for multimodal SPECT/MRI detection. Liposomes were prepared that contained both Gd-DOTA for MRI detection and empty DOTA chelates that were used for labeling with  $^{111}\text{In}$  for SPECT detection. CryoTEM revealed round unilamellar liposomal structures and a minor fraction of disk-shaped micelles. Previously Hak *et al.* [17] have observed the presence of these disk-shaped micelles as well, for liposomes with a similar composition. After labeling with  $^{111}\text{In}$ , radiochemical purities were  $> 95\%$  for the RGD-liposomes as well as the NT-liposomes.

To study the quantification potential of the multimodal contrast agent, a model system was used, consisting of an *in vitro* culture of human umbilical vein derived endothelial cells. Cellular internalization was achieved by targeting the  $\alpha_v\beta_3$ -integrin with cyclic RGD-peptide. Non-targeted liposomes served as a control for non-specific uptake. As expected, quantification using proton MRI was hampered by a difference in longitudinal relaxivity between cell internalized RGD- and NT liposomes, which was probably caused by intracellular confinement. RGD-liposomes ended up in larger intravesicular structures than NT-liposomes. A larger size results in a lower surface to volume ratio and is therefore associated with a less effective flux of water proton across the vesicular membrane. This effect leads to a lowering of the relaxivity, coined quenching, and has been observed previously for liposomal systems (Chapter 2 and 3).

SPECT-imaging and subsequent quantification was not feasible due to low uptake and very small cell pellets. The cause of the low uptake of RGD-liposomes, that was approximately a factor 20 lower than reported previously for RGD-liposomes using the same model system is unknown (Chapter 2).  $\gamma$ -counting was used to quantify the uptake of indium and was compared to the gadolinium content as determined by ICP-MS. An excellent linear correlation was observed, permitting very accurate quantification. Corresponding SPECT-images of cell pellets nicely concurred with the data obtained by both ICP-MS and  $\gamma$ -counting. For  $\gamma$ -counting, however, a small offset was found, which revealed a small overestimation of the gadolinium content based on the  $\gamma$ -counting. A factor that may have led to an overestimation is the uptake of In-DTPA. After incubation of the liposomes with  $^{111}\text{In}$ , DTPA was added to scavenge free  $^{111}\text{In}$ . Although more than 95% of the  $^{111}\text{In}$  was bound by DOTA-DSPE, the remaining 1-5% of the indium might have been present in the suspension as In-DTPA. Uptake of In-DTPA would lead to an overestimation of the gadolinium content. Another aspect that should be considered, is the

stability of the contrast agent. The  $^{111}\text{In}$ -DOTA chelate used on the surface of the liposomal contrast agent used was stable in plasma and PBS at 37 °C up to at least 24 hr of incubation. Therefore it can be ruled out that the increase in gadolinium is the result of the uptake of indium released from the chelate, by for instance transmetallation [18], especially since the thermodynamic stability constants of In-DOTA and Gd-DOTA are very high ( $\text{pK}_D = 24.0$  and  $23.9$ , respectively [19]).

In conclusion, we have presented a new multimodal SPECT/MRI contrast agent that unites the best features of SPECT and MRI. It was found that the radiolabel allowed accurate quantification of cell-internalized probe using  $\gamma$ -counting. In the future, this multimodal contrast agent may serve as an excellent tool for image-monitored drug delivery, cell tracking and molecular imaging using hybrid SPECT/MRI technology.



## Literature

1. Massoud, T.F., S.S. Gambhir, *Genes Dev*, 2003. **17**(5): p. 545-580.
2. Jennings, L.E., N.J. Long, *Chem Commun (Camb)*, 2009(24): p. 3511-3524.
3. Beyer, T., D.W. Townsend, T. Brun, *et al.*, *J Nucl Med*, 2000. **41**(8): p. 1369-1379.
4. Yamamoto, S., M. Imaizumi, Y. Kanai, *et al.*, *Ann Nucl Med*, 2010 In Press.
5. Catana, C., Y. Wu, M.S. Judenhofer, *et al.*, *J Nucl Med*, 2006. **47**(12): p. 1968-1976.
6. Schipper, M.L., Z. Cheng, S.W. Lee, *et al.*, *J Nucl Med*, 2007. **48**(9): p. 1511-1518.
7. Yang, Z., S. Zheng, W.J. Harrison, *et al.*, *Biomacromolecules*, 2007. **8**(11): p. 3422-3428.
8. Lijowski, M., S. Caruthers, G. Hu, *et al.*, *Invest Radiol*, 2009. **44**(1): p. 15-22.
9. Mishra, A., J. Pfeuffer, R. Mishra, *et al.*, *Bioconjug Chem*, 2006. **17**(3): p. 773-780.
10. Dirksen, A., S. Langereis, B.F. de Waal, *et al.*, *Org Lett*, 2004. **6**(26): p. 4857-4860.
11. Mulder, W.J., G.J. Strijkers, J.W. Habets, *et al.*, *Faseb J*, 2005. **19**(14): p. 2008-2010.
12. Mulder, W.J., R. Koole, R.J. Brandwijk, *et al.*, *Nano Lett*, 2006. **6**(1): p. 1-6.
13. Na, H.B., I.S. Lee, H. Seo, *et al.*, *Chem Commun (Camb)*, 2007(48): p. 5167-5169.
14. Tsotsalas, M., M. Busby, E. Gianolio, *et al.*, *Chemistry of Materials*, 2008. **20**(18): p. 5888.
15. Mulder, W.J., G.J. Strijkers, A.W. Griffioen, *et al.*, *Bioconjug Chem*, 2004. **15**(4): p. 799-806.
16. Rouser, G., S. Fkeischer, A. Yamamoto, *Lipids*, 1970. **5**(5): p. 494-496.
17. Hak, S., H.M. Sanders, P. Agrawal, *et al.*, *Eur J Pharm Biopharm*, 2009. **72**(2): p. 397-404.
18. Laurent, S., L.V. Elst, F. Copoix, *et al.*, *Invest Radiol*, 2001. **36**(2): p. 115-122.
19. Clarke, E.T., A.E. Martell, *Inorganica Chimica Acta*, 1991. **190**(1): p. 37.

## Chapter **8**

### **General discussion**

**General discussion**

The aim of this thesis was to study the effects of internalization of lipid based MR contrast agents by cells, focusing on cellular location, relaxometry and quantification. Several MRI contrast agents, including liposomes, quantum dots and emulsions, were incubated with HUVECs to study these effects. The cyclic RGD peptide-integrin ligand-receptor couple was used as a model approach. Not only the size of the contrast agents was varied, but also the gadolinium chelates incorporated in the lipid (bi)layer. From chapter 2-5, it is evident that contrast agent quantification using  $^1\text{H}$  MRI is very challenging, especially since the relaxivity of a paramagnetic contrast agent is greatly influenced by cellular internalization. To address this problem two multimodality contrast agents were developed that combine the high spatial resolution of  $^1\text{H}$  MRI with the quantification abilities of either  $^{19}\text{F}$  MRI/MRS or SPECT. In this final chapter an overview is given of the results of incubations with the different contrast agents and the findings regarding cellular location, relaxometric properties and cellular uptake will be discussed. Furthermore, the application of gadolinium based contrast agents will be reviewed, followed by a discussion on the use of multimodality imaging.

**Contrast agents**

Table 1 shows an overview of basic characteristics of the contrast agents used in this thesis. When comparing paramagnetic liposomes to paramagnetic quantum dots, it can be observed that the quantum dots have both a higher longitudinal and transverse relaxivity. Gd-DOTA-DSPE, which was chosen for the higher stability of its Gd-chelate complex, had somewhat higher  $r_1$ -values whereas  $r_2$ -values remained similar. In chapter 6 emulsions were used as a contrast agent for both  $^1\text{H}/^{19}\text{F}$  MRI and  $^{19}\text{F}$  MRS. When compared to a liposome with approximately the same diameter, it was found that both longitudinal and transverse relaxivity were increased by a factor 2.5. This increase in relaxivity can be mainly attributed to differences in structural properties. Liposomes consist of a double layer of lipids, whereas emulsions are coated with a monolayer of lipids. For liposomes the relaxivity of the contrast agent is lower, since contributions of the gadolinium containing lipids on the inside of the liposome are greatly diminished by the low flux of water protons across the liposomal membrane [1, 2].

**Cellular uptake of contrast agent**

In Table 2 the uptake of the contrast agent used in this thesis by HUVECs is summarized. In general, relatively low levels of the non-targeted contrast agents were taken up by the cells. For RGD-conjugated contrast agent uptake varied considerably for the different systems. RGD-quantum dots, the smallest

nanoparticles used in this thesis, were taken up by HUVECs to a lesser extent than other targeted contrast agents. After 24 hr of incubation a 30 fold lower uptake was found when compared to the uptake of RGD-liposomes. Several factors may have caused this difference in uptake. First of all, a three times lower total lipid concentration was used for the incubation of the HUVECs (see Table 1). Secondly, each quantum dot contains approximately 5000 gadolinium-based lipids, whereas a liposome contributes 20 times as many Gd-lipids. As a result, the number of nanoparticles that has to be internalized needs to be higher to achieve the same concentration of gadolinium as for incubations with RGD-liposomes. Also a lower uptake was found for incubations with emulsion. A lower uptake of gadolinium was expected especially since the Gd-containing lipid fraction was 2.5-fold lower than for liposomes or quantum dots, which was necessary to obtain stable emulsions. Furthermore, it should be noted that the hydrophobic core of the emulsion was coated with a monolayer of lipids rather than the double layer that encloses liposomes.

**Table 1, Contrast agent characterization of  $\alpha_v\beta_3$ -targeted (RGD) and non-targeted (NT) contrast agents.**

	Liposomes (Chapter 2)		Quantum Dots (Chapter 5)		Emulsion (Chapter 6)		Liposomes (Chapter 7)	
	RGD	NT	RGD	NT	RGD	NT	RGD	NT
Chelate <sup>o</sup>	Gd-DTPA-BSA		Gd-DTPA-BSA		Gd-DOTA-DSPE		Gd-DOTA-DSPE	
$r_{1,H}$ (mM <sup>-1</sup> s <sup>-1</sup> ) <sup>*</sup>	2.1	2.3	5.2	5.7	7.4	8.0	2.7	3.4
$r_{2,H}$ (mM <sup>-1</sup> s <sup>-1</sup> ) <sup>*</sup>	17.3	19.6	26.1	32.4	36.8	41.3	16.2	16.1
Diameter (nm) <sup>#</sup>	185	185	43	49	182	178	175	176
[lipid] (mM) <sup>+</sup>	1.0		0.35		1.0		1.2	
[Gd <sup>3+</sup> ] (mM) <sup>+</sup>	0.25		0.17		0.10		0.30	

<sup>o</sup> Gd-chelate incorporated in the nanoparticle (see appropriate chapter for details)

<sup>\*</sup> measured at 6.3T at 20°C

<sup>#</sup> measured at 25°C using dynamic light scattering (DLS)

<sup>+</sup> concentration of total lipid and Gd-lipid used for incubation experiments

**Table 2, Cellular uptake of contrast agents, <sup>1</sup>H relaxometry and size of fluorescent intracellular vesicular structures of HUVECs incubated with either  $\alpha_v\beta_3$ -targeted (RGD) or non-targeted (NT) contrast agents. Data refer to 8 or 24 hr incubations of cells with different nanoparticle preparations**

	Liposomes (Chapter 2)		Quantum Dots (Chapter 5)		Emulsion (Chapter 6)		Liposomes (Chapter 7)	
	RGD	NT	RGD	NT	RGD	NT	RGD	NT
[Gd <sup>3+</sup> ] (mM) 8 hr <sup>o</sup>	2.1	0.14	0.10	0.10	0.40	0.06	0.10	0.05
[Gd <sup>3+</sup> ] (mM) 24 hr <sup>o</sup>	3.3	0.22	0.15	0.13	-	-	-	-
$r_{1,H}$ (mM <sup>-1</sup> s <sup>-1</sup> ) <sup>*</sup>	0.1-1.8 <sup>‡</sup>	4.7	4.2	4.0	1.1	2.6	1.5	2.2
$r_{2,H}$ (mM <sup>-1</sup> s <sup>-1</sup> ) <sup>*</sup>	26.9	15.6	-	-	31	-	36.0	-
size vesicle (μm) <sup>#</sup>	1.5	0.4-1	1-2	1-2	4-7	1-4	0.4-2	0.4-1

<sup>o</sup> pellet concentrations of Gd<sup>3+</sup> as determined by ICP-AES / ICP-MS

<sup>\*</sup> measured at 6.3 T at 20°C

<sup>#</sup> obtained from confocal laser scanning microscopy (CLSM) images

<sup>‡</sup> longitudinal relaxivity gradually decreased over time

Calculation of  $\alpha_v\beta_3$ -integrin expression

An attempt was made to determine the  $\alpha_v\beta_3$ -integrin levels on HUVECs based on ICP-AES and ICP-MS data. The number of nanoparticles (NP) internalized per cell can be estimated based on the gadolinium concentration obtained for HUVECs incubated with a RGD-contrast agent. The number of lipids in each particle was calculated using the diameter of the contrast agent as determined by DLS (liposomes and emulsion) or in case of the quantum dots, the diameter of the inorganic core including the hydrophobic capping. The number of lipids assembled per contrast agent particle was calculated by assuming a surface area of  $42.5 \text{ \AA}^2$  per lipid. Furthermore, we assumed that  $10 \text{ }\mu\text{L}$  of cell pellet contained approximately  $2 \cdot 10^6$  cells. Results of these estimations are summarized in Table 3.

**Table 3, Results of calculations of the gadolinium content, the number of internalized RGD-conjugated nanoparticles (NP) and the number of  $\alpha_v\beta_3$ -integrins per cell, based on ICP-AES and ICP-MS data.**

	Liposomes (Chapter 2)	Quantum Dots (Chapter 5)	Emulsion (Chapter 6)	Liposomes (Chapter 7)
[NP] (nM)	2.5	100	5	3
Gd <sup>3+</sup> /NP	105000	5000	21000	105000
Gd <sup>3+</sup> /cell (fmol/cell) 8 hr	11	0.5	1.9	0.5
Gd <sup>3+</sup> /cell (fmol/cell) 24 hr	17	0.8	-	-
NP/cell 8 hr	63000	60000	55000	3000
NP/cell 24 hr	100000	90000	-	-
$\alpha_v\beta_3$ /cell	2000	2400	3200	140
[ $\alpha_v\beta_3$ ] (nM)	0.7	0.8	1.1	0.05

The estimated number of internalized NP/cell is very similar for quantum dots, liposomes containing Gd-DTPA-BSA and the emulsion. However, the estimated number of liposomes containing Gd-DOTA-DSPE taken up by HUVECs (Chapter 7) was rather low. Based on the nanoparticle uptake, an attempt was made to estimate the number of  $\alpha_v\beta_3$ -integrins per cell. Calculations were based on a median half life of 10 min for the  $\alpha_v\beta_3$ -integrin to be recycled back to the membrane as was reported by Caswell *et al.* [3] and uptake of one nanoparticle per available  $\alpha_v\beta_3$ -integrin. To rule out effects of excretion of the contrast agent, calculations were based on incubations shorter than 4 hr during which uptake of contrast agent was approximately linear. Table 3 shows similar estimations for the number of  $\alpha_v\beta_3$ -integrins present on a single cell (2000-3200  $\alpha_v\beta_3$ /cell) for incubations with liposomes containing Gd-DTPA-BSA, the quantum dots and the emulsion, whereas experiments with liposomes containing Gd-DOTA-DSPE revealed a much lower value. The number of receptors per cell as found for studies with liposomes containing Gd-DTPA-BSA, the quantum dots and the emulsion is of similar order as values found in literature for the  $\alpha_v$ -subunit ( $2.8 \cdot 10^4$ ) and  $\beta_3$ -subunit ( $6.2 \cdot 10^3$ ) [4]. The latter values were obtained using antibody coated iron oxide particles and flow cytometry. Table 3 further shows

the estimations of the effective  $\alpha_v\beta_3$ -concentration (0.7-1.1 nM) for incubations with liposomes containing Gd-DTPA-BSA, the quantum dots and the emulsion. Incubation with liposomes containing Gd-DOTA-DSPE revealed a much lower value. Obviously, the above calculations assumed the integrin expression level to remain constant throughout the experiment. This may not hold true, as integrin expression can be modulated by prolonged exposure to high levels of the RGD-ligand.

#### Quenching of the longitudinal relaxivity

Table 2 shows the  $^1\text{H}$ -MR relaxometry data of both HUVEC-internalized  $\alpha_v\beta_3$ -targeted (RGD) and non-targeted (NT) paramagnetic contrast agents. The longitudinal relaxivity ( $r_1$ ) of the different contrast agents highly varied after internalization by HUVECs. Incubation for 24 hr with RGD-liposomes using DTPA-chelates led to highest quenching of the longitudinal relaxivity resulting in an effective  $r_1$  as low as  $0.1 \text{ mM}^{-1}\text{s}^{-1}$ . Shorter incubation with these RGD-liposomes revealed higher longitudinal relaxivities up to  $1.8 \text{ mM}^{-1}\text{s}^{-1}$  for the shortest incubation time, which is only slightly lower than the relaxivity of liposomes in suspension (see Table 1). Incubation with RGD-conjugated paramagnetic quantum dots led to a high effective  $r_1$  of  $4.2 \text{ mM}^{-1}\text{s}^{-1}$ , only slightly lower than the relaxivity for quantum dots in suspension. Incubation with the RGD-emulsion and liposomes containing Gd-DOTA-DSPE also revealed quenching of the longitudinal relaxivity, but to a lesser extent than was the case for RGD-liposomes.

NT-nanoparticles showed a different trend. For liposomes, a two-fold higher  $r_1$  was found compared to liposomes in suspension. An explanation for the increase in relaxivity might be that the structural integrity of the liposomes is compromised within the intracellular compartments. In intact liposomes, the  $T_1$ -shortening efficacy of the gadolinium containing lipids in the inner monolayer of the liposome is greatly diminished since the rate of water proton exchange across the liposomal membrane with the present composition is very low [1, 2]. If the integrity of the liposomes is compromised, the gadolinium containing lipids, localized in the inner leaflet of the liposomal membrane, may be engaged in  $T_1$ -shortening of the extraliposomal water leading to an increased relaxivity. Lipid-coated emulsions and quantum dots contain a monolayer of lipids and no increase in relaxivity was observed. Interestingly, the  $r_1$  of the internalized emulsion was even three-fold lower than the contrast agent in suspension.

In general, higher intracellular concentrations of contrast agent led to more pronounced quenching of the longitudinal relaxivity. Higher uptake was associated with larger intracellular rhodamine PE positive structures. Both RGD-

and NT-emulsion caused large rhodamine PE positive vesicular structures up to 4-7  $\mu\text{m}$ , whereas incubations with paramagnetic quantum dots yielded a mean vesicular size of 1  $\mu\text{m}$ . Larger vesicular structures have a lower surface-to-volume ratio and therefore the limited flux of water protons across the vesicular membrane (chapter 3) will cause a reduction of the effective longitudinal relaxivity. The opposite holds for the smaller vesicular structures as observed in case of the uptake of NT-liposomes and paramagnetic quantum dots that show a relatively high longitudinal relaxivity.

The experiments described in this thesis showed that the effective relaxation enhancement as brought about by an internalized paramagnetic contrast agent critically depends on its intracellular localization and/or concentration. In general, the longitudinal relaxivity of internalized  $\alpha_v\beta_3$ -targeted contrast agent was much lower than that of NT-contrast agents. For liposomes, quenching of the longitudinal relaxivity was already observed for relatively low intracellular gadolinium concentrations ( $\sim 0.1$  mM). Surprisingly, no differences in longitudinal relaxivity between RGD- and NT-paramagnetic quantum dots were observed. Although it remains to be demonstrated, this quenching effect may also occur *in vivo*, which would hamper the detection and quantification of targeted contrast agent with  $T_1$ -weighted MRI. It might be beneficial to design targeted contrast agents that are either not taken up in or that are released from endosomes. Several techniques have been suggested to release macromolecules from endosomes or to avoid endosomation. Photochemical internalization was used by the group of Aime *et al.* to release endocytosed contrast agent [5]. The release from endocytic vesicles into the cytoplasm was triggered by a photosensitizer that was incorporated in the endosomal membranes and can be activated by light. As expected, endosomal release led to an elevation of the  $r_1$  relaxivity [6, 7]. Furthermore, cell penetrating peptides have been used to bypass endosomation and enable vehicle delivery directly into the cytoplasm [8-11].

#### Contrast agent stability

An important observation in chapter 5 and 6 was a discrepancy in the gadolinium to core material ratio for quantum dots and emulsions coated with paramagnetic lipids. The discrepancy is possibly caused by a transfer of lipids between the contrast agent and the cellular membrane. Although this hypothesis needs to be further substantiated, by for instance labeling of the different components of the contrast agent with fluorophores or radiolabels, nanoparticles need to be developed that are more stable. There are several methods to stabilize the lipid coating, including the use of block-copolymers that can be tuned to form micelles or polymersomes with a very low critical micelle

concentration [12, 13]. The same polymers may also be used to coat the surface of quantum dots [14]. A different approach is to introduce crosslinks in the monolayer covering the surface to stabilize the nanoparticles [15, 16]. Furthermore, the quantum dots used in this thesis were capped with octadecylamine. Instead of capping the quantum dots with a hydrophobic compound, a compound can be introduced that is either water soluble or can be chemically converted to be water soluble [17, 18]. Since quantum dots are susceptible to oxidation, the latter option seems most suitable. Another possibility would be to employ lipids containing one or more unsaturated carbon-carbon bonds in their acyl chain for the lipid coating of the paramagnetic quantum dots. Utilization of unsaturated lipids leads to a lower gel-to-liquid crystalline phase-transition temperature, which is hypothesized to stabilize the lipid coating of the paramagnetic quantum dots, thereby reducing the rate of lipid-transfer.

Another important observation for contrast agent stability was made in chapter 4. A gradual decrease in longitudinal relaxivity was observed upon incubation over a period of 5 days with fresh medium after initial loading with contrast agent. It was hypothesized that this decrease in relaxivity is caused by transmetallation of the gadolinium chelate. Transmetallation is a process in which a metal ion expels the gadolinium ion from its chelate. After its release, the expelled  $Gd^{3+}$  ions can form insoluble complexes with for instance hydroxide or phosphate ions that are present in the medium and become MR silent. Since the formation of a Gd-salt prevents direct interaction of water protons with the ion, we had anticipated the contrast agent to become  $T_1$ -silent after transmetallation. Interestingly, also  $T_2$ -shortening was observed over time.  $T_2$ -silencing may have been caused by the formation of large Gd-containing structures for which the static dephasing regime holds.

Recent findings have shown that transmetallation of gadolinium based contrast agent is a likely cause of a disease called nephrogenic systemic fibrosis (NSF) [19]. NSF occurred after administration of low molecular weight gadolinium-based contrast agents with a low thermodynamic and kinetic stability constant, such as Omniscan, to patients with renal failure or insufficiency [20]. It is hypothesized that a longer retention time as a consequence of a lower clearance rate rendered the contrast agent more prone to transmetallation. Cellular internalization of (targeted) contrast agents also leads to longer retention times, rendering the contrast agent more prone to transmetallation. For *in vitro* and *in vivo* application it is of great importance to use Gd-chelates that have a very high stability constant, such as Gd-DOTA and Gd-DO3A which are as a result less prone to transmetallation [19, 21, 22]. In chapter 6 and 7 we have used



Gd-DOTA-DSPE lipids, to prevent release of  $Gd^{3+}$  from the chelate. Besides the use of Gd-chelates with a very low dissociation constant, also the molecular target is of great importance. Targeting of moieties that do not lead to internalization, such as extracellular matrix proteins, may lead to a shortening of the contrast agent's retention time and therefore adverse effects are less likely to occur.

### Quantification

Quantification of the contrast agent concentration is very beneficial for cell tracking and MRI monitored drug delivery, since contrast agent concentration can be directly related to the amount of cells or the concentration of drugs present at a specific location. For molecular imaging the demands are even higher as one would ideally want to convert the concentration of contrast agent to the levels of a molecular marker. The concentration of markers that are not internalized by cells upon ligand binding, such as extracellular matrix component proteins and non-internalizing receptors, can be determined in a relatively straightforward manner, provided that the probe-target interaction is well understood. However, for molecular markers, which are internalized by cells, this task is extremely challenging. Especially since the relaxivity of the contrast agent is affected by internalization and/or processing by the cell. In many cases, however, quantification of the marker concentration will not be strictly needed and qualitative assessments of changes in molecular marker concentration will provide sufficient information for enabling meaningful diagnosis and staging of a disease or monitoring treatment response.

Chapter 2-7 have shown that quantification of the contrast agent based on the  $^1H$  MRI signal intensity is hampered by differences in longitudinal relaxivity between targeted and non-targeted contrast agent after internalization by cells. Especially, since no straightforward approach is available to distinguish aspecific uptake from the specific uptake of targeted nanoparticles, beforehand. Therefore, other techniques were exploited and combined with  $^1H$  MRI to explore the ability to quantify the concentration of contrast agent. Chapter 6 and 7 combine  $^{19}F$  MRI/MRI or SPECT with  $^1H$  MRI and showed excellent quantification potential for these combinations. Both approaches can be applied *in vivo*, however, also have their strengths and weaknesses. The main drawback of  $^{19}F$ -MR is its high detection limit. In this thesis a dedicated solenoid coil was used with a diameter of 6 mm resulting in a detection limit of 2 mM and 27 mM for  $^{19}F$  MRS and MRI, respectively. A larger coil will be needed for *in vivo* experiments, resulting in an even higher detection threshold. The combination of SPECT and MRI is very powerful, since it unites the very high sensitivity of SPECT with the high resolution anatomical information of MRI. Uptake of

contrast agent can therefore be detected and quantified with SPECT, while  $^1\text{H}$  MRI provides detailed information on its location. The main drawback of the combination of these two techniques is that the two images acquired separately need to be merged. Recent developments of hybrid scanners such as the PET/MRI or SPECT/MRI combinations [23-26] will allow simultaneous acquisition and therefore straightforward integration of the images.

### **Conclusion**

In this thesis the effects of internalization of lipid based MR contrast agents by cells have been studied, emphasizing on cellular location, relaxometry and quantification. In general, the relaxivity of paramagnetic contrast agent was found to be strongly affected by the internalization by cells. This phenomenon hampers the quantification of paramagnetic contrast agent uptake with the use of  $^1\text{H}$  MRI. Furthermore we have observed a large decrease in relaxivity for long retention times of the contrast agent within cells (chapter 4). Transmetallation may have caused this lowering of the relaxivity. In chapter 6 and 7, gadolinium chelates were used that have a higher thermodynamic as well as kinetic stability to prevent this process from occurring. The issue of quantification of molecular markers, which is of great benefit to molecular MRI, cell tracking and MRI monitored drug delivery, may be tackled by combining multiple techniques, such as MRI/MRS, MRI/SPECT or MRI/PET. Although the combination of the nuclear techniques with MRI is technologically very challenging and appropriate multimodal contrast agents need to be developed, the development of hybrid scanners for simultaneous dual-modality acquisition holds great promise for the future of biomedical imaging.

## Literature

1. Terreno, E., Sanino, A., Carrera, C., et al., *Journal of Inorganic Biochemistry*, 2008. **102**(5-6): p. 1112.
2. Strijkers, G.J., Mulder, W.J.M., van Heeswijk, R.B., et al., *Magnetic Resonance Materials in Physics, Biology and Medicine*, 2005. **18**(4): p. 186-192.
3. Caswell, P.T., Norman, J.C., *Traffic*, 2006. **7**(1): p. 14-21.
4. Benedetto, S., Pulito, R., Crich, S.G., et al., *Magn Reson Med*, 2006. **56**(4): p. 711-6.
5. Hogset, A., Prasmickaite, L., Selbo, P.K., et al., *Adv Drug Deliv Rev*, 2004. **56**(1): p. 95-115.
6. Gianolio, E., Arena, F., Hogset, A., Aime, S., *Proc. Intl. Soc. Mag. Reson. Med.*, 2009. **17**: p. 3162.
7. Aime, S., Castelli, D.D., Crich, S.G., et al., *Acc Chem Res*, 2009. **42**(7): p. 822-31.
8. Torchilin, V.P., Rammohan, R., Weissig, V., et al., *Proc Natl Acad Sci U S A*, 2001. **98**(15): p. 8786-91.
9. Lewin, M., Carlesso, N., Tung, C.H., et al., *Nat Biotechnol*, 2000. **18**(4): p. 410-4.
10. Josephson, L., Tung, C.H., Moore, A., et al., *Bioconjug Chem*, 1999. **10**(2): p. 186-91.
11. Medarova, Z., Pham, W., Farrar, C., et al., *Nat Med*, 2007. **13**(3): p. 372-7.
12. Jones, M., Leroux, J., *Eur J Pharm Biopharm*, 1999. **48**(2): p. 101-11.
13. Kwon, G.S., Okano, T., *Pharm Res*, 1999. **16**(5): p. 597-600.
14. Nasongkla, N., Bey, E., Ren, J., et al., *Nano Lett*, 2006. **6**(11): p. 2427-30.
15. Shuai, X., Merdan, T., Schaper, A.K., et al., *Bioconjug Chem*, 2004. **15**(3): p. 441-8.
16. Weaver, J.V., Tang, Y., Liu, S., et al., *Angew Chem Int Ed Engl*, 2004. **43**(11): p. 1389-92.
17. Di Marco, M., Sadun, C., Port, M., et al., *Int J Nanomedicine*, 2007. **2**(4): p. 609-22.
18. Portet, D., Denizot, B., Rump, E., et al., *J Colloid Interface Sci*, 2001. **238**(1): p. 37-42.
19. Idee, J.M., Port, M., Robic, C., et al., *J Magn Reson Imaging*, 2009. **30**(6): p. 1249-58.
20. Hermann, P., Kotek, J., Kubicek, V., et al., *Dalton Trans*, 2008(23): p. 3027-47.
21. Hak, S., Sanders, H.M., Agrawal, P., et al., *Eur J Pharm Biopharm*, 2009. **72**(2): p. 397-404.
22. Laurent, S., Elst, L.V., Copoix, F., et al., *Invest Radiol*, 2001. **36**(2): p. 115-22.
23. Judenhofer, M.S., Wehrl, H.F., Newport, D.F., et al., *Nat Med*, 2008. **14**(4): p. 459-65.
24. Pichler, B.J., Judenhofer, M.S., Pfannenberger, C., *Handb Exp Pharmacol*, 2008(185 Pt 1): p. 109-32.
25. Patton, J.A., Townsend, D.W., Hutton, B.F., *Semin Nucl Med*, 2009. **39**(4): p. 247-63.
26. Cherry, S.R., *Semin Nucl Med*, 2009. **39**(5): p. 348-53.

**Summary**

**Dankwoord**

**List of Publications**

**Curriculum Vitae**



## Summary

Powerful contrast agents are essential for molecular imaging, a new and rapidly developing field that focuses on *in vivo* imaging of biological markers and processes. **Chapter 1** provided an introduction on molecular imaging and gave an overview of research conducted in four major application areas: cancer, atherosclerosis, myocardial infarction and neurological disorders. Furthermore the parameters that play a critical role in molecular imaging were addressed, focusing on the challenges and opportunities of molecular imaging based on MRI.

The **aim of this thesis** was to study the interaction of targeted MRI contrast agents with cultured mammalian cells, focusing on cellular location, relaxometry and quantification. Several lipid-based MRI contrast agents, including liposomes, quantum dots and emulsions, were incubated with human umbilical vein derived endothelial cells (HUVECs) as an *in vitro* model for assessing vital aspects of molecular MRI.

In **chapter 2** the *in vitro* model setup was presented that was used throughout this thesis work to investigate the consequences of uptake of high payload multimodal paramagnetic contrast agents on their  $T_1$ - and  $T_2$ -shortening efficacy. Cultured HUVECs were incubated with paramagnetic liposomes that were conjugated with a cyclic RGD-peptide to enable internalization via the  $\alpha_v\beta_3$ -integrin receptor. Non-targeted liposomes served as a control. Integrin targeting indeed strongly increased the uptake of paramagnetic liposomes, which were deposited in perinuclear vesicles. This amplification strategy, however, strongly reduced the longitudinal relaxivity of the internalized paramagnetic liposomes.

In **chapter 3** a mathematical model was presented that describes the effective longitudinal relaxation rate  $R_1$  for water protons in three cellular compartments (extracellular, cytoplasmic and vesicular subcellular spaces) as a function of compartment size, intercompartmental water exchange rates and local contrast agent concentration. The model was used to explain the effective  $R_1$  dependence on the overall concentration of cell-internalized  $Gd^{3+}$ -containing liposomes that was measured in chapter 2. Relaxation parameters were simulated using a modified Bloch-McConnell equation including magnetization exchange between the three compartments. With the model several possible scenarios for internalized contrast agent distribution were evaluated. Relaxation parameters were calculated for contrast agent restricted to the cytoplasmic or vesicular compartments. The voxel contrast agent concentration dependencies of  $R_1$  can be used to qualitatively and quantitatively understand a number of different

experimental observations reported in the literature. Most importantly the simulations reproduced the longitudinal relaxivity “quenching” for cell-internalized liposomes described in chapter 2.

**Chapter 4** reported on the investigations into the longer-term fate of the cell-internalized liposomes by studying their relaxometric properties over 5 days, following an initial 24 hr loading period. Circa 25% of the  $\text{Gd}^{3+}$  content delivered to the cells via integrin-targeted liposomes was lost in the first 24 hr, which led to 65% and 77% reductions in  $R_1$  and  $R_2$ , respectively, as compared to the original  $R_1$  and  $R_2$  enhancements. This implies that the remaining cell-associated gadolinium had relatively low effective  $r_1$  and  $r_2$  relaxivities. It was proposed that this is due to gradual release of  $\text{Gd}^{3+}$  from the chelate in the cell, followed by sequestration in an MR silent state. Most of the gadolinium internalized by cells following incubation with non-targeted liposomes was released in the 5-day follow-up period.

**Chapter 5** described the relaxometric, optical and compositional properties of  $\alpha_v\beta_3$ -integrin targeted- and non-targeted paramagnetic quantum dot micelles (pQDs) after incubation with HUVECs. pQDs are promising nanoparticles for bimodal molecular imaging purposes: their excellent optical properties allow for *in vivo* optical imaging in small animals, while the high Gd payload allows for detection using contrast-enhanced MRI. Cell-associated pQDs showed no concentration or time-dependent change in fluorescent intensities and cellular relaxivities, enabling accurate assessment of their uptake by HUVECs using relaxometric and optical measurements. However, the molar ratio of Gd (originating from the lipid coating) to Cd (from the QD core material) in pellets containing pQD-incubated cells was significantly higher than the Gd/Cd molar ratio of the pQDs as prepared. It was proposed that this was due to non-specific lipid-transfer between the pQDs and the cellular membranes. These findings show that imaging read-outs from non-covalent contrast agent assemblies may become ambiguous due to reduced co-localization of the different imaging labels in biological environments.

*In vivo* molecular imaging with targeted MRI contrast agents benefits from methods to quantify local contrast agent concentrations. In **chapter 2-5**, it was shown that quenching of the relaxivity induced by cellular internalization hampers contrast agent quantification based on changes in MRI contrast parameters. In the *in vitro* study described in **chapter 6** we have investigated the quantification potential of a combination of  $^1\text{H}$  MRI,  $^{19}\text{F}$  MRI and  $^{19}\text{F}$  MRS, using a lipid-coated paramagnetic perfluorocarbon emulsion. HUVECs took up the  $\alpha_v\beta_3$ -integrin targeted emulsion to a higher extent than non-targeted

emulsion. Association of the targeted emulsion with the cells resulted in a concentration-dependent proton  $R_1$  with different values for targeted and control nanoparticles, prohibiting unambiguous quantification of local contrast agent concentration, using  $^1\text{H}$ -MRI. Upon cellular association, the fluorine  $R_1$  remained constant with concentration, while the fluorine  $R_2$  showed a concentration-dependent increase. Even though the fluorine  $R_2$  was not constant, the  $^{19}\text{F}$  MRI and  $^{19}\text{F}$  MRS signals were linear and quantifiable as function of nanoparticle concentration. Detection limits, however, were considerably higher for  $^{19}\text{F}$  than for  $^1\text{H}$ -MR.

**Chapter 7** reported on the development of a multimodal contrast agent for combined SPECT/MRI imaging. The development of hybrid scanners in which two imaging modalities are combined in a single setup for simultaneous dual-modality scanning is a new and exciting development in medical imaging. Dual modality imaging greatly benefits from multimodal probes that can be detected by both techniques. The liposomal contrast agent described in this chapter, contained an  $^{111}\text{In}$  label for SPECT and gadolinium-chelates for MRI contrast, creating a platform for simultaneous quantification (based on SPECT) and precise spatial localization (based on MRI) using a single probe. To explore the utility of the liposomal probe, incubations were done with HUVECs and cell samples were analyzed using MRI, SPECT/CT,  $\gamma$ -counting, confocal laser scanning microscopy (CLSM) and inductively coupled plasma mass spectrometry (ICP-MS). MRI measurements revealed quenching of the  $r_1$  relaxivities as reported in the previous chapters. Furthermore, it was found that the radiolabel allowed accurate quantification of cell-internalized probe using  $\gamma$ -counting.

In **chapter 8**, an overview was given of the results of incubations with the different contrast agents and the findings regarding cellular location, relaxometric properties and cellular uptake were discussed. Furthermore, the utility of gadolinium-based paramagnetic MRI contrast agents was reviewed, followed by a discussion on the perspectives of multimodality imaging.





## Dankwoord

Klaas, als eerste wil ik jou bedanken voor de mogelijkheid om in jouw groep te promoveren. In eerste instantie had ik gesolliciteerd bij een andere vakgroep van de TU/e waar de sollicitatiebrief was blijven liggen. Jij en Gustav kwamen mijn brief tegen en besloten me uit te nodigen voor een gesprek. Vanaf het eerste moment voelde ik me erg op mijn plaats en wist gelijk dat ik hier wilde promoveren. De Summerschool op Kreta was natuurlijk een leuk extraatje. Je had en hebt een fantastische sfeer in je groep die er voor gezorgd heeft dat ik altijd met plezier naar mijn werk kwam. Verder wil ik je bedanken voor alle wetenschappelijke input. Ik heb erg veel van je geleerd en ik bewonder je integriteit en de manier waarop je wetenschappelijk onderzoek aanpakt.

Gustav, ook met jou heb ik altijd erg prettig samengewerkt. Jij en Klaas vormen een sterk team. Jouw kennis, je enthousiasme, je manier van werken en begeleiden zorgde ervoor dat ik optimaal onderzoek kon doen. Je stond altijd klaar om vragen te beantwoorden, sequenties uit te leggen, nog een keer naar mijn artikel te kijken of te helpen met de MRI scanner. Ook heb ik veel geleerd van je manier van schrijven.

Tijdens mijn promotie heb ik vier masterstudenten mogen begeleiden. Sjoerd, ik heb met erg veel plezier met je samengewerkt en daar zelf ook veel van opgestoken. Ik wil je bedanken voor je aandeel in hoofdstuk 2 en 3. Heel veel succes in Noorwegen en ik ben erg benieuwd naar jouw boekje. Elsbeth, ook van jou heb ik veel geleerd. Ik wil je graag bedanken voor het werk dat je verzet hebt. Helaas heeft je werk niet geleid tot een hoofdstuk in dit proefschrift. Desiree, your drive was a great motivation for me. I would like to thank you for your work of which the results are described in chapter 6. Good luck in the future, with your family and your PhD. Luc, jou heb ik samen met Erik begeleid. Ondanks een aantal tegenslagen (niet voor niets kreeg je van mij de bijnaam Jinx), die je gelukkig allemaal hebt opgelost, heeft jouw werk geleid tot een waardevolle aanwinst in mijn boekje. Dankjewel. Ik wens je heel veel succes met je eigen promotieonderzoek. Verder wil ik Jessica, Lars, Wouter, Martijn en Inge, die ik als interne stagiairs heb begeleid, bedanken voor hun inzet en het werk dat ze hebben gedaan.

Ik heb met verschillende mensen aan uiteenlopende projecten gewerkt de afgelopen 4 jaar. Marjan, ik heb het altijd leuk gevonden om naar Utrecht te komen, voor onze pogingen om de contrastmiddelen uit endosomen te halen met PCI. Ik ben nog steeds van mening dat het zou moeten werken. Helaas bleek keer op keer, dat theorie en praktijk niet met elkaar verenigbaar waren.

Willem, jouw deeltjes lagen aan de basis van mijn onderzoek. Ik wil je graag bedanken voor alle hulp, discussies en inzichten. Je hebt me altijd scherp gehouden. Daisy, jou wil ik graag bedanken voor alle hulp bij verschillende experimenten en het schrijven van hoofdstuk 2. Ook vond ik onze uitstapjes naar het theater erg geslaagd. Hopelijk kunnen we dat nog vaker doen in de toekomst. Holger, ik wil je bedanken voor alle gesprekken, ideeën en discussies en natuurlijk ook voor de grote hoeveelheid ICP-MS metingen, die van onschatbare waarde waren voor dit proefschrift. Ik heb altijd graag met je samengewerkt en ik wens je veel succes toe als hoogleraar. I would also like to thank Enzo Terreno of the University of Torino for his insights and fruitful discussions, which led to a joint publication. Furthermore, I would like to thank you and Silvio Aime for the NMRD measurements on cell pellets. Special thanks go to Charles S. Springer Jr. from the Oregon Health & Science University, Portland, USA for his vital contributions to Chapter 3 on the modeling of the relaxation properties of cell-internalized paramagnetic liposomes. I would like to thank Dr. Jean-Marc Idée (Guerbet) for his insightful discussions and critical reading of Chapter 4. Hoofdstuk 5 is tot stand gekomen uit een samenwerking met verschillende mensen. Graag wilde ik Yiming Zhao, Celso de Mello Donegá en Andries Meijerink hartelijk danken voor de prettige samenwerking en in het speciaal voor de grote hoeveelheid quantum dots die beschikbaar werden gesteld voor de experimenten. Ook wil ik graag Patrick Chin en Fijs van Leeuwen van het NKI bedanken voor het meedenken over de opzet van dit project. Anke, met jou heb ik samengewerkt aan verschillende projecten die uiteindelijk hebben geresulteerd in hoofdstuk 6 en 7. Ik heb altijd erg veel plezier gehad om met jou een wetenschappelijk vraagstuk uit te werken. Naast de wetenschap waren er natuurlijk de spelletjesavonden waarmee we hebben bewezen dat uitstel niet altijd tot afstel leidt. Hoofdstuk 6, was niet zo'n mooi hoofdstuk geworden zonder de spectroscopie. Jeanine, ontzettend bedankt voor alle hulp als ik weer eens binnen kwam vallen met een probleem. Jean-Pierre Timmermans van de Universiteit Antwerpen wil ik graag bedanken voor de fijne samenwerking op gebied van TEM en CLSM. Verder wil ik Peter Frederik en Paul Bomans bedanken voor het samen onderzoek doen naar een nieuwe invriestechiek voor cellen. Bedankt voor jullie inzet.

Tijdens mijn promotie heb ik veel tijd doorgebracht in het Cellab. Hoewel ik als indringer van natuurkunde werd bestempeld, heb ik er altijd met erg veel plezier gewerkt. Bedankt iedereen! Moniek, jou wil ik speciaal bedanken voor alle gesprekken, noodbestellingen en andere oplossingen.

Niet te vergeten zijn alle groepsleden van Biomedical NMR en TPM. Bedankt voor alle hulp, inzet, antwoorden, kritische vragen, gezelligheid, koffiepraat,

kart events, BBQs, volleybal, cricket, voetbal, borrels en nog veel meer. Larry, bedankt voor alle hulp bij het ontwerpen van de verschillende spoelen en houders. Ook wil ik graag alle vakmensen van de werkplaats in N-laag bedanken voor het maken van de spoelen en houders en alle klusjes die even tussendoor werden uitgevoerd. Hedwig en Ria, dankjewel voor alle hulp. Bij jullie kon ik altijd terecht om van alles en nog wat te regelen. Dankjewel voor alle gezelligheid en natuurlijk niet te vergeten de kilo's snoepjes en koekjes die ik in de afgelopen 4 jaar heb weggewerkt. Een belangrijk onderdeel van deze groep mensen waren mijn kamergenoten. Glenda, Erik, Roel, het was altijd erg gezellig in Baklava 2.01. Helaas was het niet mogelijk om drie paranimfen te hebben. Naast de gezelligheid stonden jullie ook altijd klaar om even te helpen, of mee te denken over een probleem of experiment. Heel erg bedankt voor deze mooie tijd.

Als laatste wil ik graag het thuisfront bedanken. Thea, Gerard, bedankt voor alle gezelligheid en hulp bij het verhuizen. Jasper, jouw interesse in mijn werk zorgde er voor dat ik nog meer plezier en energie kreeg in mijn onderzoek. Papa, mama, jullie hebben me altijd gesteund om te doen waar mijn hart ligt, ook in zware tijden. Ondanks dat het maar 168 km naar Hengelo is en je het volgens jullie in 75 minuten kan rijden was de afstand toch meestal groter dan me lief was. Heel erg bedankt voor jullie steun. Als laatste wil ik Jeanne bedanken voor alles. Je bent altijd lief en je staat altijd voor me klaar. Ik hou van jou.

**List of Publications****International refereed journal publications**

**M.B. Kok**, S. Hak, W.J.M. Mulder, D.W.J. van der Schaft, G.J. Strijkers, K. Nicolay, *The cellular compartmentalization of internalized paramagnetic liposomes strongly influences both  $T_1$  and  $T_2$  relaxivity*, **Magnetic Resonance in Medicine**, 61(5), p. 1022-1032, 2009

G.J. Strijkers, S. Hak, **M.B. Kok**, C.S. Springer Jr, K. Nicolay, *A three-compartment  $T_1$ -relaxation model for intracellular paramagnetic contrast agents*, **Magnetic Resonance in Medicine**, 61(5), p. 1049-1058, 2009

E. Terreno, J. Stancanello, D. Longo, D. Delli Castelli, L. Milone, H.M.H.F. Sanders, **M.B. Kok**, F. Uggeri, S. Aime, *Methods for improved detection of the MRI-CEST effect*, **Contrast Media and Molecular Imaging**, 4(5), p. 237-247, 2009

**M.B. Kok**, A. de Vries, D. Abdurrachim, J.J. Prompers, H. Gröll, K. Nicolay, G.J. Strijkers, *Quantitative  $^1H$  MRI,  $^{19}F$  MRI, and  $^{19}F$  MRS of cell-internalized perfluorocarbon paramagnetic nanoparticles*, **submitted**

**M.B. Kok**, G.J. Strijkers, K. Nicolay, *Dynamic changes in  $^1H$ -MR relaxometric properties of cell-internalized paramagnetic liposomes, as studied over a 5-day period*, **submitted**

**M.B. Kok**, L.W.E. Starmans, H.M.H.F. Sanders, Y. Zhao, C. de Mello Donegá, A. Meijerink, W.J.M. Mulder, H. Gröll, G.J. Strijkers, K. Nicolay, *Influence of cell-internalization on relaxometric, optical and compositional properties of targeted paramagnetic quantum dot micelles*, **in preparation**

### Conference Proceedings

**M.B. Kok**, S. Hak, W.J.M. Mulder, G.J. Strijkers, K. Nicolay, *Intracellular uptake of targeted contrast agent by HUVECs leads to quenching of  $T_1$  contrast*, **First Benelux In Vivo MR Methods Symposium**, Nijmegen, The Netherlands, 2007

**M.B. Kok**, S. Hak, D.W.J. van der Schaft, G.J. Strijkers, K. Nicolay, *Quenching of  $T_1$  relaxivity in HUVECs targeted with paramagnetic RGD liposomes*, **European Society of Molecular Imaging**, Napels, Italy, 2007

**M.B. Kok**, S. Hak, W.J.M. Mulder, D.W.J. van der Schaft, G.J. Strijkers, K. Nicolay, *Intracellular uptake of targeted paramagnetic contrast agent leads to quenching of  $T_1$  contrast*, **ISMRM 16<sup>th</sup> Scientific Meeting & Exhibition**, Toronto, Canada, 2008

G.J. Strijkers, S. Hak, **M.B. Kok**, C.S. Springer Jr, K. Nicolay, *A three-compartment  $T_1$ -relaxation model for intracellular contrast agents: implications for molecular imaging*, **ISMRM 16<sup>th</sup> Scientific Meeting & Exhibition**, Toronto, Canada, 2008

A. de Vries, **M.B. Kok**, H. Grull, G.J. Strijkers, K. Nicolay, *Quantitative imaging of a cell-internalized trimodal contrast agent*, **2009 World Molecular Imaging Congress**, Montreal, Canada, 2009

L.W.E. Starmans, **M.B. Kok**, H.M.H.F. Sanders, Y. Zhao, C. de Mello Donegá, A. Meijerink, W.J.M. Mulder, H. Grull, G.J. Strijkers, K. Nicolay, *Influence of cell-internalization on the relaxometric and optical properties of paramagnetic quantum dot micelles*, **ISMRM Benelux Annual Meeting 2010**, Antwerp, Belgium, 2010

**Curriculum Vitae**

Maarten Kok werd op 25 januari 1981 geboren te Enschede. Na het behalen van zijn VWO diploma aan De Bataafse Kamp in Hengelo startte hij met de opleiding Chemische Technologie aan de Universiteit Twente. Het ingenieursdiploma werd in 2005 behaald na een afstudeerproject bij de vakgroepen van prof. dr. W. Kruijer en prof. dr. J. Feijen. In 2002 is hij gestart met de universitaire lerarenopleiding, welke hij in 2006 succesvol afrondde met het behalen van de graad Master of Science. Van januari 2006 tot februari 2010 werkte hij in de Biomedische NMR groep van de faculteit Biomedische Technologie aan de Technische Universiteit Eindhoven onder begeleiding van dr. ir. G.J. Strijkers en prof. dr. K. Nicolay aan zijn promotie onderzoek getiteld: Cell-internalized MRI contrast agents, waarvan de belangrijkste resultaten staan beschreven in dit proefschrift. Op dit moment is hij werkzaam als klinisch chemicus in opleiding in het Medisch Centrum Alkmaar.

Maarten Kok was born on January 25<sup>th</sup> 1981 in Enschede, The Netherlands. In 1999, he finished his secondary school education (Atheneum) De Bataafse Kamp in Hengelo. In the same year he started studying Chemical Engineering at the University of Twente, where he obtained his Master of Science degree in 2005 after completion of a joined undergraduate project in the groups of prof. dr. W. Kruijer and prof. dr. J. Feijen. In 2002, he also started his studies Teaching Chemistry, and obtained this Master of Science degree in 2006. From January 2006 until February 2010 he worked under the supervision of dr.ir. G.J. Strijkers and prof.dr. K. Nicolay in the Biomedical NMR group of the Department of Biomedical Engineering of Eindhoven University of Technology on his PhD-project, entitled Cell-internalized MRI contrast agents of which the principal results are described in this thesis. In December 2009 Maarten started his Clinical Chemistry residence in Alkmaar Medical Centre.